A Trigger with the BST-PAD Detector for the H1 Experiment

Diplomarbeit

Humboldt-Universität zu Berlin
Mathematisch-Naturwissenschaftliche Fakultät I
Institut für Physik

eingereicht von

Jan Kretzschmar
geboren am 18.12.1978 in Leipzig

Aufgabensteller: Prof. Dr. Hermann Kolanoski

Berlin, den 15.12.2003

Contents

Introduction

The goal of research in high-energy physics is to understand the structure of matter and its interactions. In the last decades the theoretical framework known as the Standard Model, describing the unified electroweak force and Quantum Chromo Dynamics (QCD), has been very successful in explaining most experimental data from interactions of leptons with leptons, hadrons with leptons, and hadrons with hadrons.

The structure of hadrons cannot be calculated from first principles due to the non perturbative nature of QCD at low energies, which is believed to lead to confinement of quarks and gluons. On the other hand the property of asymptotic freedom makes predictions possible at higher energies. The study of lepton-nucleon interactions and here especially deep inelastic scattering (DIS) allows us to measure the structure of hadrons and test QCD predictions.

HERA is the world's first electron-proton collider. It is located at the DESY in Hamburg, Germany, and has been delivering luminosity since 1992. H1 is one of the two colliding beam experiments at the accelerator. With a center of mass energy about one magnitude higher than previous fixed target experiments, it is a great tool for studying the proton structure in new kinematic regions and testing predictions of the Standard Model.

In 2000 the HERA I Program was finished. In the following shutdown, both the collider and the H1 experiment were upgraded for the high luminosity phase HERA II. The goal of 1 fb^{-1} luminosity until 2006 was set. It is to be achieved by a new beam focusing strategy.

The HERA II program includes inclusive DIS measurements with lepton beam polarization, heavy flavor physics, and searches beyond the Standard Model. The silicon vertex detectors of H1 play a crucial role for the precision measurements. The DESY Zeuthen group is responsible for 2 of the 3 silicon track detectors in H1, the Forward and Backward Silicon Tracker (FST and BST). The BST comprises a dedicated silicon trigger detector, the Backward Silicon Track Trigger (BSTT). The BSTT is a fast Level 1 trigger device based on silicon sensors made up of pads. It is the main topic of this thesis.

Chapter 1 gives a brief introduction into the framework used in DIS physics. Experimental aspects of HERA and H1 are described in chapter 2, while chapter 3 deals with H1's silicon detectors. First experiences with HERA II were not trouble free. High backgrounds prevented continuous high luminosity operation. A major part of the work discussed in this thesis, are studies to understand these problems. The BSTT is an important tool here. This work is presented in chapter 4. Results of first BSTT data are presented in chapter 5. They prove the functionality of the detector.
In 2003 a shutdown was taking place to cure the observed problems. Together with a planned upgrade, repairs had to carried out on the whole BST. This process is described in chapter 6.

Chapter 1

Deep Inelastic Scattering

In 1911 Ernest Rutherford established the substructure of the atom with his interpretation of a scattering experiment using α particles as probes. In a similar way a SLAC experiment revealed the partonic substructure of the nucleon in 1969. Since this time lepton-nucleon scattering has been the major tool for studying the nucleon structure. The advantages of leptons are their point like appearance and well understood interactions. This chapter summarizes the theoretical framework used to describe and interpret the data.

1.1 Kinematics

Within the framework of the Standard Model lepton-nucleon interaction proceeds via the exchange of a virtual vector boson, see figure 1.1.
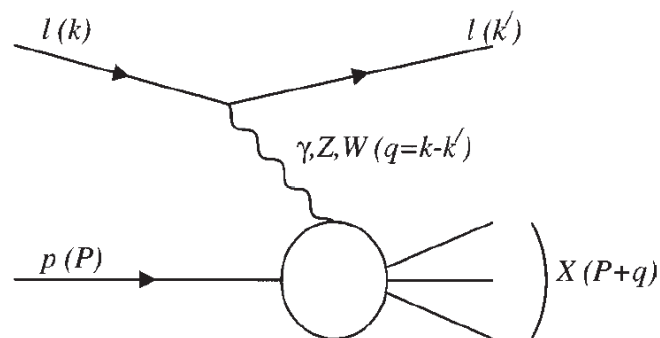

Figure 1.1: Lowest order Feynman diagram describing deep inelastic lepton-nucleon scattering, 4 momenta in parentheses

1

In the case of a neutral boson, γ or Z^0, the reaction is called "neutral current" (NC), while a reaction with $W^{\pm}$ exchange is a "charged current" (CC) process. The kinematics of the scattering process $lN \to l'X$ are most conveniently described with the usual Lorentz invariant variables formed from the 4 momenta of the particles [1]:

$$
\begin{aligned}
s &= (k + P)^2 \\
Q^2 &= -q^2 = -(k - k')^2 > 0 \\
W^2 &= (q + P)^2 \\
x &= \frac{Q^2}{2P \cdot q} \\
y &= \frac{q \cdot P}{k \cdot P} \\
\nu &= \frac{q \cdot P}{m_N} \, .
\end{aligned}
\tag{1.1}
$$

Here $\sqrt{s}$ and W are the center of mass energies of the lepton-nucleon and intermediate boson-nucleon systems, respectively. Q^2 determines the hardness or resolution of the interaction.

At high energies the masses of lepton and the nucleon can be ignored. In the rest frame of the nucleon the relations

$$
\nu = E_l - E_l' \, ,
\tag{1.2}
$$

$$
y = 1 - \frac{E_l'}{E_l} \quad \Rightarrow \quad 0 \leq y \leq 1 \, ,
\tag{1.3}
$$

hold, where E_l and E_l' are the lepton energies before and after scattering, respectively. This shows ν to be the energy of the intermediate boson, while y is a measure of the inelasticity of the interaction.

In the quark-parton model (QPM) the variable x, introduced by Bjorken, is the fraction of the nucleon momentum carried by the struck quark in the infinite momentum frame. Therefore it is also bounded as $0 \leq x \leq 1$.

Ignoring masses, the following relations between the invariants exist [2]

$$
Q^2 = sxy \, , \quad W^2 = Q^2 \left(\frac{1}{x} - 1 \right) = sy - Q^2 \, ,
\tag{1.4}
$$

so that the kinematics is determined by s and any 2 of the other variables from the equations (1.1).

Different kinematic domains are defined by the virtuality of the exchanged boson. The **photoproduction** domain is defined by $Q^2 \sim 0$, which corresponds to a photon that is almost on-shell. The **DIS** regime starts at about $Q^2 \gtrsim 1 \text{ GeV}^2$.

1.2 Reconstruction of DIS events

This section is adapted to the HERA collider experiments, which provide almost complete information about a scattering event. Therefore in neutral current events the kinematics can be reconstructed from the scattered electron, the hadronic final state or a combination of both. For charged current events with an undetected neutrino only the hadronic final state is available. There are several established methods [1] to reconstruct the kinematic variables. Usually the energy E'_e and angle θ_e of the scattered electron, and longitudinal $p_{z\,had}$ and transverse $p_{t\,had}$ momentum of the hadronic final state are measured. In addition $s = 4E_e E_p$ and E_e are known collider parameters. The angle θ is defined as in the H1 coordinate system. In this convention the incoming proton defines the positive z direction and polar angles are measured as usual with respect to this axis.

The **Electron Method** is traditionally employed at fixed target experiments and relies completely on the detection of the scattered electron:

$$Q^2 = 4E_e E'_e \cos^2 \frac{\theta_e}{2}\,, \qquad (1.5)$$

$$y = 1 - \frac{E'_e}{E_e} \sin^2 \frac{\theta_e}{2}\,. \qquad (1.6)$$

According to the laws of error propagation, the kinematic variables are reconstructed with the following uncertainties:

$$\frac{\delta Q^2}{Q^2} = \frac{\delta E'_e}{E'_e} \oplus \tan \frac{\theta_e}{2} \cdot \delta\theta_e\,, \qquad (1.7)$$

$$\frac{\delta y}{y} = \left(1 - \frac{1}{y}\right) \cdot \frac{\delta E'_e}{E'_e} \oplus \left(\frac{1}{y} - 1\right) \cot \frac{\theta_e}{2} \cdot \delta\theta_e\,, \qquad (1.8)$$

where $\oplus$ is defined via the relation $A \oplus B \equiv \sqrt{A^2 + B^2}$. Problems of this method are degraded resolution at small y as can be seen from the terms with singularities $1/y$. The method is used mainly at high $y > 0.2$. Large corrections for initial state radiation are required.
Another general problem are the terms $\propto \tan \frac{\theta_e}{2}$ which are responsible for degrading resolution at large electron scattering angles $\theta_e \to 180°$. This was one of the reasons to build Silicon Trackers in this range, as their high spacial resolution can partially make up for this deficiency.

The Σ **Method** is another general method for reconstruction of the kinematic variables using measurements from the scattered electron (θ_e, E'_e) and

the hadronic final state (Σ):

$$\Sigma \;=\; E_{had} - p_{z\,had} = \sum_{i=1}^{\#hadrons} E_i (1 - \cos\theta_i)\,, \qquad (1.9)$$

$$y \;=\; \frac{\Sigma}{\Sigma + E'_e(1 - \cos\theta_e)}\,, \qquad (1.10)$$

$$Q^2 \;=\; \frac{E'^2_e \sin\theta_e}{1 - y}\,. \qquad (1.11)$$

Using the error propagation,

$$\frac{\delta y_\Sigma}{y_\Sigma} = (1-y) \left(\frac{\delta\Sigma}{\Sigma} \oplus \frac{\delta E'_e}{E'_e} \oplus \frac{\delta\theta_e}{\tan\theta_e/2} \right) \qquad (1.12)$$

one concludes that this method gives a better precision compared to the electron method at low y. Also initial state radiation does not effect the result. Because of these advantages H1 has employed this method for a certain kinematic range.

Another method is the **Hadron Method**, which relies completely on the detection of the hadronic final state. That is why this method is suitable for reconstruction of CC events, where no information from the neutrino is available. Otherwise including information from the scattered lepton improves reconstruction quality.

1.3   Inclusive Cross Sections Measurements

Due to the non perturbative nature of QCD at low energies, it is not possible to calculate the structure of nucleons from first principles. Cross sections therefore have to be expressed with the help of structure functions. These structure functions can be interpreted in terms of parton distribution functions which is very transparent in the quark-parton model. However higher order QCD corrections change the picture. Finally a high center of mass energy and lepton polarization complicate the picture further because of electroweak effects. This will not be discussed here.

1.3.1   Lepton-Nucleon Scattering and the Quark-Parton Model

The inclusive differential cross section for the general process $lN \rightarrow l'X$ can be expressed as a function of any two variables from equations (1.1).

Conventionally x and Q^2 are chosen. The unpolarized cross section at low $Q^2 \ll M_{W,Z}^2$ can be expressed by the use of structure functions F_1, F_2, and F_3 [1]:

$$\frac{d^2\sigma^{l(\bar{l})N}}{dxdQ^2} = A\left\{\frac{y^2}{2}2xF_1(x,Q^2) + (1-y)F_2(x,Q^2) \pm \left(y - \frac{y^2}{2}\right)xF_3(x,Q^2)\right\},$$
(1.13)

where $A = G_F^2/2\pi x$ for neutrinos and $A = 4\pi\alpha^2/xQ^4$ for charged leptons.

In the quark-parton model (QPM) the nucleon is viewed as being composed of free constituents, quarks and gluons. The electroweak gauge bosons couple only to quarks, involving a mixture of vector (v) and axial vector (a) couplings. The structure functions can be expressed in terms of the individual quark distributions $q_i(x)$. Assuming quarks are spin 1/2 particles there are 3 structure functions:

$$\begin{aligned}
F_1(x) &= \frac{1}{2}\sum_i q_i(x)(v_i^2 + a_i^2)\,, \\
F_2(x) &= \sum_i xq_i(x)(v_i^2 + a_i^2)\,, \\
F_3(x) &= 2\sum_i q_i(x)(v_i a_i)\,.
\end{aligned}$$
(1.14)

For the case of electromagnetic interaction we have $v_i = e_i$, where e_i is the charge of quark flavor i, and $a_i = 0$. For charged currents the couplings are $v_i = a_i = 1$ for quarks and $v_i = -a_i = 1$ for antiquarks. Weak neutral current couplings depend on the third component of weak isospin T_{i3} as $v_i = T_{i3} - 2e_i\sin^2\theta_W$ and $a_i = T_{i3}$.

A consequence of the equations (1.14) is the Callan-Gross formula that relates F_1 and F_2 for spin 1/2 particles

$$2xF_1(x) = F_2(x)\,.$$
(1.15)

As can further be seen, F_3 is only important in parity violating weak interactions with $a_i \neq 0$. So for charged lepton-nucleon interactions and $Q^2 \ll M_{W,Z}^2$ the cross section is only a function of $F_2(x)$. The dependence of the structure functions on x only is called Bjorken scaling.

1.3.2 QCD Evolution of Parton Distributions and Structure Functions

Partons can in reality not be noninteracting, as they are confined to hadrons. The quark-parton model has to be altered accordingly to take into account

features of QCD.

Qualitatively fluctuations are expected due to emission and reabsorption of gluons by the quarks and splitting of gluons to $q\bar{q}$ pairs. A quark seen at a scale Q_0^2 carrying a momentum fraction x_0 can be resolved into more quarks and gluons at a higher Q^2, so the structure functions will acquire a Q^2 dependence violating the Bjorken scaling.

Given a small enough effective strong coupling α_s, the parton evolution can be calculated within perturbative QCD (pQCD). The result is called Dokshitzer-Gribov-Lipatov-Altarelli-Parisi (DGLAP) evolution equations, which describe how quark q and gluon g momentum distributions evolve with the scale of the interactions Q^2 [1]

$$\frac{\partial}{\partial \ln Q^2} \begin{pmatrix} q \\ g \end{pmatrix} = \frac{\alpha_s(Q^2)}{2\pi} \left[\begin{array}{cc} P_{qq} & P_{qg} \\ P_{gq} & P_{gg} \end{array} \right] \otimes \begin{pmatrix} q \\ g \end{pmatrix}, \qquad (1.16)$$

where both q and g are functions of x and Q^2. The $\otimes$ stands symbolic for a convolution integral. $P_{ij}(z)$ are the splitting functions and can be interpreted as the probability for a parton j to emit a parton i with momentum fraction z of the parent parton [2]. These splitting functions are calculated using perturbative QCD.

Due to the QCD evolution the simple relations between the structure functions and the individual quark distributions (1.14,1.15) also have to be modified. To leading order all functions just acquire a Q^2 dependence. In next-to-leading order (NLO) the Callan-Gross relation is violated and the longitudinal structure function,

$$F_L = F_2 - 2xF_1, \qquad (1.17)$$

is nonzero. Its value is predicted by QCD from F_2 and the gluon density g [2].

1.3.3   Structure Functions at the HERA collider

HERA provides colliding lepton-proton beams with a high center of mass energy of $\sqrt{s} \approx 320$ GeV. Due to the relation $Q^2 = sxy$, measurements at very low values of x or high values of Q^2 are a unique opportunity. The regions accessible by the HERA collider experiments H1 and ZEUS and fixed target experiments in the (x, Q^2) plane are shown in figure 1.2.

At low x precision tests of the QCD dynamics are possible, while the high Q^2 region tests the unified theory of electroweak interaction and is the first to show potential new physics. These two domains are characterized by the lepton being scattered into different regions of H1: for small Q^2 the lepton is
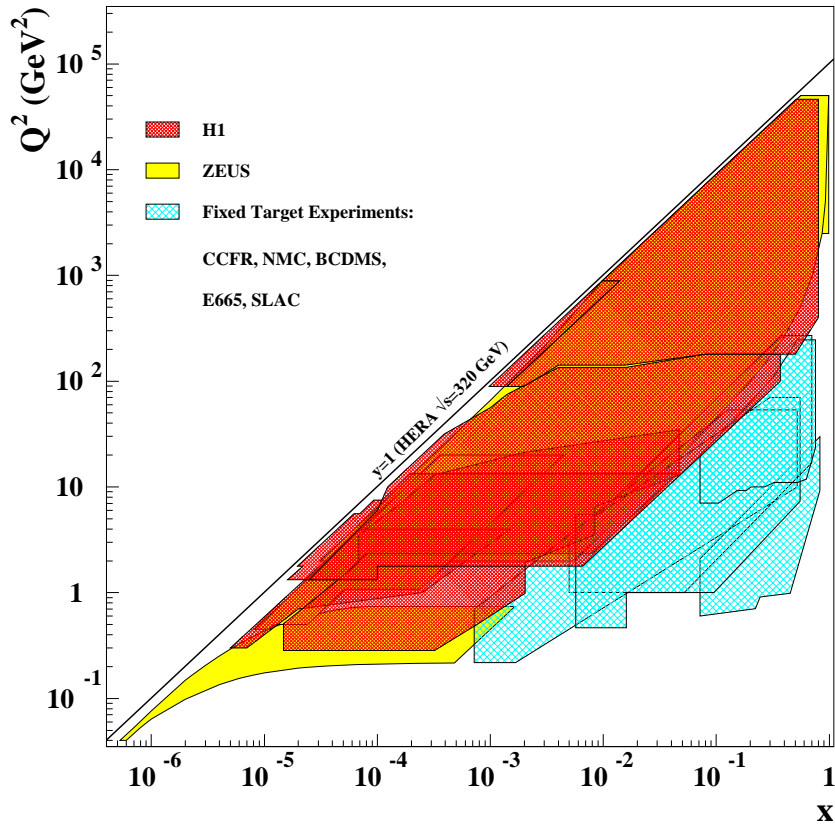
Figure 1.2: Regions in the (x, Q^2) plane where measurements of the nucleon structure function F_2 have been performed by fixed-target and HERA experiments

scattered by a small angle to $\theta_e \sim 180°$ into the so called backward region, whereas for high Q^2 the lepton is scattered by a large amount to $\theta_e \sim 0$, the forward region of H1. This can be understood considering the Electron Method reconstruction, equation (1.5).

1.3.4 Low Q^2 Measurements

One of the main contributions of HERA was to measure F_2 with high precision and to confirm the scaling violations in Q^2 and the violation of the Callan-Gross relation, i.e. the need for $F_L \neq 0$. The existence of F_L is purely due to QCD dynamics and measurements are a very sensitive test of the understanding of the strong force. Figure 1.3 shows results published by the H1 collaboration [3, 4]. Measurement of the scaling violations in Q^2 in combination with QCD fits make the determination of α_s possible.
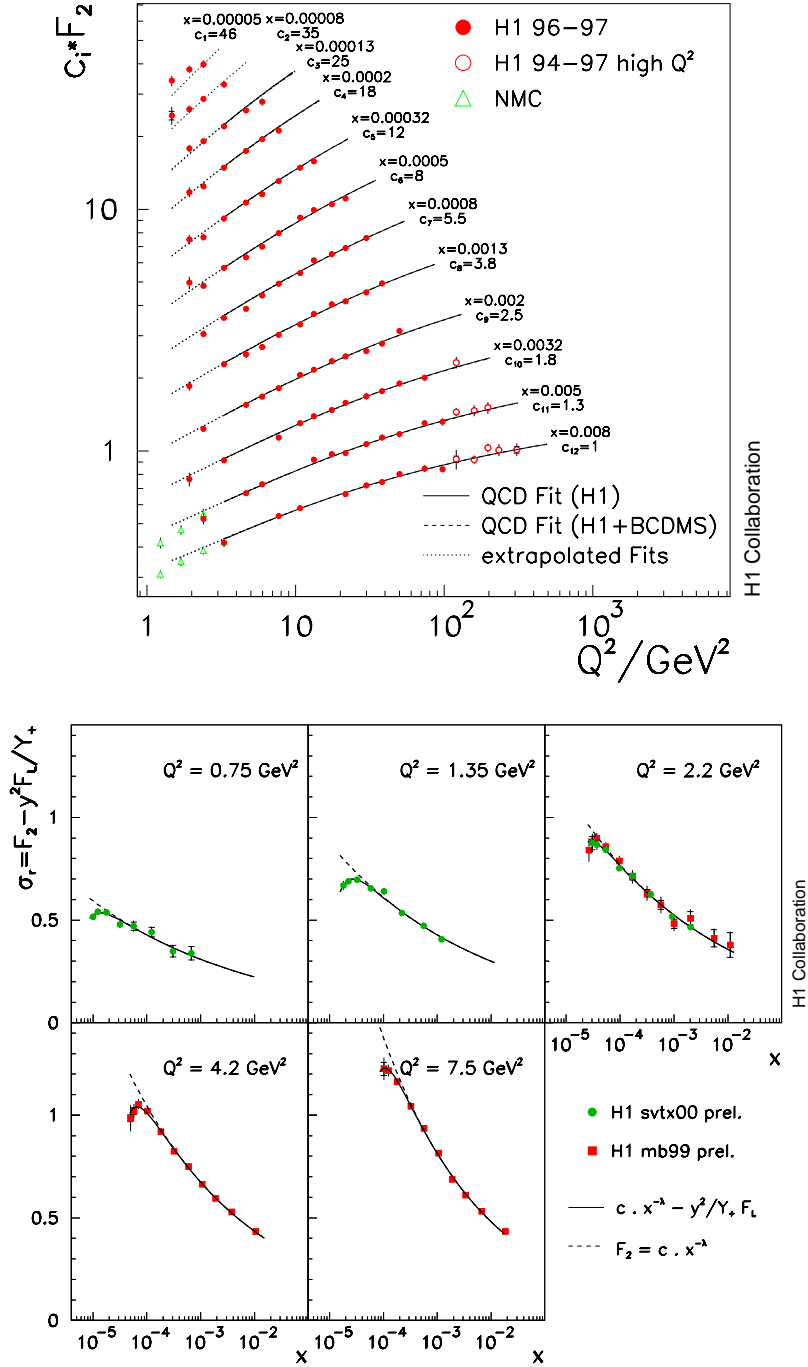
Figure 1.3: Above: Measurement of the structure function $F_2(x, Q^2)$ at low Q^2 and corresponding QCD fit [3]. Below: Reduced Cross section σ_r at low Q^2 as function of x. The deviation of σ_r from the dashed extrapolation at low x is attributed to the longitudinal structure function $F_L \neq 0$ [4].

At low Q^2 the neutral current double differential cross section, $d^2\sigma/dxdQ^2$, is dominated by photon exchange. Rescaling the cross section by the kinematic factor $k = \frac{2\pi\alpha^2 Y_+}{xQ^4}$ with $Y_+ = 1 + (1 - y)^2$, one obtains the reduced cross section

$$\sigma_r(x, Q^2) = F_2(x, Q^2) - \frac{y^2}{Y+}F_L(x, Q^2)\,. \qquad (1.18)$$

At fixed Q^2 F_L contributes most at high y and therefore low x. According to equation (1.6) this corresponds to a low scattered electron energy E'_e. Precise DIS measurement in this kinematic domain is a challenge because of:

- degrading resolution in the reconstruction of the kinematic variables from the electron method, see equation (1.8),

- high backgrounds from photoproduction.

Both problems are tackled by the "Backward Silicon Tracker" (BST) of H1. It provides improved tracking resolution, can determine the charge of a track, and can separate photons from real DIS electrons. This was done offline [3] and will be done online using the "Backward Silicon Track Trigger" (BSTT).

1.3.5 High Q^2 Measurements

At high Q^2 the contribution of the longitudinal structure function becomes negligible, but the possible exchange of parity violating electroweak gauge bosons Z^0 (in interference with γ) and $W^\pm$ lead to $F_3 \neq 0$. Using polarized lepton beams, and both electrons and positrons, detailed tests of the electroweak theory and further constraints on the parton densities in the proton are possible. Here the "Forward Silicon Tracker" (FST) of H1 is expected to improve the precision of the measurements.

1.4 Heavy Quark Production

One of the main goals of the high luminosity phase HERA II is heavy flavor physics. The main process for producing open charm or beauty at H1 is photon gluon fusion (figure 1.4). This process is especially interesting, because it depends directly on the gluon density of the proton. In addition to the QCD fits for inclusive measurements, this analysis provides an independent check. An early H1 analysis [5] is shown in figure 1.5. Because of their good capabilities for secondary vertex resolution, the H1 silicon trackers are crucial for these physics topics.
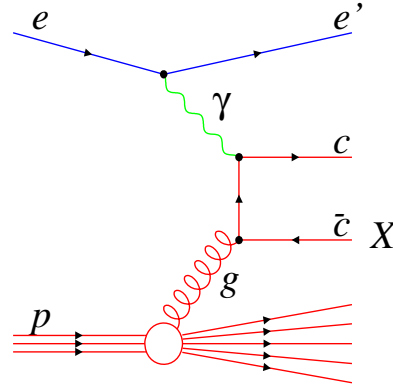
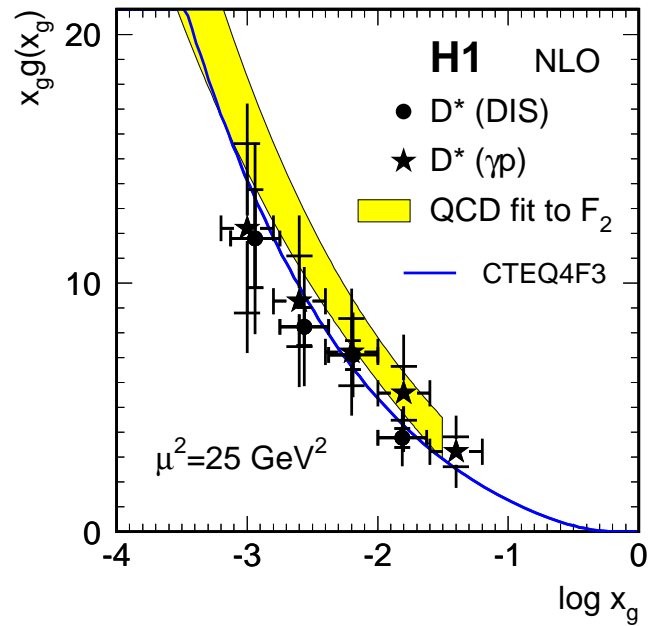Figure 1.4: Leading order heavy quark production in photon gluon fusion

Figure 1.5: Comparison of the gluon density extracted in DGLAP QCD fit from F_2 evolution and direct determination from D^* production [5]

Chapter 2

The H1 Detector at HERA

The HERA machine is the world's first lepton-nucleon collider. It is located in Hamburg, Germany. It consists of two separate accelerators each with a circumference of 6.3 km for electrons and protons, respectively. The beams are made to collide at zero angle for the two collider experiments H1 and ZEUS. In addition there are two fixed target experiments, HERMES and HERA-B, which use only the lepton and proton beam, respectively. Figure 2.1 gives an overview over the HERA accelerator facility.

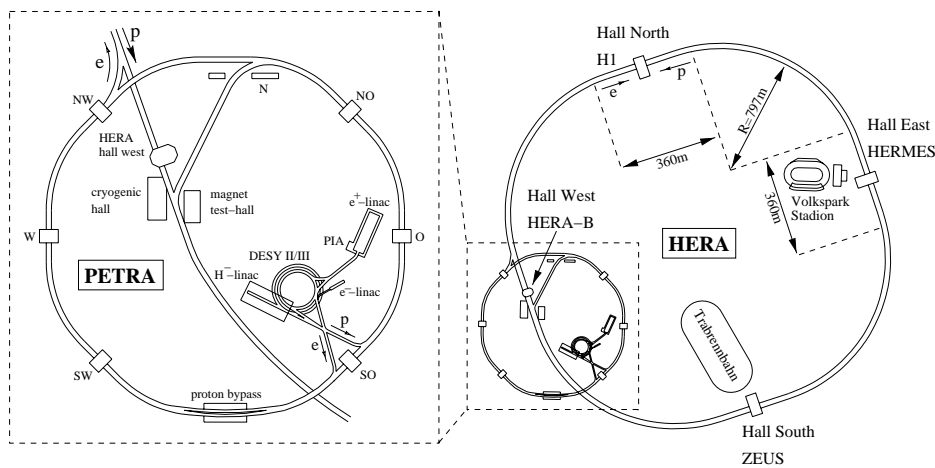Figure 2.1: The HERA accelerator facility and its 4 experiments

The physics program started in summer 1992. In 2000 the HERA I phase was finished. In the following upgrade the H1 detector and HERA were prepared for higher luminosity operation HERA II. The following two sections describe the general properties of the HERA machine and H1, while the most relevant changes during the upgrade are discussed later.

2.1   The HERA accelerator

The electron ring operates at ambient temperature and accelerates electrons or positrons to $E_e = 27.6$ GeV. The superconducting proton ring achieved an energy of $E_p = 920$ GeV from 1998 on. This corresponds to a center of mass energy $\sqrt{s} \approx 320$ GeV for the collider experiments. Due to the equation $Q^2 = sxy$ (1.4), this high center of mass energy makes Q^2 values up to $100,000\,\text{GeV}^2$ at highest x and y possible. At low Q^2, x values down to $5 \cdot 10^{-5}$ are reached. In general, the accessible y range is limited by detector resolution and "escaping" hadrons to $y \geq 0.001$.

There have also been special shifted vertex runs to increase the detector acceptance for lower Q^2 events. Figure 1.2 shows the acceptance of H1 and fixed target experiments in the kinematic (x, Q^2) plane.
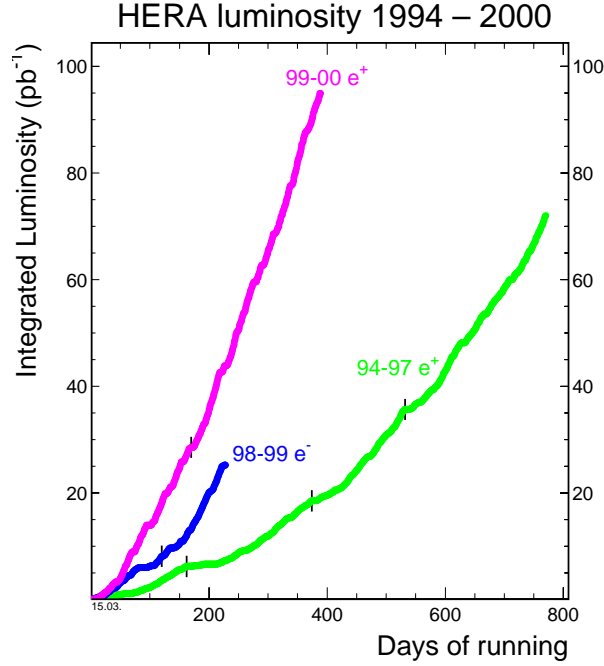
Figure 2.2: Integrated luminosities delivered by HERA I differentiated in lepton sign. Total physics luminosity collected by H1 was about 100 pb^{-1}.

For the physics the luminosity is as important as the center of mass energy. Interesting processes like very high Q^2 scattering and potential new physics tend to have small cross sections and high luminosity is needed to collect reasonable statistics. The integrated luminosities delivered in the HERA I phase are shown in figure 2.2. Maximum beam currents were $I_p = 105$ mA and $I_e = 48$ mA. A significant improvement in luminosity is expected in the

HERA II phase, which will be discussed below.

Bunch crossings occur every 96 ns or equivalently with a rate of 10.4 MHz, the frequency of the so called HERA clock. Some satellite bunches are left unpaired for background studies.

HERA can run using both electrons and positrons. Their interactions differ due to electroweak effects in NC interactions with $Q^2 \sim M_Z^2$ and in all CC interactions. With the HERA II upgrade, lepton beam polarization is available for the colliding beams having similar consequences like the sign of the lepton. Beam lifetime and background conditions are generally better for positron running. So except for an extended period in 1998/99 positrons were used. In the following the term "electron" is often used for both charged leptons.

2.2 The H1 detector

H1 is a general purpose magnetic detector with nearly hermetic calorimetric coverage designed to study all aspects of electron-proton collisions. Special emphasis has been given to the electron identification and energy resolution. H1's most important subdetectors are shown in figure 2.3.

The coordinate system of H1 is defined to have the positive z axis in incoming proton direction. The polar angle θ is measured with respect to this axis. This means, that low angle electron scattering (small Q^2) corresponds to $\theta \sim 180°$, called the "backward" direction, while electron back scattering (large Q^2) corresponds to $\theta \sim 0$ and the final states are detected in the "forward" detectors. The H1 detector in general reflects the asymmetric beam setup of HERA.

In the following a short overview of the H1 detector is given. A complete description as of 1997 can be found in [6]. Since that time many components were upgraded or exchanged. Here the current status is discussed and the most important HERA II upgrade projects are summarized. The silicon detectors will be described in detail in the next chapter.

2.2.1 Tracking detectors

Figure 2.4 shows the several tracking detectors of H1. The central trackers, shown in figure 2.5, consist of [6]

- the silicon trackers located closest to the beam pipe (see chapter 3),

- a 5 layer "Central Inner Proportional Chamber" (CIP) for triggering,

THE H1 DETECTOR

Forward Muon System   Central Muon System   Forward Tracker

Central Tracker

Silicon Tracker

Veto   Lumi

PLUG TOF   LAr Calorimeter   EM Spacal
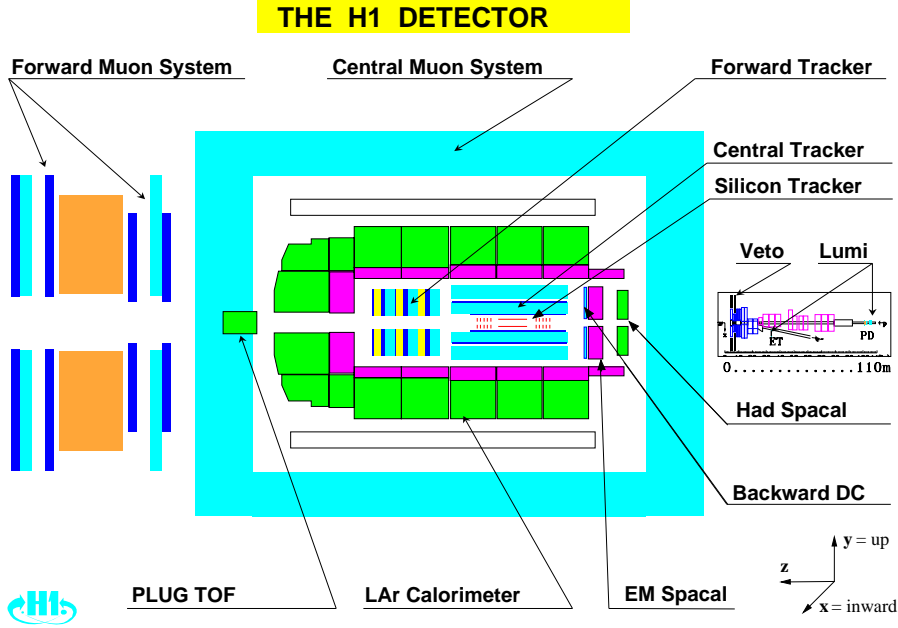
Had Spacal

Backward DC

y = up

z

x = inward

Figure 2.3: Schematic drawing of H1's subsystems, protons enter from the right, electrons from the left

- two large concentric drift chambers, called "Central Jet Chambers" (CJC1 and CJC2) with good tracking resolution in $r - \phi$ plane $\sigma_{rz} = 170\,\mu$m and worse resolution in z direction $\sigma_z = 2.2$ cm through charge division only ,

- a "Central Outer Z Chamber" (COZ) for the precise determination of the z coordinate with $\sigma_z \sim 300\,\mu$m,

- and the "Central Outer Proportional Chamber" (COP) for trigger purposes.

The angular acceptance varies for the single subdetectors, the COZ covers for example the range $25° < \theta < 155°$.

A superconducting solenoid provides a magnetic field of 1.15 T for the measurement of particle momenta. The typical momentum resolution is $\sigma_p/p^2 = 0.003\,\mathrm{GeV}^{-1}$ [6].

In forward and backward region there are further dedicated gas chambers: the "Forward Track Detector" (FTD), covering the angular range of $7° < \theta < 25°$, and the "Backward Proportional Chamber" (BPC).
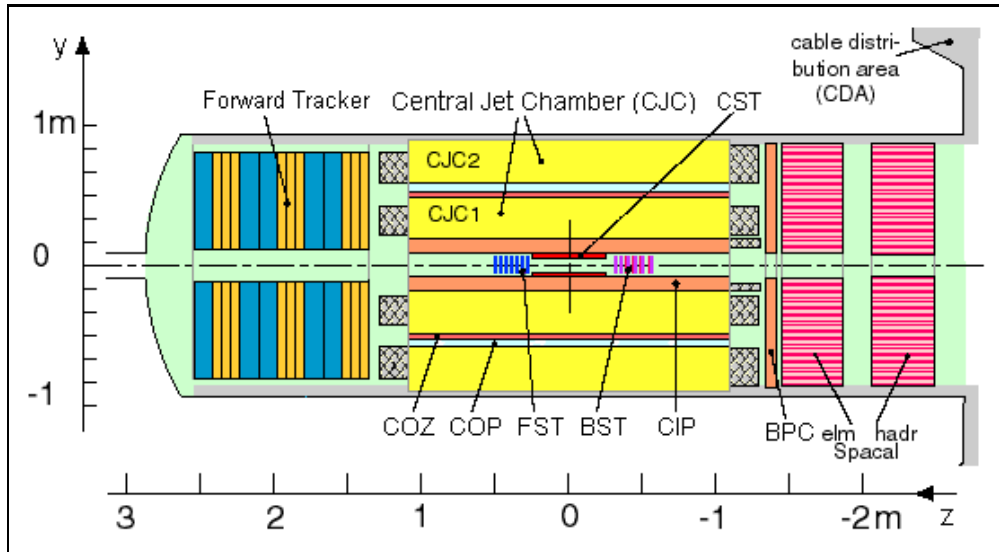
Figure 2.4: Tracking systems of the H1 detector

2.2.2 Calorimetry

The main calorimeter covering the polar angle range $4° < \theta < 154°$ is a liquid argon sampling calorimeter (LAr) [6]. In the electromagnetic section lead is used to promote shower development providing 20-30 radiation lengths, while the hadronic section is made of stainless steel providing 5-8 interaction lengths. The typical energy resolution is $\sigma_{EM}/E = 0.12/\sqrt{E(\text{GeV})} \oplus 0.01$ and $\sigma_{had}/E = 0.50/\sqrt{E(\text{GeV})} \oplus 0.02$ for electromagnetic and hadronic showers, respectively. The calorimeter is non-compensating. Reweighting of the hadronic shower energies is done during offline processing.
In backward direction a lead-scintillating fiber calorimeter ("Spaghetti Calorimeter", SpaCal) was installed in 1995. Its polar angle acceptance was reduced due to the HERA upgrade and is now $153° < \theta < 174°$. Spatial and energy resolutions are excellent, reaching $\sigma_{pos} = 4.4\,\text{mm}/\sqrt{E/\text{GeV}} + 1.0\,\text{mm}$ and $\sigma_{EM}/E = 0.07/\sqrt{E(\text{GeV})} \oplus 0.01$, respectively [7].
The very forward direction $0.7° < \theta < 3.3°$ is covered by the PLUG calorimeter.
The calorimeters are placed fully inside the iron return yoke to have as few inactive material as possible in the way of the particles. This improves the scattered electron measurements. The iron is instrumented to act as tail catcher for showers that leak from the inner calorimeters and for muon identification.
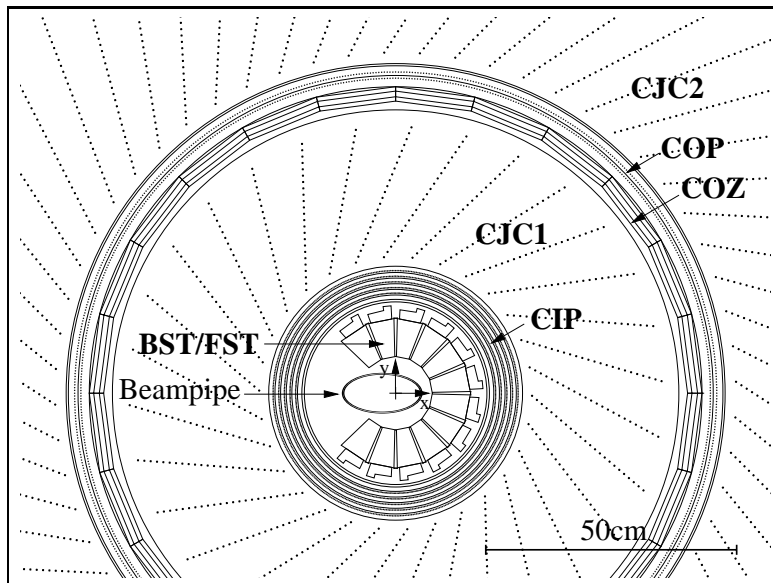
Figure 2.5: Central trackers and the FST/BST in a projective look "down the beampipe" (in negative z direction)

2.2.3   Luminosity system and Additional detectors

H1 measures the luminosity via the Bethe-Heitler reaction $ep \rightarrow ep\gamma$. The photons are detected in a calorimeter ("Photon detector", PD), while for electrons there are various "Electron Taggers" (ET) upstream ($z < 0$).
Other detectors include the "Forward Proton Spectrometer" (FPS) and the "Very Forward Proton Spectrometer" (VFPS), located far downstream at $z \sim 70$ m and $z \sim 220$ m, respectively. They can detect protons scattered with very small momentum transfers and are used for diffractive studies.

2.2.4   Triggering and Readout

The high bunch crossing frequency and large background rates make a difficult system for data readout and triggering necessary. As an ep collider experiment, H1 has to deal with high backgrounds from hadronic interaction and low physics rate given by electroweak interaction. These problems became more severe after the HERA II upgrade and will be discussed separately.
H1 uses 4 trigger levels to reduce the amount of data written to tape while keeping the interesting physics. More abundant processes like scattering at low Q^2 have to be prescaled, effectively lowering the luminosity for these reactions. This way the limited bandwidth can be used optimally. Figure 2.6

gives an overview over the H1 trigger system and associated time scales.
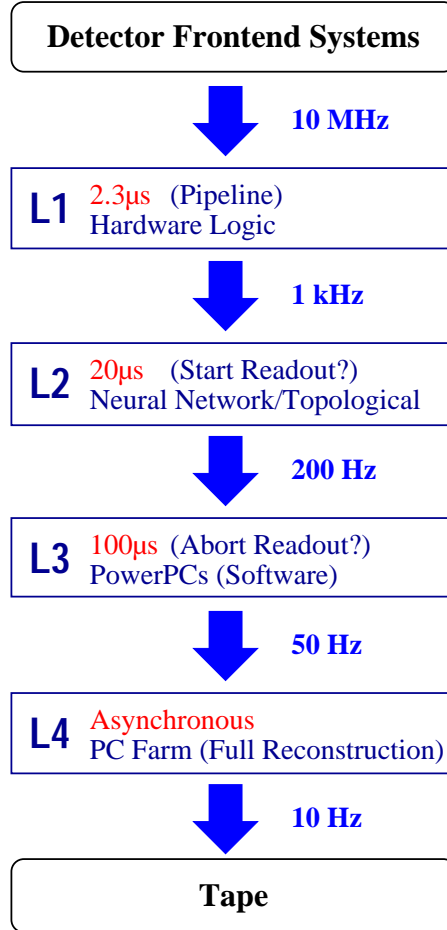
Figure 2.6: The 4 trigger levels of H1 with respective input rates and processing times.

The first level trigger (L1) works dead time free. The various subdetectors providing L1 information, e.g. CJC, LAr, CIP, Muon System, SpaCal, or BSTT have $2.3\,\mu s$ to deliver signals, so called trigger elements (TE) to the central trigger system. This rather long time is needed by the CJC and the LAr to collect the ionization charge. All H1 detectors need to keep their history stored in a pipeline for later readout. The pipeline length has to be at least the L1 decision time.

The trigger elements are combined to subtriggers, that should in the ideal case reflect a certain type of physical event. If the central trigger system decides to keep an event (L1Keep), the pipelines are stopped and the dead time starts.

At L2 refined information from all trigger detectors are used to perform neural network and topological analysis within $20\,\mu$s. This decides on the begin of detector readout.

The new Fast Track Trigger (FTT) at L3 can run more extensive software algorithms and may stop the H1 readout. Decision time is typically $100\,\mu$s. The fourth level trigger is based on a full event reconstruction in a PC farm and reduces the amount of data written to tape further. The rates delivered to the next level are typically 1 kHz, 200 Hz, 50 Hz and 10 Hz, respectively.

2.3   HERA II Upgrade

The instantaneous luminosity achieved by HERA can be written as [8]

$$\mathcal{L} = \frac{I_e I_p \gamma_p}{4\pi e^2 N_B \epsilon_N \sqrt{\beta^*_{xp}\beta^*_{yp}}}\,. \tag{2.1}$$

It depends on the product of beam currents $I_e I_p$, the lorentz factor of the protons γ_p, the number of colliding bunches N_B, the normalized emittance of the proton beam ϵ_N, and the horizontal and vertical beta functions at the interaction point β^*_{xp} and β^*_{yp}. The emittance is determined by the process of beam preparation, while the beta functions reflect the influence of the beam optics [9]. The following relation exists between the transverse emittance ϵ, the beta function β and the beam size σ

$$\epsilon\beta = \pi\sigma^2 \tag{2.2}$$

To make stable running possible, the sizes σ of both beams have to be matched.

The maximum instantaneous luminosity reached at HERA I was $\mathcal{L} = 1.8\cdot 10^{31}\,\mathrm{cm^2\,s^{-1}}$ with beam currents of $I_e = 48$ mA and $I_p = 105$ mA in 180 colliding bunches. In 2000 H1 had collected about 100 pb^{-1}.

To be competitive in further physics topics like heavy flavor studies and physics beyond the Standard Model however, a luminosity upgrade was required and carried out [8]. The most cost effective possibility for increasing the luminosity was to reduce the beta functions. This was done with the introduction of new beam focusing magnets very close to the interaction point, reducing the design beam spot size to $\sigma_x \times \sigma_y = 120 \times 30\,\mu\mathrm{m}^2$. In turn the design luminosity was increased by a factor of 4 to $\mathcal{L}_{\mathrm{desg}} = 7.5\cdot 10^{31}\,\mathrm{cm^2\,s^{-1}}$ and the goal of collecting 1 fb^{-1} until 2006 was set.

The H1 experiment had to be altered in many respects for HERA II:

- Due to the new magnets, higher synchrotron radiation from the electron beam was expected. An elliptical beam pipe was constructed to let the synchrotron radiation fan pass freely through H1. Changes to the detectors closest to the beampipe, the silicon trackers and the SpaCal, were inevitable.

- The trigger system was upgraded in order to improve physics triggering and reject rising backgrounds. This included the complete redesign of the CIP and upgrades of the CJC and LAr based triggers.

- Aging gas detectors were replaced (BPC), rewired (CJC) or redesigned (FTD).

- The Luminosity system was adapted to the new conditions.

Furthermore spin rotators were built to make longitudinal polarized lepton beams available to the colliding beam experiments.

The start of the HERA II physics program in 2001 was not trouble free. Problems with the new accelerator setup and high backgrounds prevented normal operation. This will be discussed in chapter 4.

Nevertheless HERA demonstrated the ability to reach close to the design luminosity and to establish polarized positron beams. Just before the 2003 shutdown, an instantaneous luminosity of $\mathcal{L} = 2.7 \cdot 10^{31}\,\mathrm{cm}^2\,\mathrm{s}^{-1}$ was achieved with beam currents of only $I_e = 37$ mA and $I_p = 69$ mA. As backgrounds limited the total beam currents, only 119 bunches were filled to maximize luminosity. The specific luminosity was just 20% below the design value. Given that the accelerators and detectors can be successfully operated at currents of $I_e = 58$ mA and $I_p = 135$ mA as planned, the luminosity is expected to reach close to the design value. HERA also demonstrated the ability to bring beams in collision with up to 50% longitudinal polarization for the positrons.

Chapter 3

The H1 Silicon Detectors

Silicon vertex detectors have been used in all major particle physics experiments in the last decade because of their good spatial resolution. While all physics profits from more precise track measurements, it is essential for studying heavy flavor decays. Hadrons with open charm or beauty (e.g. produced in photon gluon fusion) decay via weak interaction only, resulting in mean life times of the order $\tau \sim 10^{-12}$ s and decay lengths $c\tau \sim 300\,\mu$m. With silicon detectors it is possible to resolve the secondary decay vertex.

H1 features several silicon vertex detectors [10], which are described in this chapter. The central region is covered by the barrel shaped "Central Silicon Tracker" (CST). Forward and backward region are covered by the "Forward" and "Backward Silicon Tracker" (FST and BST) [11, 12]. Both are composed of several wheels. With these 3 separate detectors, the acceptance of the H1 detector for heavy flavor production is high throughout the kinematic plane, as shown in figure 3.1.

In addition there is also a trigger detector in the backward region, called "Backward Silicon Track Trigger" (BSTT) [13]. Sometimes it is referred to as "BST Pad", as the basic units of the sensors are pads. A special emphasis is given to the BST and BSTT, as they are the main topic of this work.

The beam pipe region around the interaction vertex with all silicon detectors is shown in figure 3.2.

3.1   General Properties of Silicon Detectors

Silicon detectors are the latest tools of experimental particle physicists. I will only discuss their application for particle tracking. As most track detectors they are based on the detection of ionization charge created by the passage of particles through matter. They can supply signals very fast, are ideal for
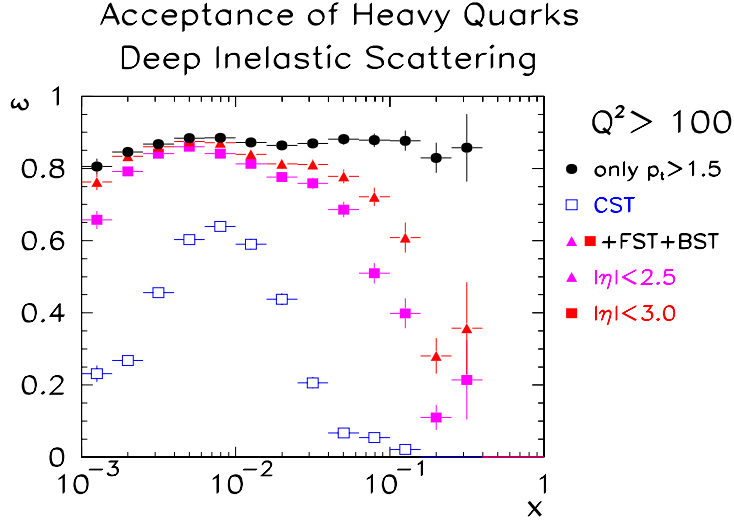
Figure 3.1: H1 Acceptance for heavy quarks in different regions of the kinematic plane. BST and FST cover the regions of low and high x, respectively, hence a reasonable acceptance is maintained over the whole accessible region.

electronic readout, and can have spacial resolution down to $5\,\mu$m. With these combined properties they are superior to any other track detector technique.

3.1.1   Silicon as Detector Material

Silicon is a typical semiconductor. It is used in its crystalline form with a tetrahedral structure. Every atom has 4 valence electrons which are all used to form the crystal lattice. So at 0 K the valence band is fully occupied and there is a gap of about 1.1 eV to the conduction band. Even at room temperature, the intrinsic charge carrier concentration of pure silicon is relatively small. Useful properties are created by doping the silicon, i. e. introducing atoms with different amount of valence electrons into the lattice and therefore creating extrinsic charge carriers:

- Atoms with 5 valence electrons are donators and create new occupied levels just below the conduction band which lead to electron conduction. This is so called n-type silicon.

- Atoms with 3 valence electrons are acceptors and create new unoccupied levels just above the valence band. The holes behave like positive charge carriers and therefore lead to hole conduction. The resulting material is called p-type silicon.
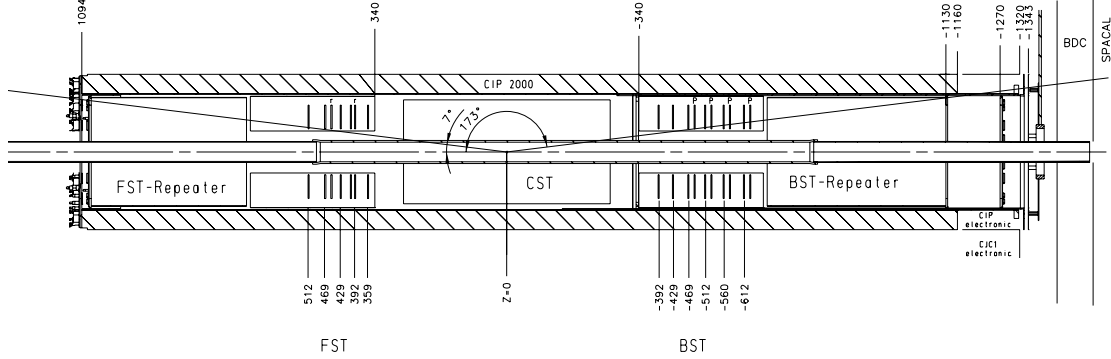
Figure 3.2: View on the region of the silicon detectors in H1. Wheels in the FST with r-strip detectors are marked with "r", the "Pad" planes of the BSTT are marked with "P", all other planes are of the φ-strip type (see section 3.3).

The relative amount of foreign atoms used for doping is in the order of 10^{-5} to 10^{-10}, where application for particle detectors usually needs very little doping only and clean processing.

3.1.2 The Operating Principle of a Silicon Detector

The basic unit of a silicon particle detector is a $p - n$ junction diode. At the junction the two types of charges recombine until an equilibrium with the internal bias voltage $V_{in} \sim 1$ V created by this diffusion is reached. The depletion zone can be widened by applying a large reverse bias voltage. This zone represents the sensitive volume of the detector. Any charge carriers created here will be collected at their respective electrodes where the signal can be read out.

Due to thermal effects and production faults, a constant leakage current will flow through the detector. This is one possible source of noise.

Figure 3.3 shows the basic setup of diodes used for particle detectors. The setup is antisymmetric with the bulk material being lightly n-doped material, while the the p electrode is highly doped (called p^+). This way the depleted region extends mainly into the n-type bulk. Neglecting the small internal bias voltage and the small depletion zone in the p^+ material, the width of the depletion zone is [9]

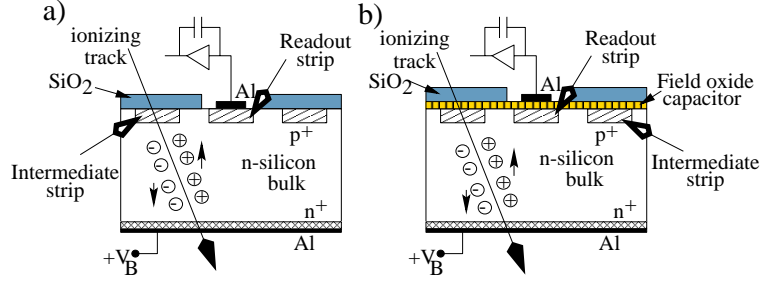$$w = \sqrt{\frac{2\epsilon V_B}{e N_d}}\,, \qquad\qquad (3.1)$$

Figure 3.3: Detection principle of a silicon strip detector. Readout electronics can be DC coupled (a) or AC coupled (b).

with the dielectric constant for silicon $\epsilon = 11.9\epsilon_0$, the elementary charge e, and the n dopant concentration N_d. To fully deplete a 300 μm thick detector with typically $N_d \approx 10^{12}$ cm^{-3}, a bias voltage of $V_B \approx 80$ V is needed. The detector capacitance is

$$C = \frac{\epsilon}{w} \propto \frac{1}{\sqrt{V_B}} .$$ (3.2)

The depletion voltage V_B must be high enough to guarantee a fully depleted and hence very efficient detector. A small capacitance also improves the noise behavior of the amplifier. On the other hand a large bias voltage increases leakage currents and enhances the problems with production faults in long term stability.

3.1.3 Readout and Resolution

The energy needed for the creation of an electron-hole pair is about 3.6 eV, which is larger than the band gap because of the excitation of phonons [9]. Particles to be detected at H1 are in most cases minimum ionizing particles (MIPs). In the most probable case a MIP will create about 32000 electron-hole pairs in a wafer of 300 μm thickness. The amount of created charge is Landau-distributed. Collection time is very fast with about 10 ns for electrons and 25 ns for holes. In principle both charges can be read out. Single sided detectors usually use the charge collected on the p^+ strips. Double sided detectors can determine 2 coordinates at once using also the signal on the n^+ diode, which is technically more challenging.

As the signal is small, a low noise readout chip with a charge sensitive amplifier has to be placed close to the detector. Conventionally the sensor is glued to a "hybrid", which carries the necessary chips. Due to the proximity to the beams and the interaction point, the radiation hardness becomes an issue to consider. This will be discussed in section 6.1.

Figure 3.3 shows a simple one sided detector, where only the signal from the p^+ strip is read out. If a simple DC coupled readout is used, the charge created by leakage currents is read out as well. This can be avoided using an AC coupled detector where each strip has its own coupling capacitance.

To keep the number of channels reasonably small, not all strips are read out, but rather coupled capacitively to each other. Given a proper treatment of

- individual pedestals of each strip,

- coherent readout noise ("common mode", "common slope"),

- charge division and crosstalk effects,

- and detector alignment,

the achievable resolution is much smaller than "readout pitch"$/\sqrt{12}$. Limiting effects in addition to the above mentioned are multiple scattering in the beam pipe and other dead material.

A summarizing quantity for the performance is the "Signal to Noise Ratio" (S/N). Quoted here is usually the most probable value of a Landau distribution. With a high S/N ratio, most noise can be rejected while keeping a high detector efficiency.

3.2 Central Silicon Tracker

The CST is designed to measure precisely the interaction vertex position in the central region. It consists of two barrel layers formed from 12 and 20 silicon ladders (see Fig. 3.4).

After the HERA II upgrade, the support structure was changed to adapt to the elliptical beampipe. The active length of one ladder is 35.6 cm and the total length of the CST is 44.2 cm. One ladder consists of two half ladders, each of these is made of three chained silicon sensors. Each half ladder has a hybrid at its end. The CST sensors are read out from both sides. While this gives a 3D space hit instantly, a threefold ambiguity in z remains and can only be resolved with the help of the CJC. The readout chips were exchanged after some operation time to make the detector radiation hard. The further data transmission is done via multiplexing over optical fiber cables.

The resolution varies from $12\,\mu$m to $23\,\mu$m. A problem is the low S/N ratio of the detector of about 8. This means, that imposing a reasonable cut on S/N will lower the detection efficiency. The angular acceptance for one hit is about $18° < \theta < 162°$, requiring hits from both layers lowers the angular coverage to about $29° < \theta < 151°$.

p–side: **n–side:**

rϕ–strips
25 μm implant pitch   34 mm
50 μm readout pitch

z–strips
88 μm pitch

aluminium wire bonds

640 readout lines
on 2nd metal layer

carbon fiber rail
221 mm

Ceramic
Hybrid   Readout Chips

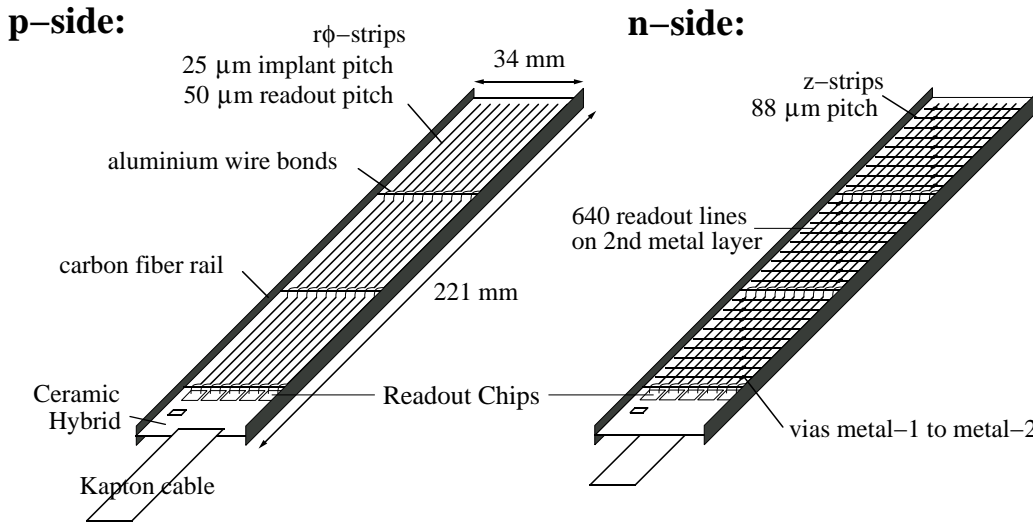vias metal–1 to metal–2

Kapton cable

Figure 3.4: The CST Half Ladder

3.3   FST and BST Strip Detectors

FST and BST detectors are very similar in structure. Both were constructed
and are maintained mainly by DESY Zeuthen. While the FST is a com-
paratively new detector and was introduced only in the HERA II upgrade,
the BST has been in operation for a much longer time [14]. During that
time there were several modifications, the latest just in the 2003 shutdown
[12, 11].

Figures 3.2 and 3.5 give an overview of the layout and spacial dimensions
of the 2 silicon trackers. Both are composed of an active volume in the
part close to the interaction point and a "repeater" section with additional
readout components. The active volume is made up of several planes, each
having the form of a wheel. One wheel carries 12 wedge shaped sensors on
each side. For the HERA II setup one quarter of the wheels had to be freed
for the elliptical beam pipe, so acceptance in ϕ is only 270°. The FST covers
the very forward region of $7° < \theta < 19°$, while the BST acceptance lies in
the range $163° < \theta < 174°$.
Six Repeater boards distribute supply voltages and provide line drivers for
the readout of one double sector. The support structure is made of carbon
fiber and aluminum. Water cooling is provided for the repeater boards and
the hybrids. The whole unit is flushed with dry nitrogen and covered by a
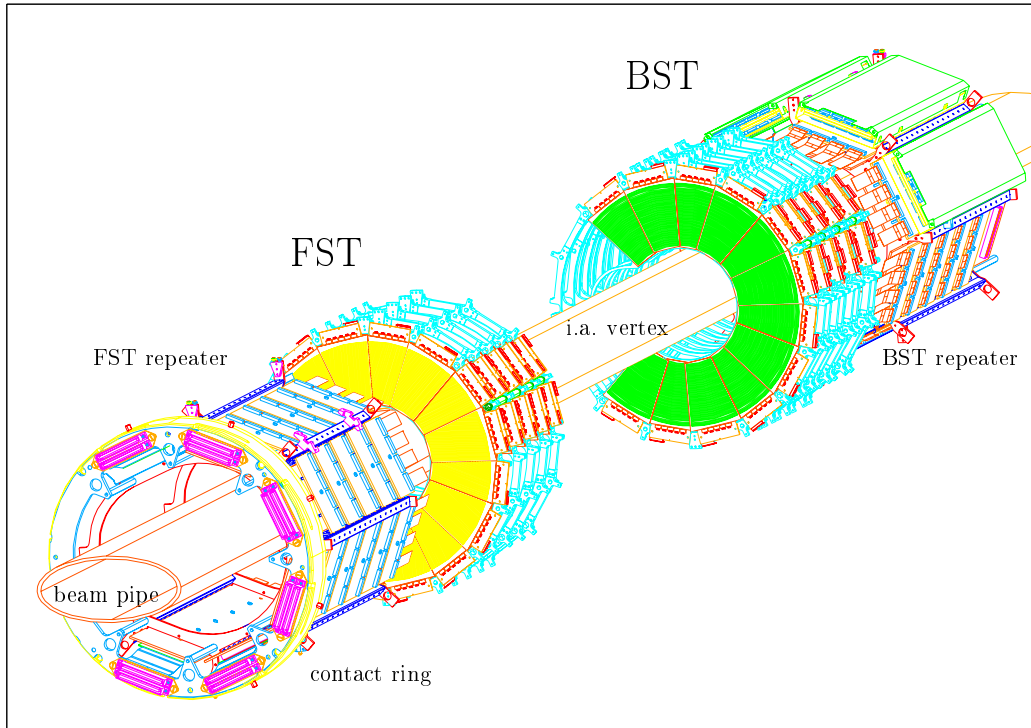thin copper shield.

Figure 3.5: FST and BST

3.3.1 The Strip Detector Modules

The main type of sensor used in the BST and FST is a simple, single sided, single metal strip sensor. These are referred to as "φ-strip" or "u/v" type detectors. Figure 3.6 shows a scheme and photograph of a module, the internal structure is revealed in the cross section 3.7. One sensor covers 22.5° in ϕ from $r = 5.9$ cm to 12.0 cm, so 12 modules are needed for each side. Some overlap in ϕ is used for internal detector alignment. The strips of a second sensor mounted back-to-back on the same wheel cross the former strips at an angle of 22.5° and allow full track reconstruction. A new reconstruction directly using these "u" and "v" coordinates is currently being developed. The FST contains 5 wheels equipped with "u/v" detectors, while the BST has 6 of these.

To resolve ambiguities, the FST also contains two wheels with another detector type, called "r-strip" sensor. This is a single sided, double metal sensor with curved readout strips concentric to the z axis. Experience has shown, that the r-strip sensor works satisfactory with S/N of about 13 [15]. However the φ-strip type was found to have much superior performance. This is the reason to replace all remaining r-strip sensors in the BST in the 2003
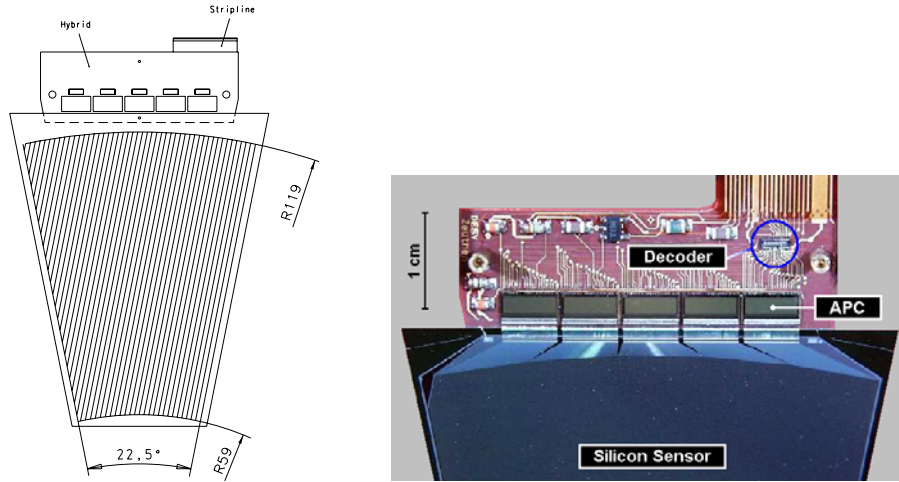
shutdown.

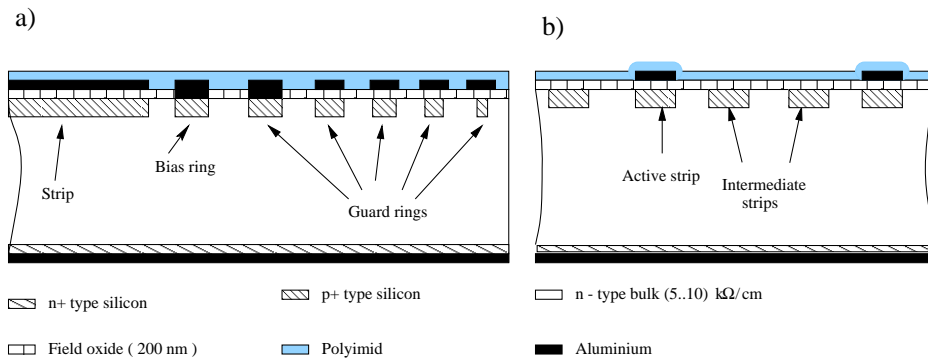Figure 3.6: A single φ-strip detector module

Figure 3.7: Cross section of a φ-strip module in strip direction (a) and perpendicular to the strips (b).

The layout of the φ-strip module is very close to the general scheme described above. It was designed by DESY Zeuthen. MPI Munich developed the production masks which were then written at Siemens. The production was carried out by CIS Erfurt.

The silicon bulk is 280 μm thick. The p^+ strips are ion implanted on the front side of the n-type silicon bulk. They are parallel to one of the detector edges. The n^+ anode on the back side is made by high temperature diffusion. It covers the whole backplane, the surface of which is completely covered with an aluminum layer. The readout electronics is AC coupled via a field oxide layer of about 200 nm thickness. A guard structure around the bias ring

avoids distortions of the electric field at sensor edges.

The distance between neighboring strips is $25\,\mu$m. Every third strip is read out (see figure 3.7b), resulting in a pitch of $75\,\mu$m between the 640 readout strips.

Contact to the readout elements is provided by small pads at the top edge of each strip. Two larger contact pads for the bias voltage and the guard ring are in the upper corners of the sensor. All strips need a sink for the leakage current. Therefore they are connected via a so called "punch–through" transistor to the bias structure. For this a n-channel FET is created at one end of the strip by the gap of n-type material between the p^+ structures. The inner guard ring is also connected by "punch through" to the bias (see figure 3.7a).

3.3.2   Strip Hybrid and Readout

The whole sensor is fixed on a small circuit board with conducting glue. This hybrid contains the 5 readout chips "APC128" ("Amplifier and Pipeline Chip with 128 channels") and auxiliary control elements. Each strip is connected to one input of the APCs. In sampling phase the signals are preamplified and the 32 latest entries are stored in an analog pipeline, corresponding to a history time of about 3.1 μs and therefore enough for the L1 trigger decision. When the H1 Trigger System decides to start readout of an event, the pipeline charges of the corresponding time slice are transfered to a latch capacitor and amplified again. As the number of available channels to the H1 DAQ system is limited, the 1280 signals of 2 detector modules have to be read out serially. All together the BST and FST Strip detectors have both about 100,000 channels. The whole readout is a rather lengthy process of at least 800 μs, making the system one of the slowest in H1.

The readout chip is of special interest concerning the radiation hardness as will be described later in chapter 6. The rest of the readout chain is described elsewhere [16, 17].

3.3.3   Physics Performance

After the HERA II upgrade the FST was one of the best working detectors. Data analysis has started, but as running conditions were bad, no serious results were obtained so far. The BST was repaired in the 2003 shutdown, a process that will be described in more detail in chapter 6.

Two plots demonstrating the performance of the φ-strip modules from the FST are shown in 3.8: the S/N ratio of 30 is exceptionally high and the

spacial resolution of about 11 μm is very high considering the readout pitch
of 75 μm.
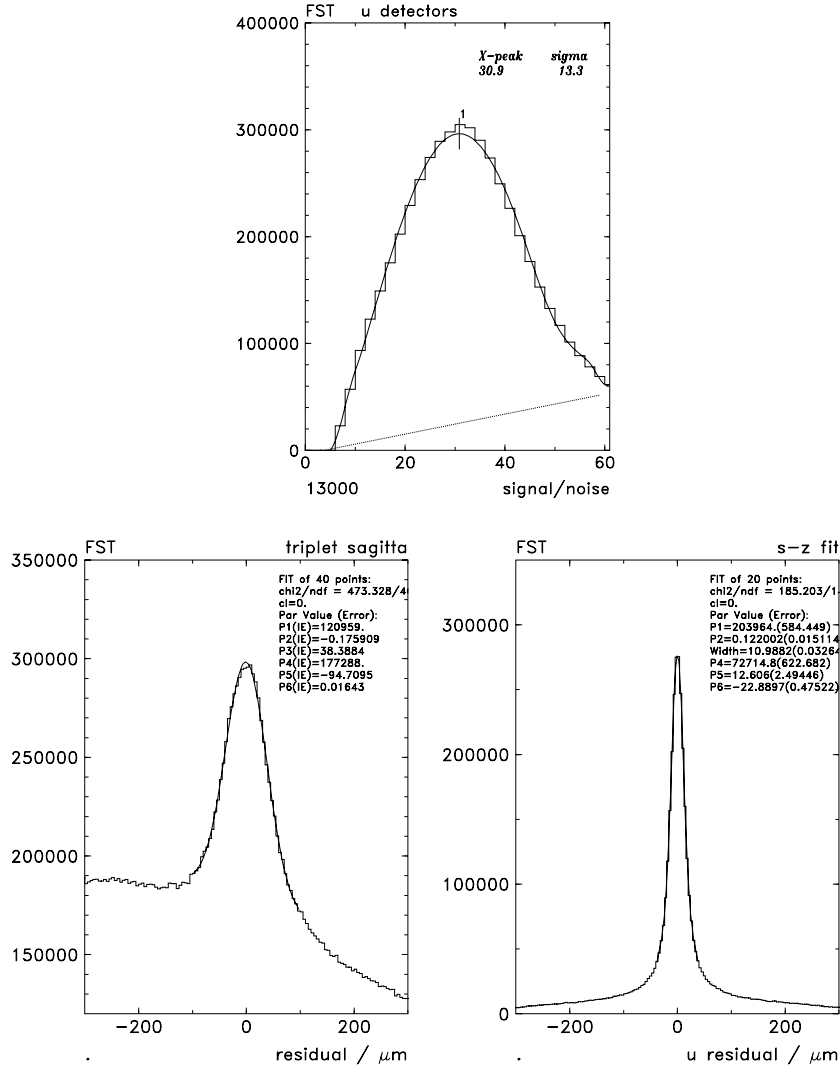
Figure 3.8: Above: Signal/Noise ratio for the φ-strip type, Below: Performance of the FST. Resolution perpendicular to the strips is about 11 μm as can be seen in the right figure

In figure 3.9 two events are shown with the electron reconstructed in
the BST or FST, respectively. The high precision of the silicon detectors
improves reconstruction significantly, especially as resolution degrades at the
edges of the kinematic plane. Because the silicon trackers are the first ones
to record a charged track with a minimum of dead material in front, they
have distinct advantages:

- At low Q^2 the BST can differentiate charged tracks, i. e. electrons, from high energy photons created within the hadronic final state.

- At high Q^2, where the scattered electron can have energies of several 100 GeV, track detection before showering enhances the possibilities of lepton identification.

3.4 The BST Pad Trigger Detector

In addition to the 6 planes of strip detectors, the BST also contains 4 planes of detector modules composed of pads. As for the strip detectors, one quarter of the wheels had to be freed for the new elliptical beam pipe of the HERA II setup. Now there are 12 modules per plane, each covering 22.5° in ϕ.
In contrary to the strip system, the pad system has much fewer channels and advanced logic systems mounted inside the detector on 6 "repeater boards". With this setup it is a very fast detector suitable for Level 1 triggering.
The BSTT in its present form is still under development. Radiation damage and background problems prevented trouble free operation. First results are presented in chapter 5.

3.4.1 General Trigger Idea

The acceptance of the BST lies in the region of small Q^2. DIS Events have usually a very clean signature here: the electron is scattered at a small angle, its track can be measured in the BST and the BPC, while the SpaCal provides cluster measurement with very good spacial and energy resolution. At high y the hadronic final state is also projected into the backward region, but it is well separated in ϕ and can be differentiated easily. Triggers available so far were the CIP and the SpaCal. The CIP trigger is limited in acceptance to $\theta \lesssim 169°$, so the SpaCal is the only efficient trigger in the region of lowest Q^2.
A problem in this interesting region is the photoproduction background at $Q^2 \sim 0$. Here the scattered electron escapes down the beampipe and is usually not detected at all. On the other hand, photons produced within the hadronic final state from $\pi_0 \rightarrow \gamma\gamma$ also create an electromagnetic cluster in the calorimeter. The trigger rate of photoproduction events rises steeply with lowering the trigger energy threshold, all together the rate is about 100 times higher than for DIS events. The only way to control this background online was to raise the energy threshold of the trigger. This however makes
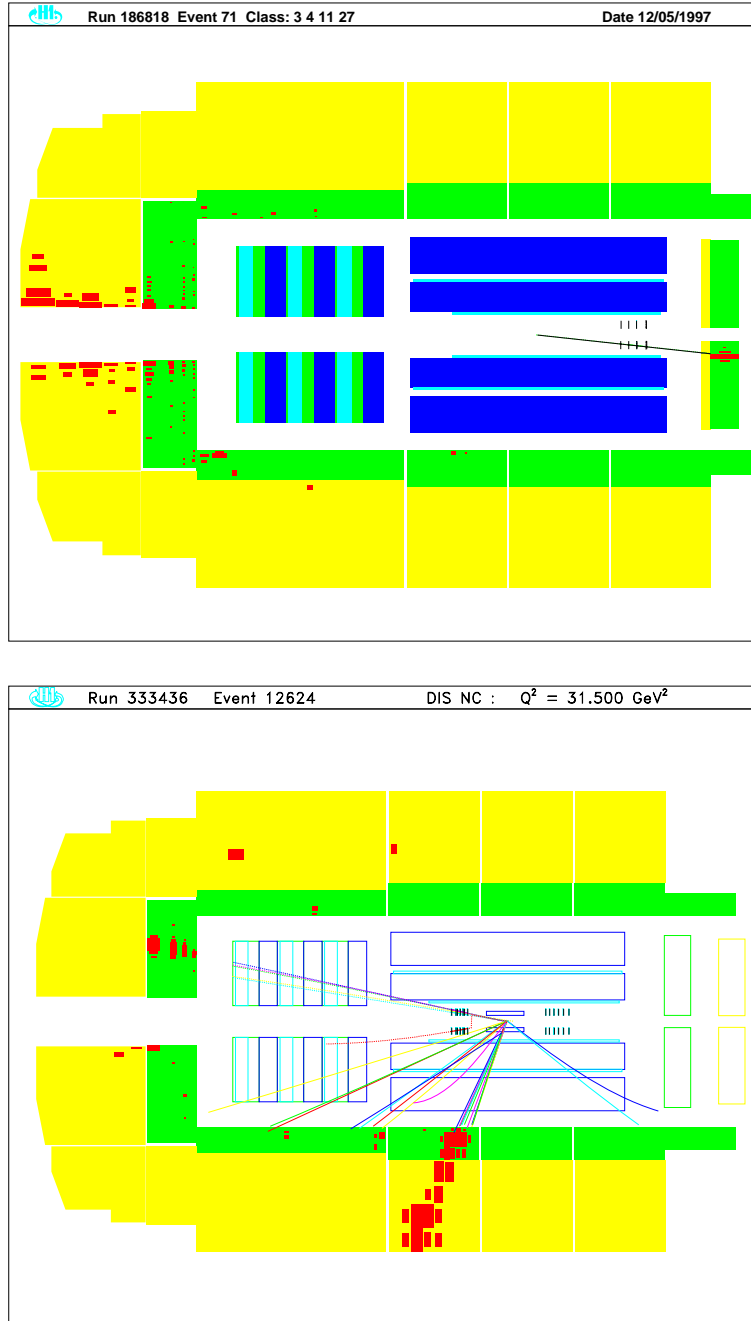
Figure 3.9: Above: Low Q^2 event with electron reconstructed in the BST, Below: High Q^2 event with electron reconstructed in the FST

it inefficient for high y, which is exactly the region of interest for F_L measurements. With a track requirement, neutral background can be rejected. Up to now this was done offline using the BST to identify neutrals and to subtract charge symmetric background [3].

The main reason for introducing the BSTT is to be able to do the background suppression online. Photons from photoproduction have a very small probability of creating a track signature and therefore the associated cluster in the SpaCal can be rejected. This makes it possible to lower the energy threshold and reach the high y region.

As track multiplicities for DIS events in the backward region are generally low, the trigger detector does not need fine granularity. On the other hand, the backward region is the origin of large proton induced backgrounds with very high charged track multiplicities. These are often triggered without appropriate veto. The BSTT is able to provide such a high multiplicity veto.

For the sensor a setup with silicon pads divided into 8 concentric rings was chosen. Vertex pointing tracks are identified as correlation of signals in at least 3 out of 4 planes. Patterns of ring numbers code the track signatures and can be compared to stored "masks". For example the pattern "2345" corresponds to a particle entering the detector in ring 2 in the first plane and leaving it through ring 5 in the fourth plane. Figure 3.10 illustrates this idea. The masks can be derived from simulation or offline data analysis.
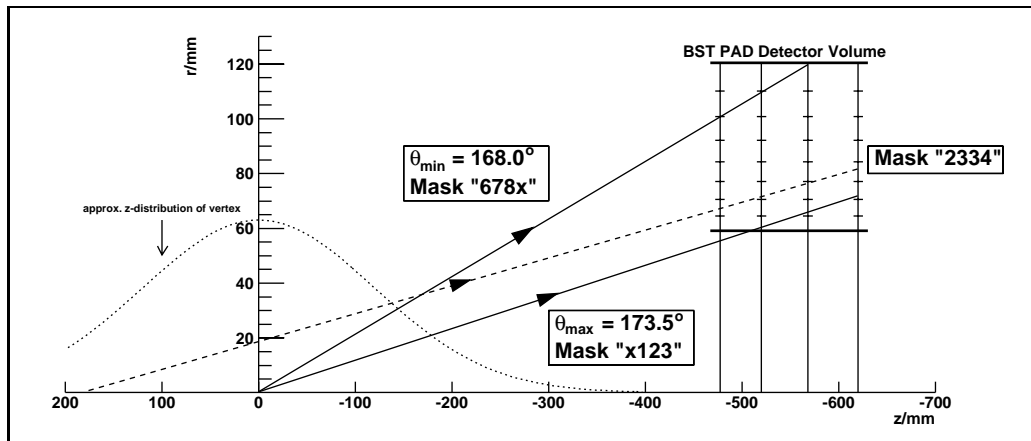

Figure 3.10: Scheme describing the BST Trigger concept. The 4 trigger planes with their radial divisions are shown. Straight tracks are identified with certain masks. For tracks originating from the nominal vertex, the maximal angular coverage is shown (solid tracks). Due to vertex spread (dotted line), additional masks have to be considered (dashed track).

To get trigger roads pointing to the vertex with the same detector modules in every plane, the following relation between the z positions of consecutive planes $z_n, n = 1 \dots 4$ and the radial subdivision of each detector module into the 8 rings with outer radii $r_m, m = 1 \dots 8$ has to be fulfilled:

$$\frac{z_{n+1}}{z_n} = \frac{r_{m+1}}{r_m} = \text{constant } \forall n, m \,. \tag{3.3}$$

Space is limited in radial direction by the CIP and the beampipe, constraining the outer and inner edges of the silicon sensor to $r_0 = 59.0$ mm and $r_8 = 120.4$ mm, respectively. In z direction the superconducting focusing magnet GG limits space, so the planes are located between about $z_1 = -477$ mm and $z_4 = -620$ mm. With this setup, the angular acceptance in θ is about $168° \leq \theta \leq 173.5°$ for tracks from the nominal vertex.
Only considering tracks from the nominal vertex, one would have compare measured patters with very few masks: because of the above mentioned trigger road setup just 7 patterns with 4 hits are possible. However, vertex smearing and beam offsets enlarge that number. A total number of about 50 masks has been shown [18, 19] to be fully efficient for current HERA conditions. Coding more masks would also lead to higher acceptance of background events.

3.4.2   The Detector Module

The PAD sensor was designed by DESY Zeuthen and produced by MICRON Semiconductor Ltd. with a technique similar to the strip modules. Shape and size are almost identical. A schematic view and a photograph are shown in figure 3.11.

The sensor is 380 μm thick. The p^+ active structures are pads with surface areas from 33.3 mm^2 to 115.7 mm^2. The typical bias voltages for full depletion is $V_B = 50$ V. The capacitances in depleted regime range from 15 pF for the smallest to 50 pF for the largest pads. This leads to higher noise for the larger pads.
One sensor is made up of 32 pads, organized in 8 rings of 4 pads each. The area of the AC coupling aluminum contacts is the same for all pads. The remaining area which does not compose the coupling capacitor, is DC coupled and connected to the p^+ silicon. Biasing is done using the FOXFET technique. The effect is similar to the one in the φ-strip sensors. A guard ring surrounds the active area for shaping the fields at detector edges. A cross section through the module is shown in figure 3.12.

The silicon module is glued onto a hybrid, which contains the readout chip PRO/A. It is a so called ASIC (Application Specific Integrated Circuit) and
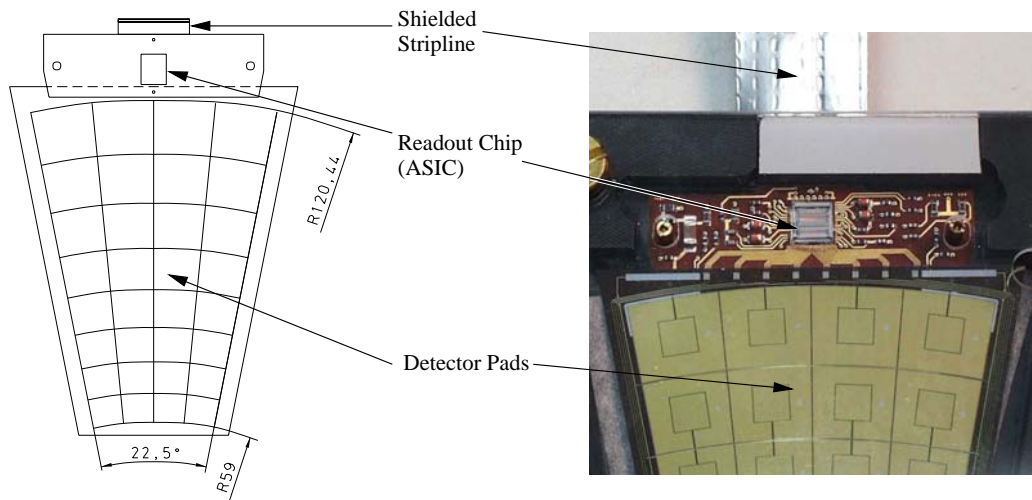
Figure 3.11: A schematic drawing and a photograph of a BST Pad detector module
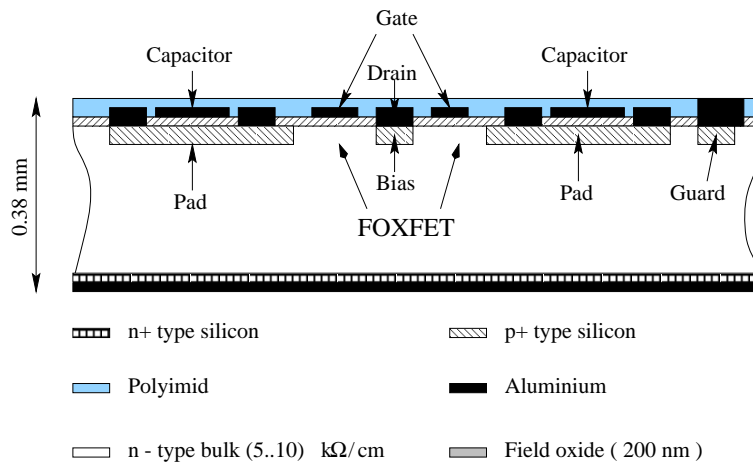

Figure 3.12: The Pad Module in cross section

was designed in collaboration with IDE AS in Oslo, Norway [19]. The chip has 32 channels with analog and digital outputs. Every channel is connected to one pad. The chip provides charge-sensitive amplification with variable gain and signal discrimination with adjustable thresholds. An important feature of the PRO/A chip is the analog common mode subtraction. This feature suppresses noise by subtracting the signals of two neighboring pads from each other. For the strip detectors a similar procedure is done during the readout phase using the digitized signals. The output consists of the logical OR for all pads of one ring, i. e. just 8 signals from one detector.

The chip steering is done via a 72-bit control register. The register content
has a default "power on" configuration, but it can be changed during running.
E. g. single channels can be deactivated or test pulses can be injected from
the repeater board to test the trigger algorithms.

3.4.3   The Repeater Board

As Level 1 trigger detector the BSTT has to provide L1 trigger information
for every bunch crossing. Due to the limited number of channels for data
transmission to the H1 DAQ systems, data reduction has to be done on
the repeater boards inside the detector. This includes track validation and
multiplicity calculation. Due to radiation damage, the board design had to
be redone in 2003. This will be discussed in section 6.3. The new repeater
board is shown in figure 3.13.

Every board provides full control over one of the 6 double sectors, each
containing 8 detector modules. The board contains two complex program-
mable logic devices (CPLD) from the "ALTERA" family [20]:

- The "ACEX" EP1K30 is responsible for Slow Control functions like
  changing threshold setting, providing supply voltages for the pad mod-
  ules, downloading or verifying of PRO/A ASIC codes, and issuing cal-
  ibration pulses.

- The "APEX" EP20K300E performs signal synchronization, raw data
  pipelining, the online trigger data analysis, and finally coding of the
  output. The trigger analysis is based on masks stored in a "Content
  Addressable Memory" (CAM). This enables very fast comparison of
  the latest detected pattern with all stored masks. The CAM lookup
  mechanism provides the possibility of "do not care" values. With this
  it is possible to react in a flexible way to dead channels or to decrease
  the number of hits required for track verification.

These devices are configurable to a very high extend. Programming is
done in the platform-independent "VHSIC (Very High Speed Integrated Cir-
cuits) Hardware Description Language" (VHDL). A power on configuration
is stored in non volatile memory units (EPROMs). For configuration of the
CPLDs and their EPROMs the JTAG bus is used. All other Slow Control
functions use the CAN bus interface provided by the ATMEL T89C51CC01
controller [21].
The trigger data is transmitted via a screened copper cable using the dif-
ferential line drivers HS-26CLV31RH and their complementary receivers HS-
26CLV32RH [22]. The 8 bits therefore use 16 lines for noise resistant data

Striplines from detectors
(2 sectors x 4 planes)

Depletion Voltage (HV)

ALTERA APEX
(Trigger)

Phi Bus (connection
to other sectors)

Line Driver

Nitrogen Cooling

Power On Config.
for ALTERA

Temparature Sensors

CAN Controller
(Slow Control)

CAN Bus
(to next sector)
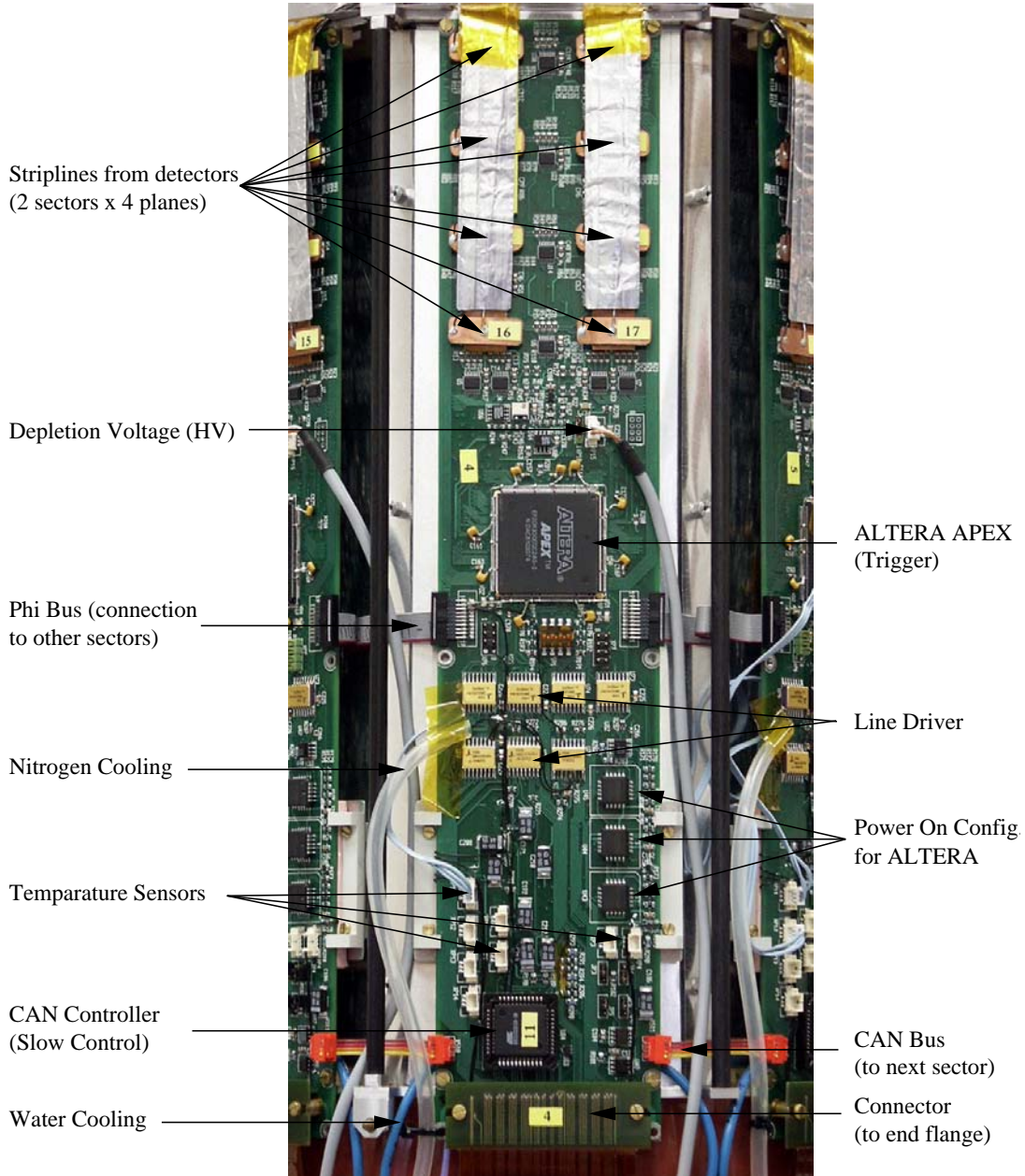
Water Cooling

Connector
(to end flange)

Figure 3.13: The new BSTT repeater board mounted on the BST support structure. The backside of the board carries additional components like the ALTERA ACEX Slow Control Processor and voltage regulators.

transmission synchronous to the HERA clock.

The data output from the front-end has two modes. During sampling phase the data reduction processor is sending out validated tracks with polar angle or hit multiplicities. These are the two basic capabilities of the trigger [19]. In addition, the radiation monitor signal is transmitted continuously. After L1Keep is announced by the H1 DAQ, the readout phase starts. Here additional data, i. e. raw data from the pipeline, is multiplexed to the output to be used by the L2 triggers.

3.4.4   The VME Modules

Various VME modules were designed to integrate the BSTT into the H1 DAQ and the H1 central trigger system [19]:

- Two "Trigger Cards" cards untie high density cables coming from the detector, adapt signal levels to the H1 standard, provide the data fanout, distribute the HERA clock frequency and H1 control signals for the whole BSTT and prepare the "front-end ready" (FER) signal.

- The "Master Card" unifies data streams of all 6 repeaters and takes the final trigger decision. It uses the reduced data with validated tracks and hit multiplicities from the whole BSTT. The L1 trigger elements TE192 to TE199 are delivered.

In addition there are modules providing Slow Control functions which are described later together with their respective functions.

Chapter 4

The Background Situation at HERA II

After the restart of beam operation in 2001, HERA and the collider experiments faced many problems, most of which can be related directly or indirectly to the upgrade. They hampered regular operation close to design luminosity. Many of the physics goals for the HERA II phase were formulated for an integrated luminosity of the order 1 fb^{-1}. The search for the origin of the problems and possible solutions had highest priority. A "Background Task Force" group (BGTF) was formed to investigate the situation. Two DESY internal reports were published on this subject [23, 24]. The Radiation Monitor rate provided by the BSTT was one of the major background indicators. Consequently one of the subjects of this thesis is the analysis of data collected by background monitors. The results presented here were published in [24].

4.1   The Upgrade Impact

The HERA luminosity upgrade brought about a redesign of the beam line close to the collider interaction points. The higher luminosity was to be achieved mainly through better beam focusing. Therefore new magnets were introduced, the most prominent being the superconducting quadrupole magnets GG and GO in backward and forward region close to the interaction point. The main problem of the lepton beam focusing is the associated production of synchrotron radiation. The power dissipated by synchrotron radiation, given in SI units by

$$P = \frac{2}{3} \frac{I_e e}{4\pi\epsilon_0} \frac{\Delta\phi}{\rho} \left(\frac{E_e}{m_e c^2} \right)^4 ,$$ (4.1)

depends on lepton energy E_e, current I_e, bending angle $\Delta\phi$, and bending radius ρ. The bending radius at HERA II is $\rho = 400$ m, about 3 times smaller than at HERA I. This results in an increase of the radiated power to about 12 kW. The synchrotron radiation spectrum is continuous. It can be characterized by the critical energy E_C, defined as the median in the dissipated power spectrum. E_C also depends on the bending radius as $E_C \propto \rho^{-1}$, therefore radiated photons have higher energies compared to HERA I conditions. Figure 4.1 shows the simulated spacial distribution of the generated radiation fan in the H1 region.
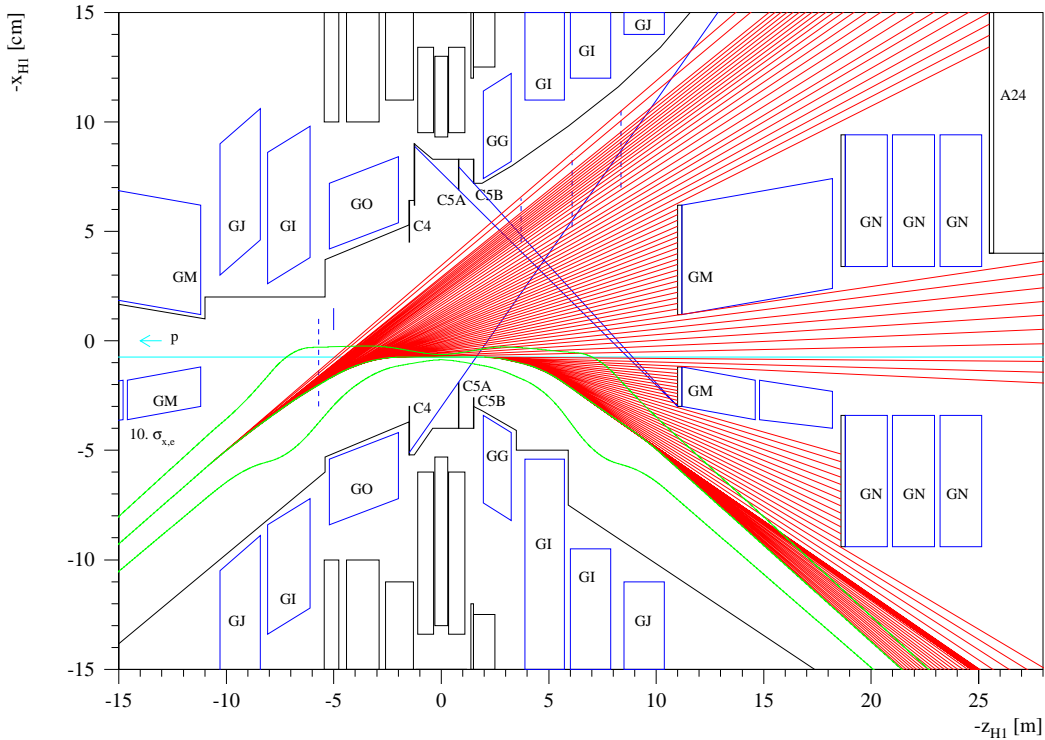

Figure 4.1: Simulated synchrotron radiation fan in the horizontal plane due to the new beam focusing strategy. Note the different scales of the axes. C4, C5A, and C5B are collimators, magnets are labeled with Gx.

All detectors have to be protected against direct synchrotron radiation. Otherwise the consequences would be additional hits in the track detectors, ageing of the gas chambers and damage of electronics and silicon trackers. The new elliptical beampipe was designed to let the radiation pass by the detector region. A system of absorbers and collimators should let only doubly scattered radiation reach the detector. Absorbers are produced with a special coating against backscattering of incident synchrotron photons. The general strategy is to use a high Z material like tungsten as absorber core.

Several layers of medium Z (silver) and lower Z materials (copper) are applied to absorb fluorescence lines.

Synchrotron radiation also causes vacuum deterioration. When the photons hit elements of the beam line and heat them up, gas originally trapped at the surface is freed. This is known as "dynamic pressure increase". Another source of heating can be excitation of "higher order modes" especially at lower lepton beam energies where bunches are shorter. This effect typically shows up near beam collimators that form cavity-like structures, so that electromagnetic waves are produced resonantly by the accelerated particles.

High pressure in the beam pipe leads to more frequent beam–gas interactions. Most important is the proton–gas interaction, as the cross section is larger than for electron-gas scattering and showers have higher multiplicities. The effects of high beam–gas background are the same as described above for direct synchrotron radiation. A certain limit must not be exceeded for safe longterm operation of the detectors. The HERA II setup brought about a much higher material density in the beam pipe region due to new magnets and collimators. Secondary interactions in this material are therefore likely, resulting in the development of showers with high average charged multiplicities [24].

Data taking is affected by high backgrounds as well. Trigger conditions are often fulfilled with a larger number of tracks if no appropriate veto is applied. For example the CIP was not fully operational after the startup due to technical difficulties. Therefore the z-vertex trigger was not available. This led to triggering lots of background events originating from interactions in collimators, see figure 4.2. These events use up a large part of the limited DAQ bandwidth.

The beam steering can have a large influence on the background. But given "optimal" particle orbits, conditions will obviously depend on the beam currents. These in turn had to be far below the design values. Running with reduced currents helped to disentangle different contributions of background and to find an optimal strategy for improvements.

4.2 The Background Monitors

During beam operation the running conditions have to be monitored online to avoid permanent damage of the detectors. Several detectors were designed as dedicated monitors, others deliver background information in addition to their standard data. Most detectors count hit rates, while gas chamber measure the total current through the sense wires. In the following these quantities, which often have a linear dependence to the ionizing dose
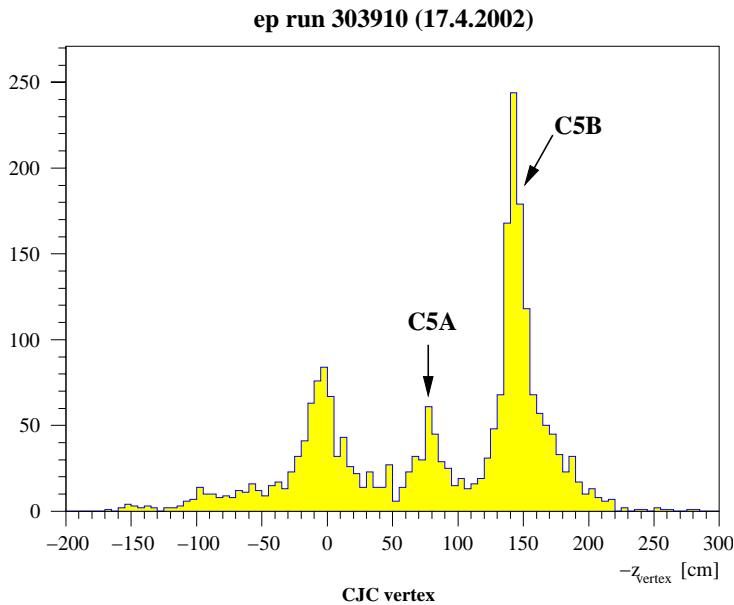
ep run 303910 (17.4.2002)

Figure 4.2: CJC z vertex distribution. In addition to interactions at the nominal vertex $z = 0$, there are lots of background events originating from the collimators C5A ($z = -80$ cm) and C5B ($z = -145$ cm).

and are directly related to ageing effects, are referred to as background indicators. Measured values can be compared to some theoretically calculated limit, which might involve rather high uncertainties. Long term experience is often preferable as source of reasonable operation limits.

The two most important indicators used in 2002/3 running were the "H1 Radiation Monitor" rate delivered by the BSTT and the current in the CJC. Other indicators used are the "e background" and "p background" scintillation counters and the SpaCal rates. These are monitored during normal runs and special tests, like intentional changes in the vacuum system.

In the following the long term development is investigated to learn about background sources and their individual development. Figure 4.3 shows a sample run with stable conditions. Injection and beam steering time as well as spikes caused by temporary instabilities have to be excluded from the analysis.

Beam currents, indicator data and auxiliary information was read from the HERA archives as text files, filled into a ROOT [25] Ntuple and processed further. ROOT provides convenient functions for χ^2 fitting of standard and self defined functions.

The basic idea is to fit a simple model function to a background indicator B, where B could be any measured rate or current. Several additive contribu-
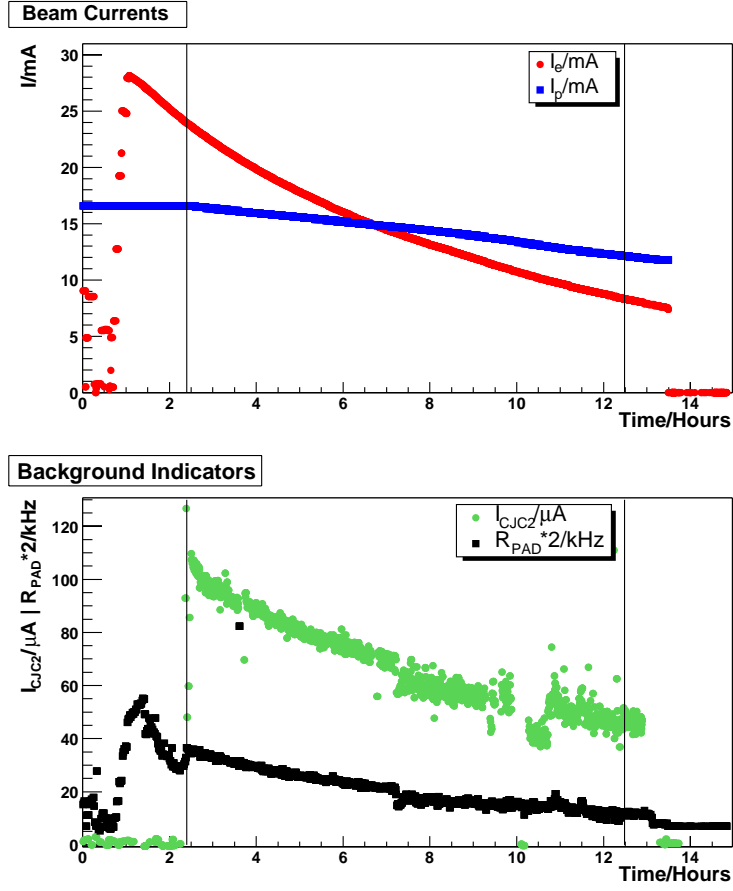
Figure 4.3: Sample run in 2002 used for background studies. The behavior of the two indicators: Radiation Monitor rate R_{RM} and total current in the CJC2 I_{CJC2} can be studied as function of the beam currents I_e and I_p. During the short period around 10 hours the CJC was switched off.

tions to B are expected:

- a small pedestal value independent of time and beam conditions α_0,

- a contribution from direct synchrotron radiation $\alpha_{SR}I_e$, which is proportional to the positron current,

- a contribution from positron beam–gas interactions $\alpha_e I_e \langle P_L \rangle$, which is proportional to the positron current and the mean pressure left of the interaction point folded with detector acceptance $\langle P_L \rangle$,

- a contribution from proton beam–gas interactions $\alpha_p I_p \langle P_R \rangle$, which is

similar, but sensitive to the mean pressure right of the interaction point $\langle P_R \rangle$.

As was mentioned before, the pressure in the beam pipe changes dynamically as soon as positrons are injected. Figure 4.4 shows pressures measured with ion getter pumps close to the interaction point in negative z-direction. With the exception of very high positron beam currents I_e and bad vacuum conditions, a linear fit can be used to describe the data. Thus the relations $\langle P_L \rangle = P_L^0 + \gamma_L I_e$ and $\langle P_R \rangle = P_R^0 + \gamma_R I_e$ are obtained.
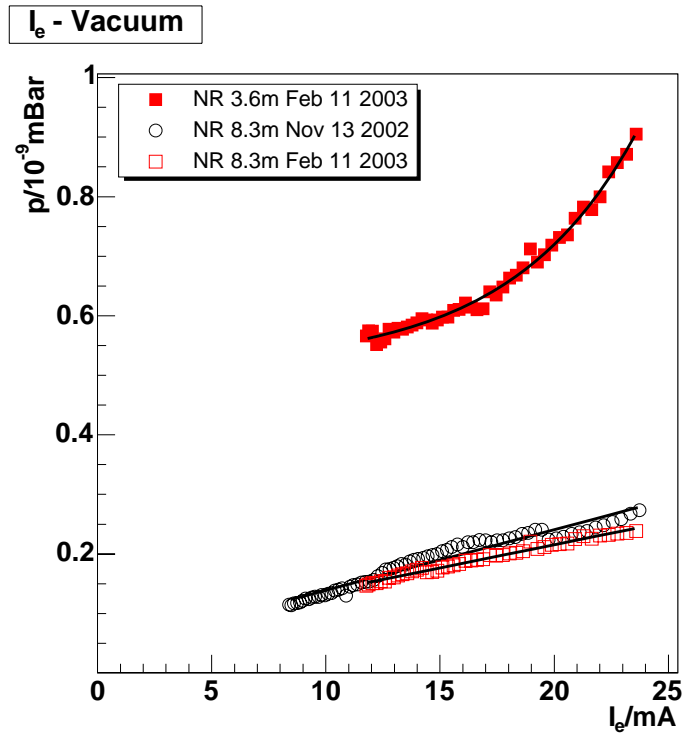

Figure 4.4: Correlation positron current I_e and pressure in the ion getter pumps NR3.6 and NR8.3 located at $z = -3.6$ m and $z = -8.3$ m, respectively. At least for small pressures the relation is about linear.

Adding all contributions and using the relations for $\langle P \rangle$, one obtains:

$$\begin{aligned} B &= \alpha_0 + (\alpha_{SR} + \alpha_e P_L^0)I_e + \alpha_e \gamma_L I_e^2 + \alpha_p P_R^0 I_p + \alpha_p \gamma_R I_e I_p \\ &= a_0 + a_1 I_e + a_2 I_e^2 + a_3 I_p + a_4 I_e I_p \, . \end{aligned} \tag{4.2}$$

Making a fit to the data with the free parameters a_0 to a_4, it is possible to

- determine the most significant sources of background,

- present the background dependence of single runs as a function of only I_e while keeping I_p constant (the beam lifetime for the protons is much larger than for the positrons),

- monitor improvements by calculating rates that are directly comparable at a common I_e and I_p,

- and finally extrapolate to design currents and identify dominant contributions for this scenario.

Conditions within a run tend to fluctuate because of beam steering or technical problems. To get meaningful results for the long term development, the first task is to select long, stable runs like the one presented earlier in figure 4.3. In addition the fit procedure is done in a special way to be less sensitive to short term influences:

- From positron only runs ("e only") the parameters a_0, a_1, and a_2 are determined by fitting a quadratic polynomial. It was checked, that especially the pedestal a_0, and the contribution due to direct synchrotron radiation and base pressure a_1 were long term stable. The dynamic positron–gas part a_2 is however adapted to the running period.

- Using these results, the indicator measurements from luminosity running ("ep") are reduced to the proton–gas contribution and parameters a_3 (proton–gas, base pressure) and a_4 (proton–gas, dynamic pressure) are extracted from a linear fit.

4.2.1 The H1 Radiation Monitor

The silicon detectors are the most vulnerable parts of a collider experiment: they are placed closest to the beampipe and interaction point and their readout electronics has to be implemented close to the detectors. Therefore it is natural to have some device to monitor background conditions located in the vicinity of the detector. The BSTT trigger logic was programmed to deliver the Radiation Monitor signal [19]. One of the H1 trigger elements is used to transmit the number of hits collected within the last second. The signal is synchronous to the HERA clock, so the dynamic range is up to 10 MHz. The continuous rate for safe longterm operation is approximated to be about 50 kHz (see also chapter 6).

The coefficients of equation (4.2) are determined for the Radiation Monitor rate. The resulting fits for a few sample runs are given in figure 4.5. Both, the pedestal and the contribution of synchrotron radiation are negligible ($a_0, a_1 \sim 0$). This is consistent with expectation: typical synchrotron

photons with $E_\gamma \sim 100$ keV have a mean free path of the order 1 cm [9]. This means that only a few percent of the photons interact in the thin silicon detectors. Also the typical energy deposition of a single photon is lower than for a minimum ionizing particle [10] and therefore not likely to exceed the signal threshold.
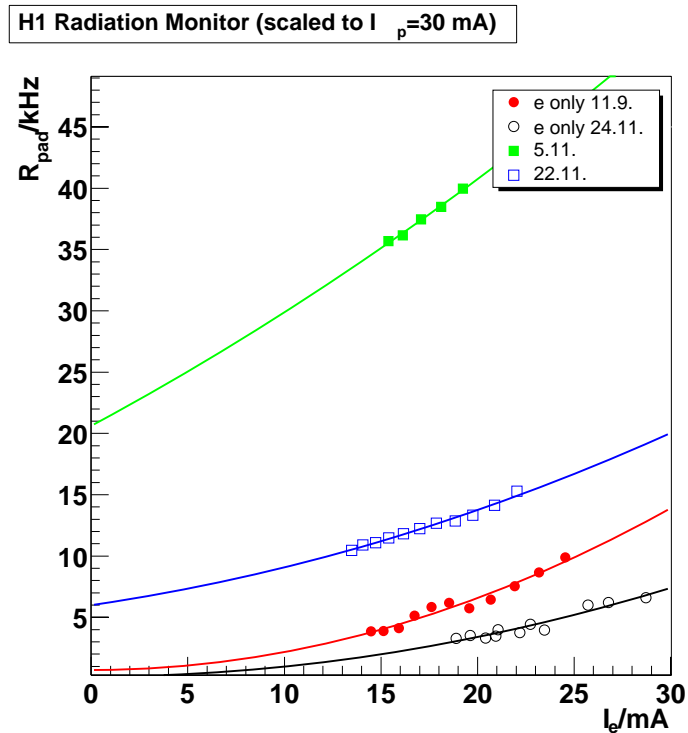

Figure 4.5: Dependance of Radiation Monitor rate on I_e at constant $I_p = 30$ mA for a few sample runs in 2002. From 4.11.2002 a different ϕ sector was used, so rates are not comparable in magnitude

Different contributions appear to change over time which can be attributed to different vacuum conditions. Unfortunately radiation destroyed the readout electronics in some of the ϕ sectors which led to changes in the setup. The long term analysis would consequently not be conclusive. Instead it is performed using the CJC.

4.2.2   Central Jet Chamber as Background Monitor

The CJC is the most important tracking detector of H1. It is divided into inner (CJC1) and outer (CJC2) part. They have 720 and 1920 sense wires made of gold-plated tungsten with a diameter of 20 μm. After a certain

amount of charge collected on the sense wires, ageing effects reduce the efficiency considerably and the wires have to be replaced. From operation experience of former years it was judged, that $I_{CJC} \leq 200\,\mu A$ is a tolerable limit for the highest luminosities.

Being one of the most important and sensitive subsystems, the CJC also became the most important background monitor as soon as it was switched on. In the final phase of beam steering HERA used the CJC current to optimize background conditions.

The analysis described above is done using the more stable CJC2 current. The result of the fits for a few sample runs are given in figure 4.6. The pedestal is determined to be $a_0 = 15\,\mu A$. For the positron run in November synchrotron and positron gas contributions are both present with $a_1 = 1.2\,\mu A/mA$ and $a_2 = 0.028\,\mu A/mA^2$. The proton induced part is seen to change over time.
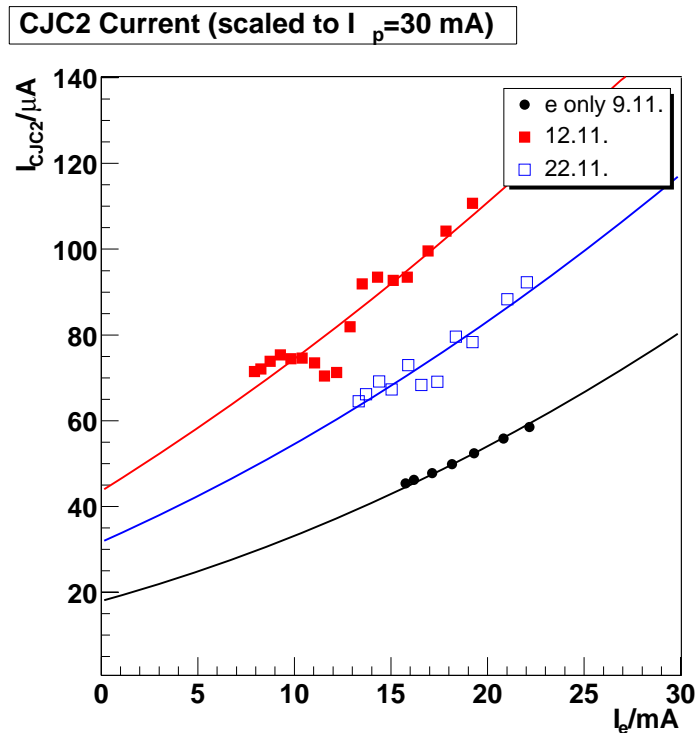

Figure 4.6: Dependance of average CJC2 current on I_e at constant $I_p = 30$ mA for a few sample runs in 2002.

4.3   Correlation of the Background Monitors

Even though absolute values of the H1 Radiation Monitor are not comparable over longer timescales, it is still a very useful tool. During injection and luminosity tuning it provides the only reasonable source of background information. In this phase backgrounds are very high and the high voltage of the gas chambers is switched off until the Radiation Monitor shows stable conditions.

The correlation to the CJC currents has to be considered for each of the different setups separately. The dependence changes if only a positron or a proton beam is present. A linear fit $R_{RM} = R_0 + c \cdot I_{CJC2}$ describes the data well, compare figure 4.7. The exception are the positron only runs, where there is a deviation from the linear correlation due to the fact, that the Radiation Monitor rate is mostly quadratic in I_e, but the CJC2 current contains a linear synchrotron contribution.

	September/October 2002	November 2002
e only	0.29	0.10
p only	0.60	—
ep	0.38	0.19

Table 4.1: Coefficient $c \cdot \mu$A/kHz relating the Radiation Monitor and the CJC according to $R_{RM} = R_0 + c \cdot I_{CJC2}$. All fits extrapolate to a CJC pedestal of about $I_0 \approx 15\,\mu$A for $R_{RM} = 0$.

Table 4.1 summarizes the different slopes of "p only", "ep", and "e only" correlations. These indicate the Radiation Monitor to be more sensitive to proton beam induced and less sensitive to positron beam induced background compared to the CJC. This is very reasonable: on the one hand synchrotron radiation does not contribute significantly to the Radiation Monitor rate, on the other hand the BSTT is located closer to the source of background induced by the proton beam in the backward region of H1.

4.4   Time development of the background

The next step is to use the fit procedure for various runs within a longer time period. In September 2002 conditions had stabilized. Data is analyzed from then until the shutdown in February 2003. The typical maximum beam currents in that time were $I_p \approx 40$ mA and $I_e \approx 30$ mA. For these values, the five different contributions of the CJC current are shown in figure 4.8 as a function of time. The most variable contributions are the proton induced
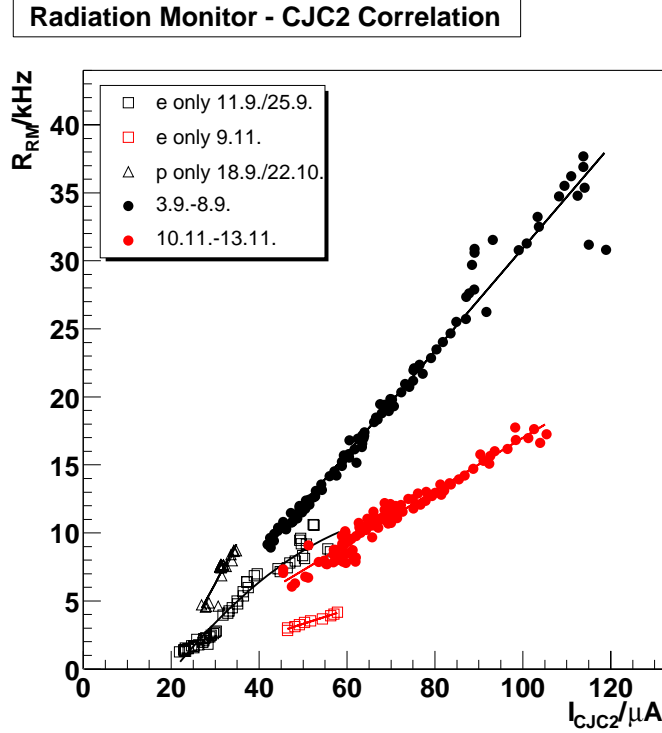
Figure 4.7: Correlation between H1 Radiation Monitor rate and CJC2 current. The Radiation Monitor setup changed on 4.11.2002. The relation is mostly linear, but depends strongly on the beam setup used. For "e only" runs, the different physical processes responsible for R_{RM} and I_{CJC2} are visible.

background components. Various "e only" runs reproduced similar values for the direct positron beam induced background (a_0, a_1). Beam steering and collimator settings are the major influences for this contribution.

Towards the end of the year 2002 a strong improvement is seen, mostly because the dynamic pressure increase became less severe. This is a consequence of continuing "bake out": gas trapped in the beam pipe is freed during running and slowly pumped away. For the best conditions, the proton induced contribution drops below the direct positron contributions, but typically both parts are similar in magnitude.

At the beginning of 2003 a vacuum leak worsened conditions for some time. However the situation improved quickly, especially the high base pressure part was reduced within 2 weeks.

As a cross check for the reliability of these results, the coefficients that should exhibit a proportional behavior to the effective mean pressures $\langle P_L \rangle$
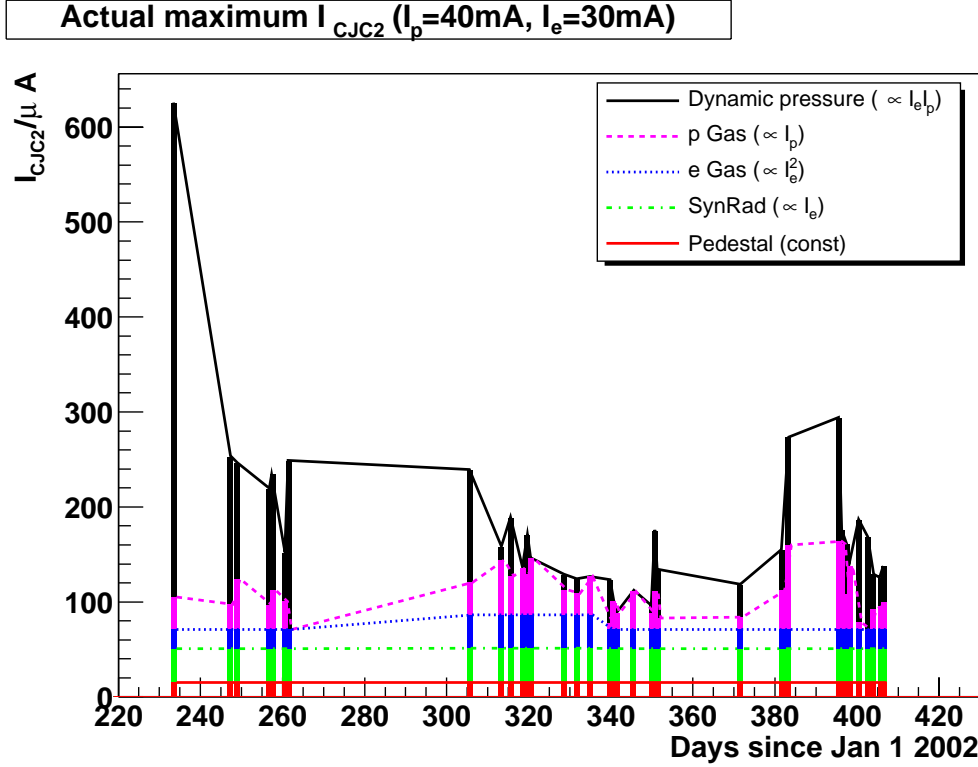
Figure 4.8: Actual CJC2 current scaled to typical currents of $I_e = 30$ mA and $I_p = 40$ mA. At the beginning of the year 2003 (day 380) there was a vacuum leak.

and $\langle P_R \rangle$ can be correlated with measured beam pipe pressures. There are several ion getter pumps located close to the interaction point at positive z (region sensitive to positron–gas interactions, called NL for "North Left") and at negative z (region sensitive to proton–gas interactions, called NR for "North Right"). These display pressure as given by the ionization current within a range of about 10^{-6} mBar to 10^{-10} mBar. The NL pumps are typically at or close to the pedestal value, but the NR pump pressures vary quite strongly as was shown in figure 4.4. The vacuum is worst close to the interaction region and improving strongly in both directions. Studies indicated, that due to the existing vacuum conditions and H1 acceptance for background, the pressure down to $z \sim -10$ m is most important for the proton induced contribution [24]. One has to keep in mind, that:

- pump locations are local minima in the pressure profile,

- the relation between pump current and vacuum is actually not well

known and also depends on gas composition.

As an example the pumps NR3.6 and NR8.3 are chosen, located at $z = -3.6$ m and $z = -8.3$ m, respectively. Other NR pumps show either similar behavior or are too close to their pedestal values to be of use. According to the model equation (4.2) the base pressure measured at $I_e = 0$ is expected to correlate with the parameter a_3. The dynamic pressure increase divided by positron current $\Delta p/\Delta I_e$ at the start of a run should be proportional to parameter a_4. Results are shown in figure 4.9. Error bars reflect only the statistical uncertainties. The total uncertainty can be judged from the spread of points for similar conditions.

The a_3 parameter varies strongly, while exhibiting a slow falling tendency in time. Only the base pressures measured with NR3.6 are well above the pedestal value. While some correlation can be seen for the highest pressure values, it is overall not very strong. Typical values are $a_3 \sim 0.5 .. 1.0 \, \mu A/mA$, but for pressures above the average values of $a_3 \sim 1.3 .. 2.5 \, \mu A/mA$ are reached.

The behavior of a_4 is consistent with the measured fall of $\Delta p/\Delta I_e$ in 2002. A simultaneously rise and fall is observed due to the vacuum leak in January 2003. The correlation plot for one pump shows the expected behavior, though there are quite a few point off the overall trend. However as $\Delta p/\Delta I_e \to 0$, one cannot expect the measured pressure values to be an accurate representation of the effective pressure $\langle P_R \rangle$ any more because of the limited dynamic range of the pumps.

In summary the model (4.2) represents reality reasonably well, despite some fluctuations. Uncertainties can be estimated by averaging over the runs of a few days with similar conditions.

4.5 Extrapolation to Design Currents

The last step is to extrapolate the measured backgrounds to HERA II design currents of $I_e = 58$ mA and $I_p = 135$ mA. This is done in figure 4.10.

At higher beam currents, background will be dominated by the proton induced contribution. For bad vacuum conditions CJC currents of over 1 mA are reached, far above the acceptable limit of $I_{CJC2} \leq 200 \, \mu A$. However in time this excess factor of more than 5 is reduced to about 2 to 3. The dominating contribution is the dynamic pressure increase $\propto I_e I_p \propto \mathcal{L}$ directly limiting luminosity. Fortunately this part also showed the strongest improvement over time due to bake out.

Other studies like MC simulation and worsening the vacuum intentionally
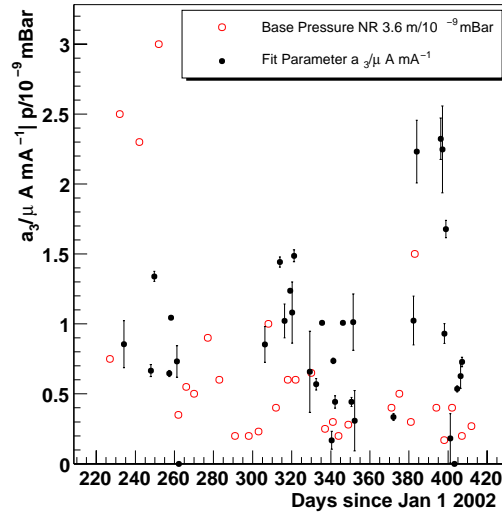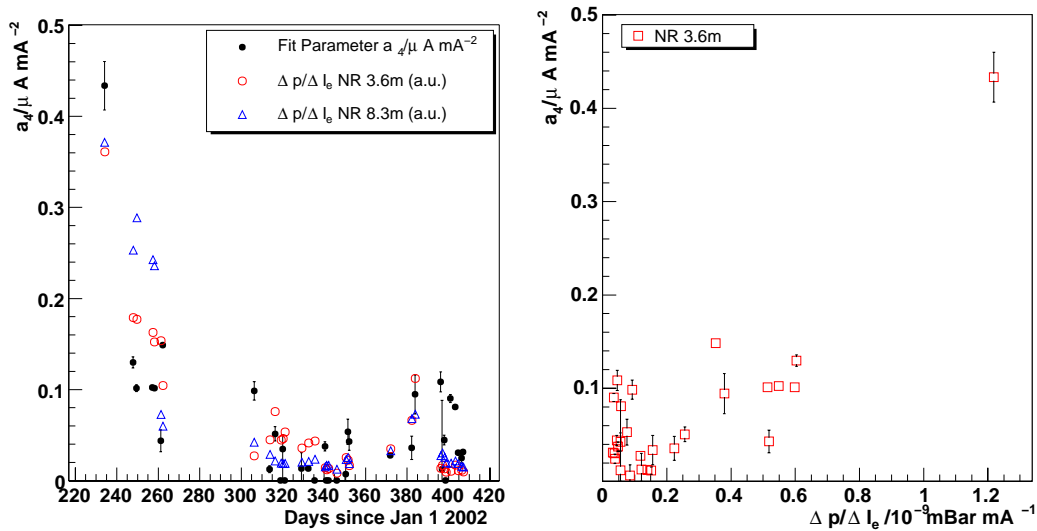
(a) Time development of parameter a_3 and base pressure at NR3.6.

(b) Time development of parameter a_4 and dynamic pressure increase $\Delta p/\Delta I_e$ (arbitrary normalization).

(c) Correlation a_4 to $\Delta p/\Delta I_e$ at NR3.6. Lowest pressure readings are unreliable.

Figure 4.9: The CJC fit parameters a_3 and a_4 and respective pressure values. A linear relation is expected in each case. Errors are statistical from fit only. Most prominent features are the improvement in 2002 and the vacuum leak at day 380.
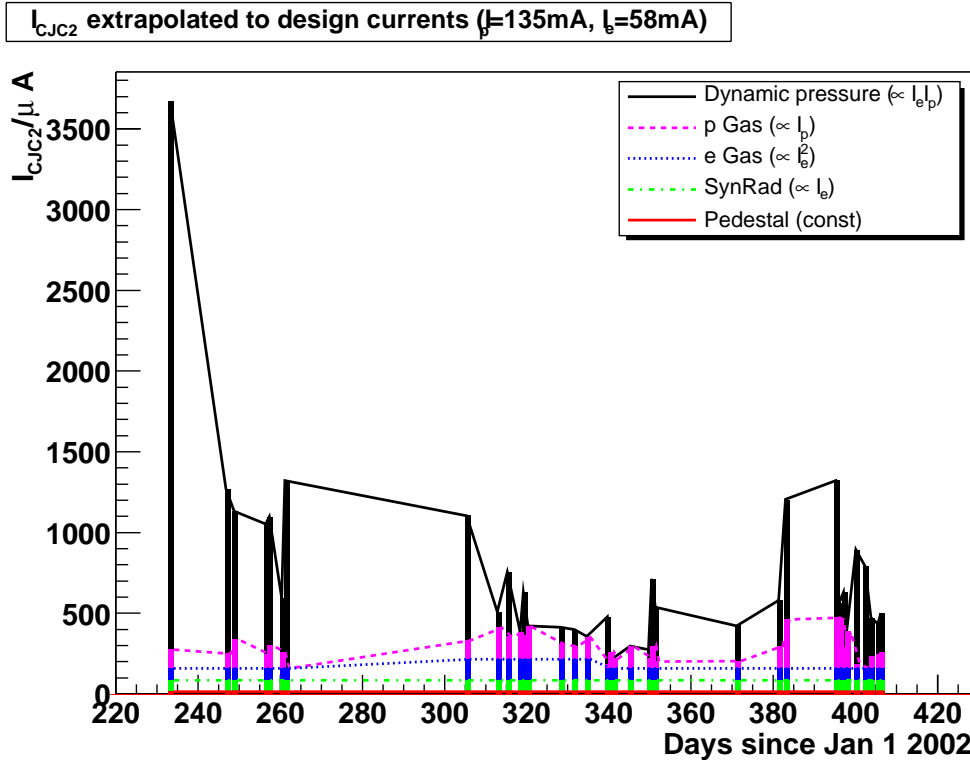
Figure 4.10: CJC2 current scaled to HERA II design currents. Safe operation limit is considered to be about $I_{CJC2} \leq 200 \, \mu A$.

confirm the dominance of proton induced background and also stress the importance to improve the vacuum in "North Right" [23, 24]. Some measures were taken in the 2003 shutdown to improve the situation:

- Absorber coatings were optimized to lower synchrotron backscattering into the detector.

- The collimator C5B which causes rescattering and thereby increases charge multiplicity and disturbs physics data taking (as shown in figure 4.2), was reduced in thickness from 2 cm to 0.5 cm. The new design still reduces the flux of synchrotron radiation as needed while the nuclear interaction length is reduced as much as possible. Heating by excitation of higher order modes is minimized by optimizing the shape of the collimator. Additional cooling for C5B was installed to avoid high dynamic pressure increase.

- An additional pump was installed in the sensitive NR region at $z = -1.5$ and the performance of the NR3.6 pump was raised.

In the first few months after the 2003 shutdown HERA operation has been repeatedly interrupted by technical problems and vacuum leaks. However first operation with $I_e \times I_p \approx 20 \times 60$ mA^2 at low CJC2 currents of about $I_{CJC2} \sim 120\,\mu$A looked encouraging.

Chapter 5

Analysis of first BSTT Data

In the HERA II upgrade the BSTT was extensively modified. Before operation experience could be gained however, parts of the repeater board were rendered non-functional by radiation damage. When the situation had stabilized in the end of 2002, tests were possible with 1 out of 6 double sectors. At this time it was especially interesting to check, if the detector modules were still working reliably.

The test was repeated with the first available data after the 2003 shutdown. During the repairs the setup was changed to make the repeater electronics more radiation hard (see chapter 6). This was the first test in H1 operating conditions.

The available bandwidth of the BSTT is just 8 bit per sector and bunch crossing and thus very limited, as it was designed as trigger detector with built-in data reduction. Further standards in the H1 DAQ System prevent the system from transmitting information to the main data stream after the L1 trigger decision is made. Therefore a "raw data" mode, in which all front-end detector signals at the event time are stored for unbiased offline analysis is possible only with limitations. If the storage of 1 bit (hit/no hit) for each of the 8 rings per detector module is desired, data from a single plane can be taken for a given run. Efficiency can be monitored with respect to the signals from other detectors.

The analysis is carried out in the PAW/Fortran analysis chain of the H1 Working Group for "Inclusive Measurements" (nELAN [26]). From the data tapes HBOOK ntuples are created which store data used for analysis already including known corrections. For all events a Fortran function is executed which performs tasks like data selection and histogram booking and filling. Final analysis of the histogram data is done in the PAW framework [27].

5.1   Detectors used for Analysis

The most simple calculation of internal efficiency, where 3 planes show a track signature and this is to be confirmed by the 4th plane, cannot be performed due to above mentioned bandwidth restrictions.

The next most obvious detector to use for external efficiency analysis would be the BST Strip. It matches geometric acceptance perfectly and the detection is based on the same physical principle. Unfortunately this detector has not delivered reasonable data until now because of various different problems. The same can be said about the other track detector in the backward region, the BPC.

The only detector left to detect particles going into the backward direction is the SpaCal, which is consequently used. The position resolution of cluster reconstruction is very good with $\sigma_{\text{pos}} = 4.4\,\text{mm}/\sqrt{E/\text{GeV}} + 1.0\,\text{mm}$. Combined with the long lever arm, "track reconstruction" is good enough to resolve the single BSTT rings.

In addition vertex information is crucial. The z-vertices of ep events are distributed approximately Gaussian with a width of $\sigma = 120$ mm. Also the beams do not collide at $x = y = 0$ in the H1 coordinate system. Beam offsets are up to 10 mm and run dependent. Vertex information was delivered from reconstruction of the central trackers. Alignment of the detectors with respect to each other is also important. It was checked using QED Compton Events $ep \rightarrow ep\gamma$ with both e and γ detected in the SpaCal. Furthermore tracks reconstructed in the central trackers and in the backward detectors can be compared in θ and ϕ to verify alignment. Summarizing, alignment of the SpaCal to the central trackers is to be found better than the position uncertainties of the BST.

5.2   Event Selection

Data was collected during standard luminosity runs of HERA. Two samples are analyzed: January 2003 data and November 2003 data. With respect to the properties concerned in this analysis, both data sets are very similar. Therefore figures are usually given for one of them only except for the final efficiency result.

January data is available only for the first plane of one double sector. The November data was collected and analyzed for a similar setup. Because of electronics problems, the double sector just next to the one from January data is used.

Requirement of an event with a reconstructed vertex made the central track

triggers most important for data taking. Offline several additional cuts are applied. The z-vertex is required to be in the range $|z_v| < 30$ cm to reject background. Resolution of z coordinate should be $\Delta z_v < 4$ cm.
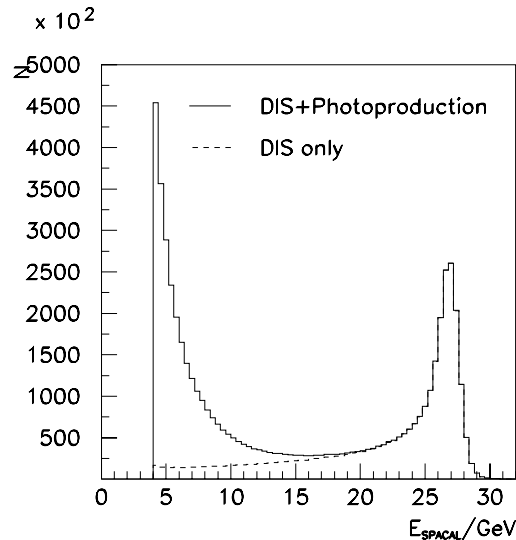

Figure 5.1: MC simulated energy spectrum of electromagnetic clusters in the SpaCal using DJANGO and PHOJET.

It is very important to suppress electromagnetic clusters created by hard photons, as they do not leave a signal in the silicon detectors. The expected energy spectrum can be simulated with the MC generators DJANGO [28] and PHOJET [29] for DIS and photoproduction events, respectively. Combining the two samples weighted by luminosities, the energy spectrum shown in figure 5.1 is obtained. The kinematic peak of DIS positrons near the nominal beam energy of $E_e = 27.6$ GeV is clearly visible. Clusters from photoproduction lead to a strong rate increase towards low energies. For $E_e > 15$ GeV the amount of contributing photoproduction is negligible. The number of photons is reduced further by the cut on the cluster radius $r_{cl} < 4$ cm and by requiring exactly one lepton cluster candidate.

Using the cluster coordinates in the SpaCal and the z-vertex information from the central tracker, the next step is to select only events where the positron is within the geometric acceptance of the BSTT sensors. In general, the track of a charged particle in a magnetic field is a helix. However a high momentum track with small angle with respect to the B-Field will curve only very little. A straight line extrapolation is used as first approximation. The

influence of the magnetic field of the H1 solenoid of about $B = 1.15$ T can be modeled as a shift in ϕ depending on z, θ, and particle momentum (sign reflects the charge of the lepton). The resulting shift $\Delta\phi$ in radians is

$$\Delta\phi = 0.29979 \frac{(B/\text{T})\,(z/\text{m})}{2\,(p/\text{GeV})\cos\theta} \;. \tag{5.1}$$

Limited resolution especially of the vertex reconstruction has to be taken into account as well. This is done on an event-by-event level. The acceptance is checked for the whole $x\sigma$ region around the reconstructed vertex. Here x represents an adjustable factor by which the coordinate uncertainties σ are multiplied. When x is raised, the number of selected events drops. Simultaneously the efficiency of the detector increases first and then stabilizes. The range $x = 1\ldots 6$ is investigated. The choice of $x = 2$ seems reasonable for cutting all events outside the BSTT acceptance and leaving most of the statistics.

Furthermore the exact positions of the active sensor areas are not known better than to a few 100 μm.[1] Therefore cuts around the sensor edges are applied. These are investigated in the same manner as described above. Finally radial cuts of $\delta r = 1$ mm and azimuthal angle cuts of $\delta\phi = 1°$ are used. Both data sets contain about 300 events after these cuts. In figure 5.2 the distributions of the cut variables are shown. The polar angle distribution of selected positrons is shown in figure 5.3.

5.3   Efficiency and Noise

For the available positron candidates the estimated radius in the BSTT detector r_{Spacal} is computed. If a hit in the corresponding pad module is found, its radius r_{Pad} is taken as the middle of the ring. The correlation of the two radii and their difference is shown in figure 5.4. A cut on the difference $\Delta r = |r_{Spacal} - r_{Pad}| < 1.5$ cm is applied to reject a few random noise hits. A very good correlation band is observed.

The width of the Δr distribution is determined by several factors:

- The coarse resolution of the rings with an average size $\overline{r_{Pad}} \sim 0.8$ cm leads to an uncertainty of about

$$\sigma_{\Delta r1} = \overline{r_{Pad}}/\sqrt{12} \sim 0.23\,\text{cm}\,. \tag{5.2}$$

---

[1]This will improve as soon as alignment is performed with the BST Strip system.
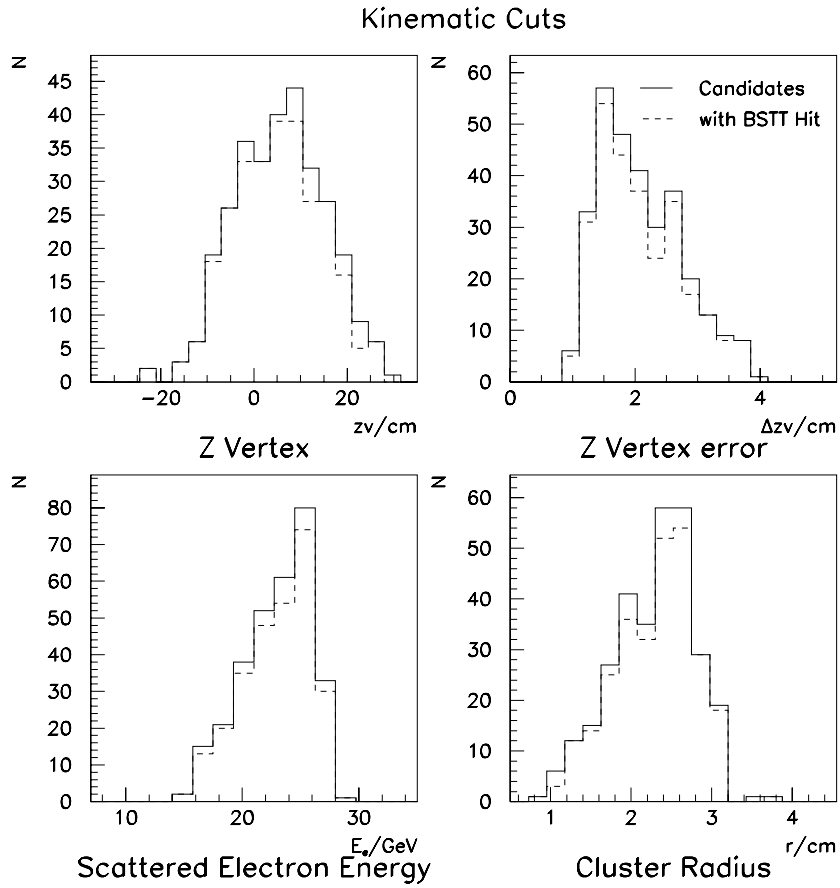
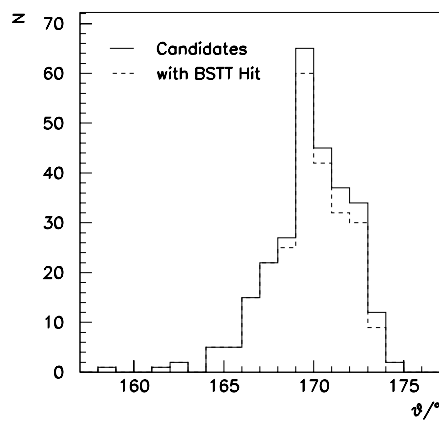Figure 5.2: Kinematic distributions after applying general kinematic and acceptance cuts (November data).

Figure 5.3: ϑ distribution of selected DIS positrons in the BSTT plane closest to the interaction point (November data).
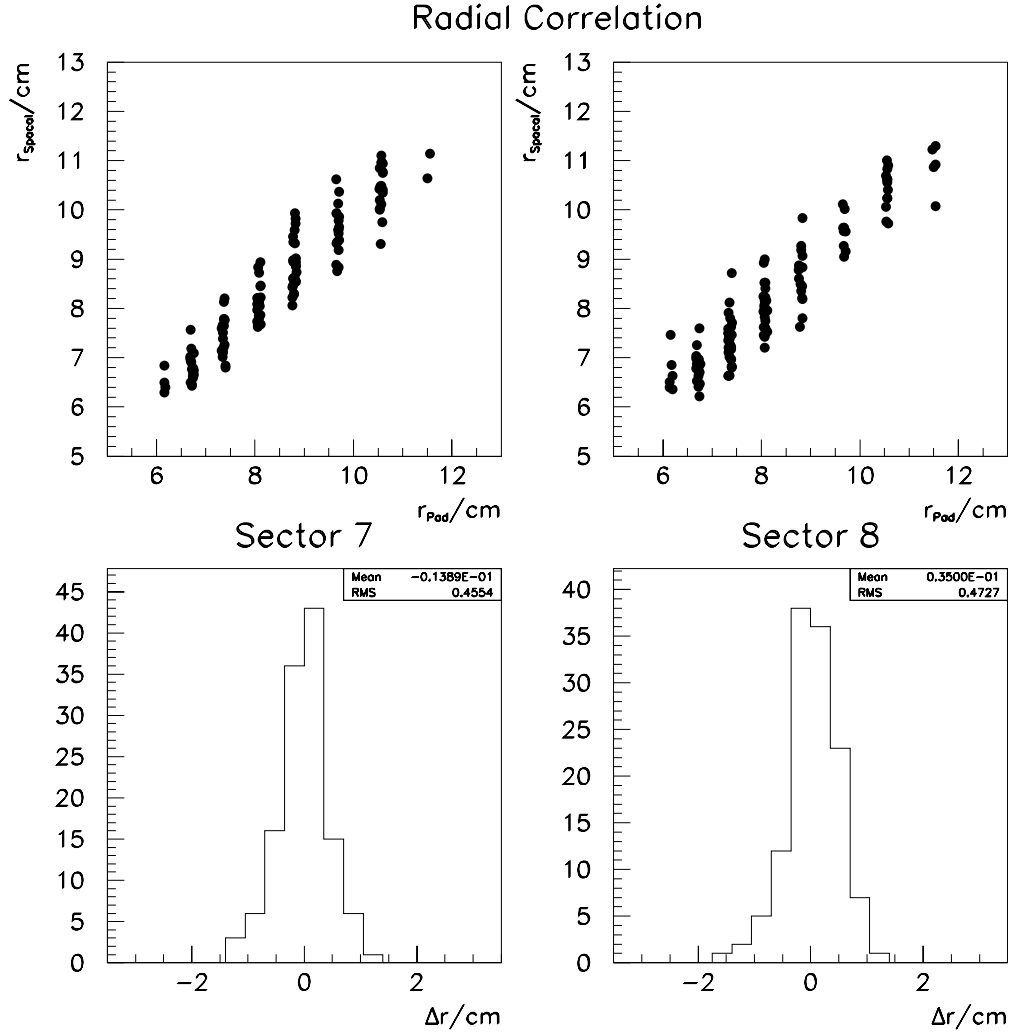
Figure 5.4: Radial correlation of hits in BST Pad sensors and hits expected from vertex and SpaCal cluster information (November data).

- Uncertainties of the primary vertex and the SpaCal cluster position measurement. The position resolution of the SpaCal in this energy range is about 2 mm, while the z-vertex uncertainty with typically $\Delta z_v \sim 2$ cm dominates.[2] This leads to $\sigma_{\Delta r2} \sim 0.23$ cm from error propagation.

- Unknown misalignments.

Adding the $\sigma_{\Delta ri}$ in quadrature, a minimal $\sigma_{\Delta r} \sim 0.33$ cm is expected from this

---

[2]No improved resolution from CST was available.

simple estimation. This is consistent with the measured $\sigma_{\Delta r} \sim 0.38 \ldots 0.45$ cm.

Finally efficiency can be calculated from the number of candidates in a given ring N and the number of found hits in this ring N_{hit} as

$$\epsilon = \frac{N_{Hit}}{N}, \qquad \Delta\epsilon = \sqrt{\frac{\epsilon(1-\epsilon)}{N}}. \qquad (5.3)$$

The statistical error $\Delta\epsilon$ is computed using a binomial distribution. It is a good estimate except for the cases were $\epsilon = 0$ or 1. Results for each individual ring are given in figure 5.5. Three of the four modules have average efficiencies in the range $\epsilon = (89.9 \pm 2.6)\,\%$ to $\epsilon = (95.7 \pm 1.6)\,\%$. The remaining module has an inefficient ring and therefore an overall worse result. If all detector modules work similarly, this is no reason for concern, only some redundancy is lost. This single detector efficiency is comparable to the test beam results, hence the detector modules are still in good shape after radiation exposure and the new repeater board is operating as expected.

The above quoted uncertainty is statistical only. There are also systematical uncertainties to consider:

- The sample might contain neutral particles that cannot be detected by a silicon detector but by the SpaCal. As discussed above, the energy cut ensures a very clean sample of DIS positrons. This is further supported by the efficiency dependence on the energy cut as shown below in figure 5.7.

- Limited resolution can result in accepting candidates, which are in fact outside the geometrical acceptance of the BSTT. This was checked by varying safety margins as described above and found not to be the case within the limits of statistical error,

- There might be noise hits in the detector leading to random coincidences. A test for noise makes use of the clean event signature in the backward region. In figure 5.6 the hits in the detector are counted for the case of a candidate missing the detector module at $\phi = 45°$ (2 sectors). Only 3.6% of the events had hits. All other three sectors have similar results. This is a direct upper limit for noise induced random coincidences which is estimated to be reduced by the cut on Δr to less than 2%.

Having summarized the sources of systematic errors it is concluded, that the total systematic error will be of the order of the statistical uncertainty. Further studies are not performed, since they are not necessary at this level of precision.
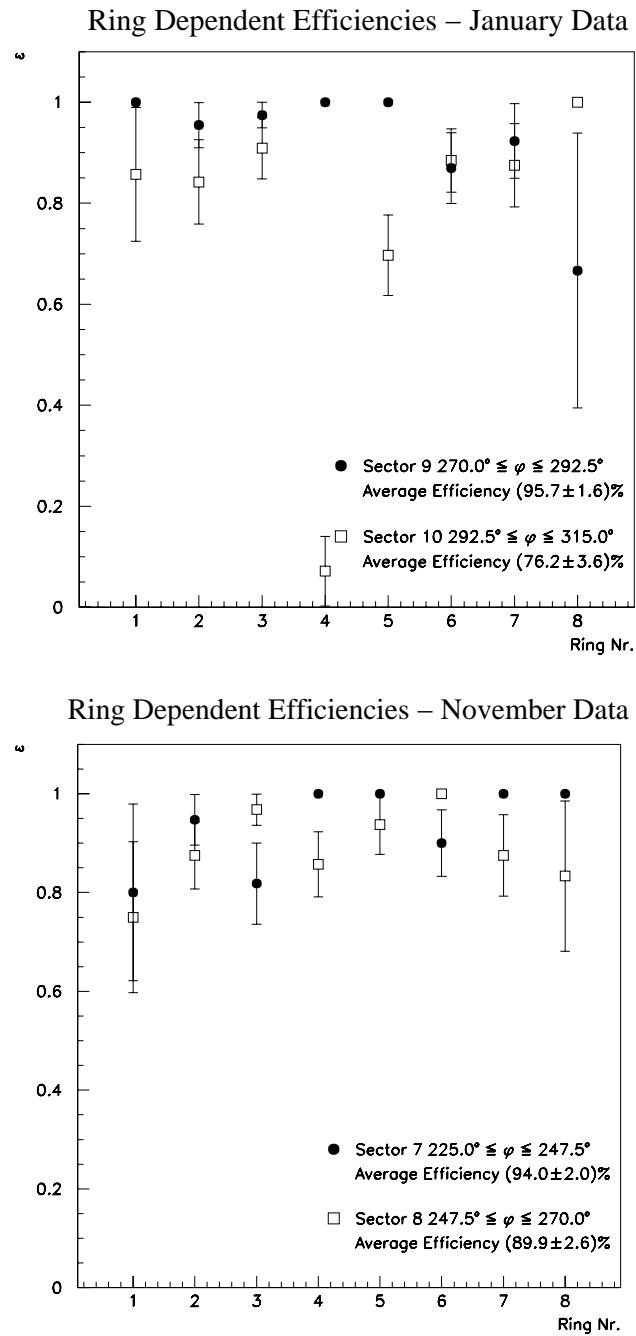
Figure 5.5: Efficiencies for each ring of 4 BST Pad modules. Data was collected in January (upper panel) and in November (lower panel). Except for the module with one inefficient ring (in sector 10,upper panel), the average efficiency is of the order 90% to 95% for all modules.
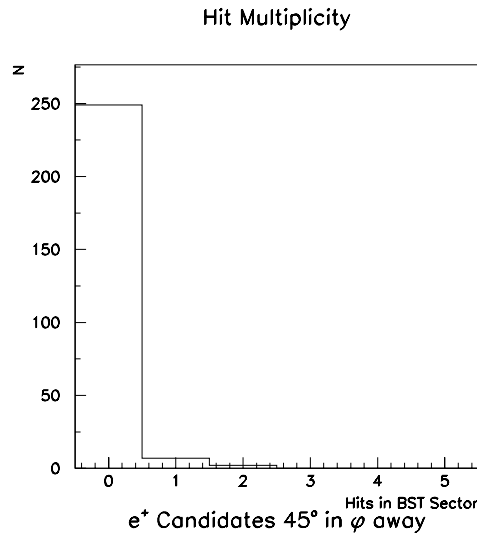
Figure 5.6: Hit Multiplicities for one sector with positron candidate not crossing the detector module.

5.4 Background Reduction

The primary task of the BSTT is to reduce photoproduction background by adding a track trigger to the SpaCal electromagnetic cluster trigger. As mentioned above, this is especially important for controlling the photoproduction background at low the energy thresholds of the SpaCal triggers for F_L measurements. A preliminary investigation was done with the January data. Keeping all other mentioned cuts, the overall efficiency was plotted for all energy bins down to $E_e = 2$ GeV, see figure 5.7. One sees again the rise of the photoproduction background towards lower energy and the kinematic peak of DIS positrons. As expected, the requirement of a BSTT signal removes a large part of the background. Even though other cuts suppress photoproduction in this data sample, the dropping efficiency for $E_e < 15$ GeV has to be attributed to the neutral particle background.

A secondary task of the BSTT is to generally suppress background events. As was discussed in chapter 4, high multiplicity events caused by scattered protons, e. g. in the collimator C5B, are a major source of H1 background. On the other hand DIS events have in most cases only one or two tracks in this detector region [18]. A simple cut on the hit multiplicity removes background efficiently. More investigation and simulation is needed here. A preliminary test of the effect of the trigger element TE195, defined as a veto for more than 5 hits per double sector, is shown in figure 5.8. A reconstructed vertex was
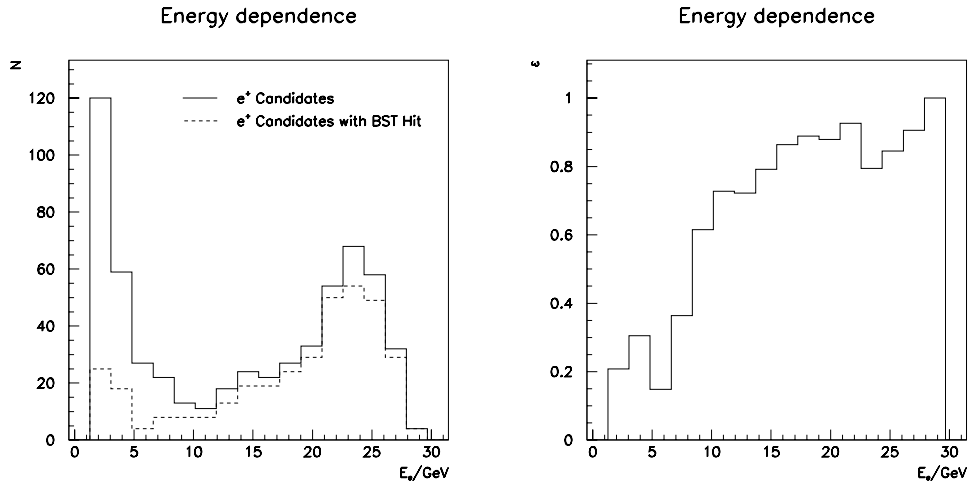
Figure 5.7: Suppression of neutral background at low energies with the help of the BSTT. The efficiency is stable within statistical variation down to $E_e \sim 15$ GeV.

required. The distribution of event vertices with the high multiplicity flag follows the background shape. The amount of background in this sample can be reduced by about 10% without vetoing real ep events from the primary vertex.
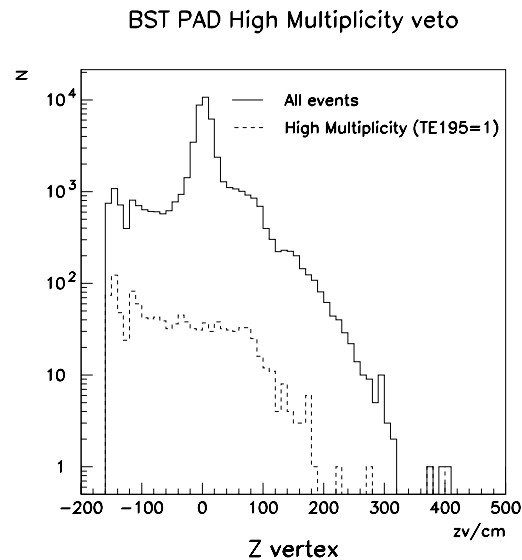

Figure 5.8: Suppression of background by high multiplicity veto TE195 of the BSTT.

Chapter 6

Upgrade and Repair of the BST

During the 2003 shutdown of HERA several problems in the BST had to be solved:

- Already planned for a longer time was the exchange of old r-strip detectors by the superior φ-strip type. As shown before, they proved to operate very well in the FST and a significant improvement in data quality is expected. More than 100 new modules were delivered months before the shutdown and evaluated in several standard tests.

- During operation it became evident, that some of the components of the Strip and Pad repeaters were not sufficiently radiation hard. This included vital components like the line drivers, that are responsible for transmitting the signals over copper cables outside the detector. Also the Slow Control interface was not working for several sectors.

- Additional damage on the detector modules themselves was expected. This had to be checked by applying the same tests like for new modules.

6.1   Radiation Damage of the BST

In order to be detected, particles have to deposit energy in the detector. However if this energy deposition is too high, the detectors can eventually be destroyed by radiation damage. Silicon detectors are especially problematic, because they are placed closest to the beams and need readout electronics very close to the detector. Both, detectors and electronics are made up of silicon primarily. Absorbed radiation energy per mass is measured in the SI unit Gray, 1 Gy = 1 J/kg; another unit often used is 1 rad = 0.01 Gy. Radiation can have different consequences for semiconductor devices[30]:

Total Ionizing Dose effects lead to trapped charges in the oxide insulator and can increase leakage currents. Modern sub-micron technologies tend to be more resistant than older technologies because trapped charges can escape more easily by tunneling effects. Commercially available products can usually stand a total dose of the order 10 to 1000 Gy. This kind of radiation damage is dangerous for detector modules (larger dark currents and therefore higher noise) as well as for electronics (shifting thresholds and higher power consumption).

Displacement damage is caused by hadronic interaction that shifts atoms from their position in the lattice. The effects strongly depend on the type of electronic device. Optical devices are especially sensitive.

Single Event Effects are caused by individual interactions that deposit a large ionization charge in a device. This is only relevant for electronic circuits. In the least problematic case this results in bit flips in the memory. Consequences are corrupted data or malfunctioning programs. By reloading the code, normal function can be restored after such a "Single Event Upset".
In more problematic cases, the charge disturbs the function of the device in a way, that a large current flows between power supply and the ground, so that the chip is permanently damaged by this "Single Event Latchup". Due to the statistical nature of the effect, one has to avoid too sensitive components. Special manufacturing processes are insensitive to this kind of damage.

6.1.1 Online Monitoring

The only effects that can be monitored and are influenced directly by the beam conditions are the Total Ionizing Dose effects. Using the Radiation Monitor provided by the BSTT, H1 monitors the dose rate and total dose during running.

A simple calculation relates the number of particles N crossing the active detector area $A = 40\,\text{cm}^2$ to the dose $D = E/m$ deposited due to ionization loss:

$$
\begin{aligned}
D &= 1.7\,\text{MeV/g} \cdot 3N \cdot \frac{\text{cm}^2}{A} \\
&= 2.0 \cdot 10^{-11} \text{Gy}\, N \,. \quad\quad (6.1)
\end{aligned}
$$

For this calculation minimum ionizing particles (MIP) with their characteristic energy loss of about $1.7\,\text{MeV}\,\text{g}^{-1}\,\text{cm}^2$ [9] are assumed. Because the

threshold for counting a particle was higher than the MIP level, a factor of 3 has to be included.

It is estimated, that the BST can stand a total dose of about 100 Gy for a operation period of several years. This limit is set mainly by the readout chip APC, whose performance deteriorates after an accumulated dose of 1 kGy [10]. Assuming one operation year to be 10^7 s, an upper rate limit of 500 kHz is obtained from (6.1). However a large part of the spectrum, namely softer photons, is not observed with the Radiation Monitor. Also higher doses might be deposited by a shower contained in one pad for example. Therefore a safety factor of 10 is applied and the limit is set to 50 kHz. Higher rates are tolerated only for a limited time. If HERA is not successful in optimizing conditions during this time, a beam dump is requested.

Figure 6.1 shows the integrated rate from autumn 2002 to the shutdown in 2003. Normal running periods have averaged rates of 10 kHz to 20 kHz, obeying the rate limit. Discontinuities are caused either by Single Event Upsets which enforced a reset and reload of the chips or by radiation accidents and subsequent electronics failure.
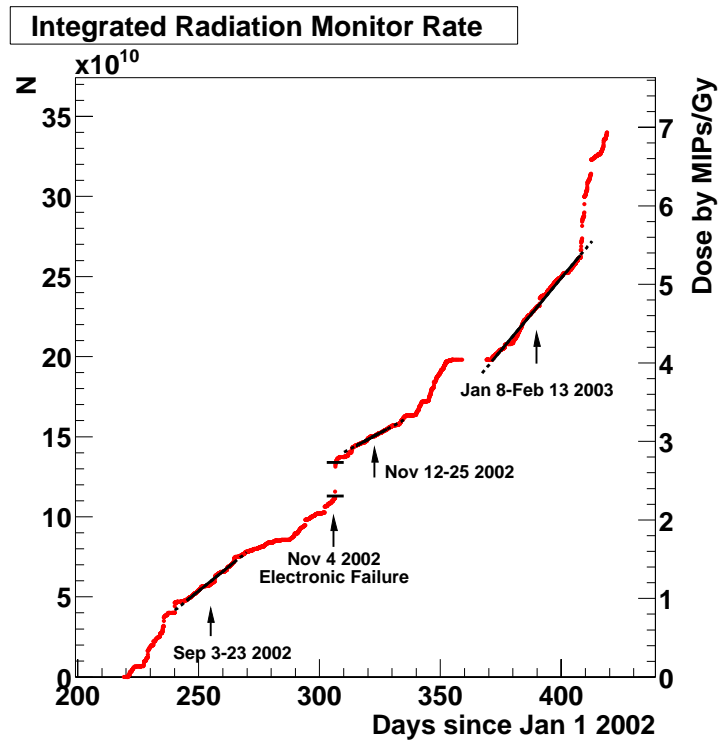

Figure 6.1: Integrated BST Radiation Monitor rate and MIPSs dose calculated according to equation (6.1).

The total dose calculated using equation (6.1) for the time period considered here is about 7 Gy. Even when multiplying with the safety factor of 10, the limit of 100 Gy per year of operation is not exceeded. However operation experience showed, that radiation damage was serious and much larger than indicated by this calculation.

6.1.2   Dosimeter Measurements

Whenever access to the detectors is possible, the integrated radiation dose can be determined more reliably using small dosimeters that are fastened to different positions of the silicon detector support structures. The type used is a "Radio-photo-luminescence (RPL) Glass Dosimeter" which consists of silver phosphate glass (4% silver content). Results for the FST for 2002/3 running were in the range of 50 Gy to 100 Gy. This is on the one hand consistent with the Radiation Monitor measurements. It shows on the other hand, that the used components can stand this dose, since the FST was operating very well throughout this period.

For the running periods before the year 2000, typical doses in the BST were of the order 10 Gy to 100 Gy per year in the detector volume close to the interaction vertex and much less in the repeater region.

For the 2002/2003 running period, the values are shown in figure 6.2. Some confusion was caused by the evaluation of the DESY D3 group responsible for radiation control. Because of the unexpectedly high dose, DESY D3 had to renormalize the initially "measured" values. Assuming these "corrected" values to be valid, one sees large differences. The detector volume received doses from only a few Gray up to 3.2 kGy in some areas. Averaging over this range, this is about compatible with the measurement of the H1 Radiation Monitor. In the rear section a dramatically higher exposure of the order 10 kGy was recorded. This is by far more than the design limit.

6.1.3   Radiation Effect on the Repeater Boards

Two types of chips proved to be mainly responsible for the malfunctions observed:

- Differential line drivers (Texas Instruments, transmitter AM26LV31 and receiver AM26LV32) used for the signal transmission over the copper cables: replacement chips HS-26CLV31RH and HS-26CLV32RH [22] manufactured in a radiation hard CMOS process are used for the repair (not qualified "PROTO" chips are used, however properties are supposed to be the same). These chips are function and pin compatible,
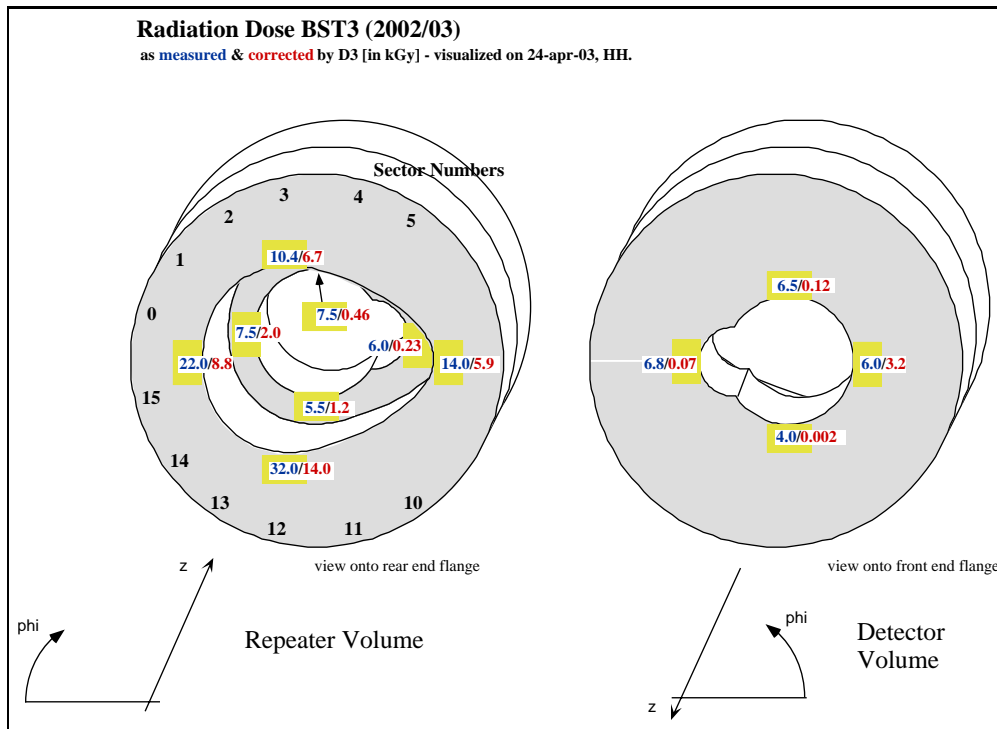
Figure 6.2: Dose "measured"/"corrected" in different parts of the BST. One sees a drastic increase in the repeater region. Explanation for the corrected values is given in the text.

radiation hard up to a total dose of 3 kGy, and immune to destructive Single Event Latchup.

- The SLIO chip (Philips P82C150, CAN Serial Linked I/O device) which represents the Slow Control interface: this is a rather old chip and is therefore more suseptible to the total ionization damage. For the Strip repeater these chips are used only for temperature measurements. For the Pad system however more advanced features have to be provided. A different chip with a new board layout is used, which is described in more detail in section 6.3.

6.1.4 Radiation Effect on the Detector Modules

Damage to the detector modules can occur in two different places: the actual wafers and the readout chips on the hybrid. Serious damage in any of them renders the whole unit unusable.

Measuring the leakage currents of the modules is a good way to test the

wafers. Strong irradiation might increase the currents and by that increase noise. The test was done in the same way as for new modules, leakage currents are measured as function of the applied bias voltage V_B. Figure 6.3 shows a sample measurement for a pad module. Currents increased after irradiation, but the general characteristics remained unchanged. In summary radiation exposure equalized the sensors: good wafers with formerly very low leakage currents show now similar currents like formerly only "acceptable" wafers. There was no critical damage in any Pad or Strip sensor.

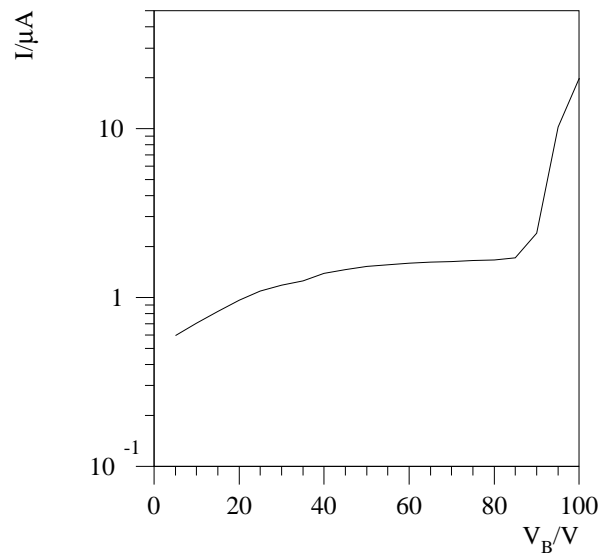**I/V Measurement of a PAD Module**

Figure 6.3: Total leakage current in a Pad Module. While this current is higher than before radiation exposure, the general characteristics remained unchanged. The behavior in the region of the depletion voltage ($V_B = 50$ V) is still stable.

The readout chips on the hybrid were another major concern. Tests indicated, that the Pad Hybrid ASICs were working well mostly. A few of them were exchanged. This is feasible, because only very few connections (32) exist between hybrid and wafer.
The readout chip on the strip hybrid is however more problematic. Bonding of the strips to the APCs can only be done once and single chips cannot be exchanged. The APC performance deteriorates if the total dose reaches about 1 kGy [10]. The functionality of this chip was described earlier. The damage analysis is done using a special sequence of test pulses that are injected into the 640 channels of one module. The critical part is the readout, which lasts

about 1 ms in H1 conditions, while the pipeline is rewritten every 3 μs during sampling. After the pipeline entries of a specified timeslice are transferred onto a latch capacitor, this preamplified signal charge has to be stable for the whole time of the readout. The latch capacitors of new APCs keep a stable signal for 5 to 10 ms.

In the test setup, the pedestal was subtracted and the signal was digitized using an oscilloscope. Already by optical judgment it was possible to identify bad modules, see figure 6.4.

Further data processing gave a quantitative measure of the APC damage. Three tests with artificially lengthened readout delays of 5, 3, and 1 ms are carried out. Modules passing the respective test are classified as "Quality=3" (5 ms) down to "Quality=1" (1 ms). Only very few bad channels should be tolerated in this laboratory test. Accordingly at least 97% working channels are required to pass a test. If modules are not stable even for 1 ms or have other failures, they are classified as "Quality=0" or "Quality= −1". This scheme is expected to have some correlation to the received dose, but detailed dependence is unknown. Figure 6.5 displays the status of all BST ϕ-strip hybrids before the repair. More than half of the 72 modules were damaged at least partially. A strong correlation to the z position of the module in the detector is seen. This is consistent with the dosimeter measurements: both methods show that irradiation was much higher in the backward parts of the BST.

6.1.5 Conclusions from the Irradiation Analysis

Before this analysis the electronics failures were attributed to singular accidents in the beam steering and subsequent Single Event Effects, because the dose measured with the well working H1 Radiation Monitor seemed to indicate a rather low total dose. Analysis of the long term history (figure 6.1) also showed about half of the dose to be due to relatively short spikes.

However the strong radiation damage in the backward part of the detector volume and the repeater section hinted to a continuous radiation source: synchrotron radiation. Problems with the absorber and collimator setup must have lead to backscattered synchrotron photons reaching this particular part of the H1 detector. It is much less efficiently detected by the silicon sensors and therefore is not well represented in the Radiation Monitor rate.

Using damaged sensors was considered not to be reasonable. Some spares were available, however the large number of 41 modules could not be replaced. The only solution was not to fit all available positions with new detectors. Due to mechanical constraints and simulations concerning accep-
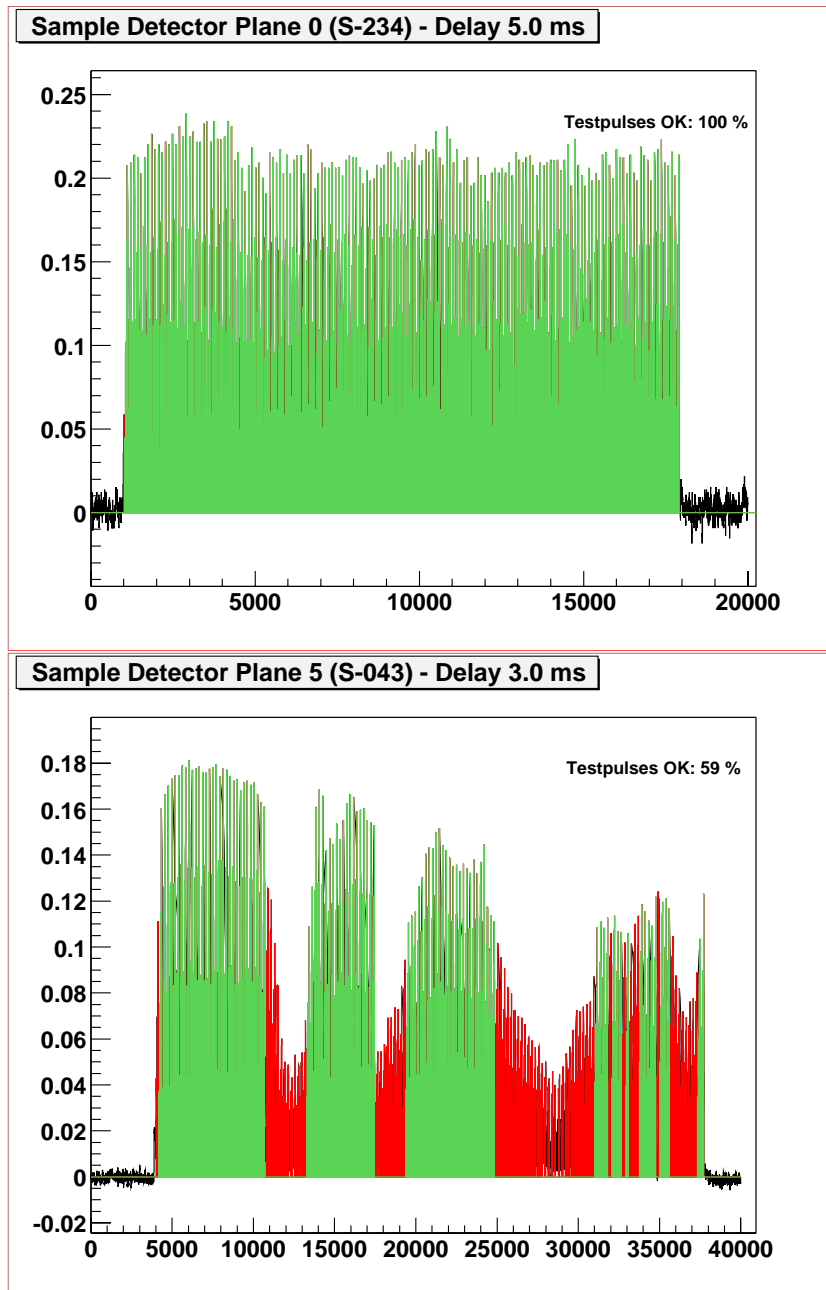
Figure 6.4: 640 APC test pulses from 2 different BST strip modules from the area of low (Plane 0, upper panel) and high (Plane 5, lower panel) irradiation. While the latch capacitors of the upper detector is long term stable, the lower one had many malfunctioning channels.
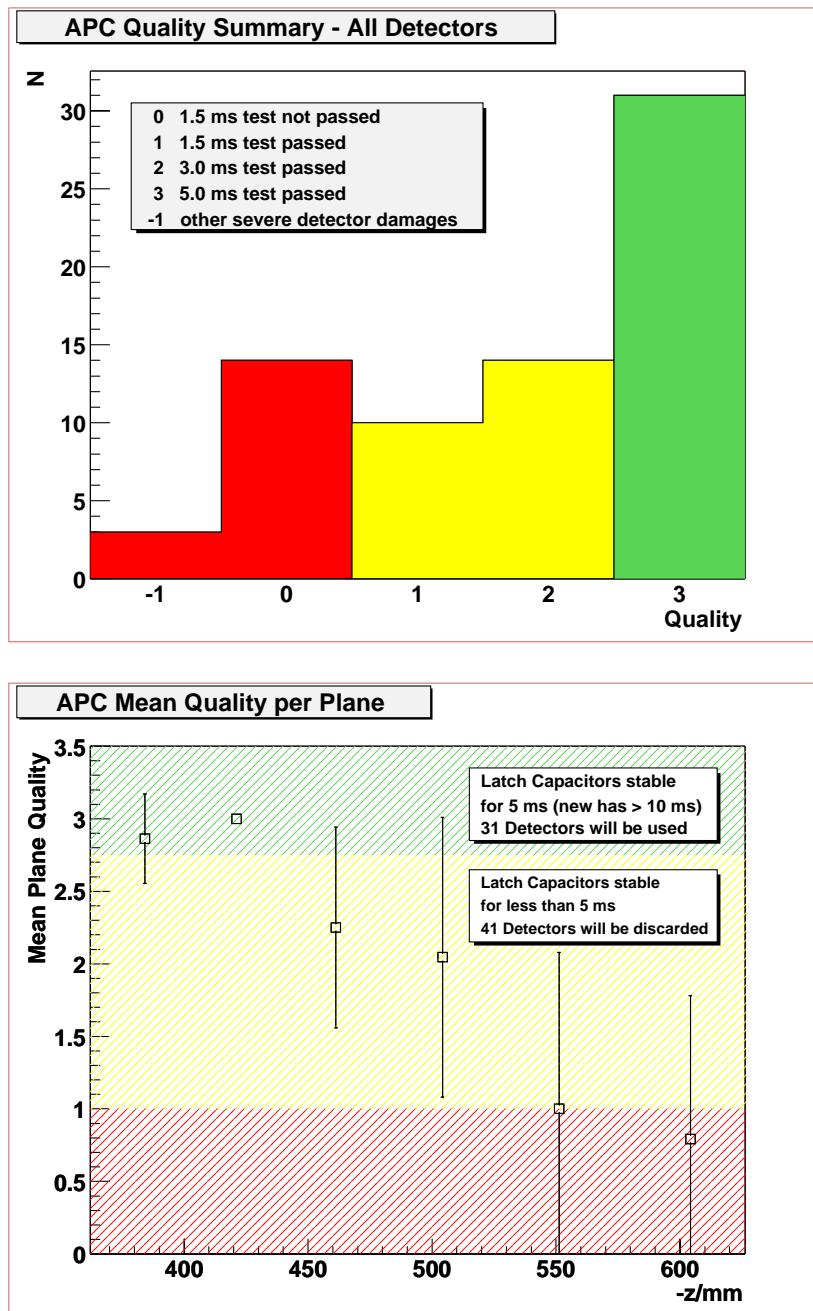
Figure 6.5: Overview over the functionality status of all ϕ-strip hybrids in the BST. Out of the 72 modules, only 31 are classified as "damage free". While there is no dependence on the azimuthal angle ϕ, there is an obvious correlation to the z position of the detectors. The bars in the lower graph represent the σ (r.m.s) of the quality class distribution, mechanical failures are excluded.

tance it was decided, to fit the intermediate plane 2 at $z = -461.2$ mm with slightly damaged sensors (quality class 2) from one side only. These modules should still work efficiently at the moment. If they become inefficient, some redundancy is lost.

The same kind of damage has to be avoided for the future. Even if the new repeater boards survive longer with the new radiation hard chips, the modules would soon become inefficient. Already before a lead shielding of about 2 mm thickness around the backward part of the beampipe was considered. Particles originating from interactions around $z = 0$ are not affected by this shield. The synchrotron radiation flux from the backward part of the experiment would be reduced by a factor of 50, but on the other hand the charge multiplicity of proton induced background increases through rescattering by about 20% [23]. Therefore the decision was staged until this analysis was completed. Having reliable knowledge about the source of radiation damage, the shielding is vital for the BST. Figure 6.6 shows the setup in the backward region with the new lead shield. It might help to improve the background situation as a whole, because other detector electronics is protected and the amount of synchrotron radiation reaching the CJC is reduced. First analysis of CJC data taken in a positron only run [31] after the shutdown confirmed this, see figure 6.7.

6.2   Strip Module Replacement

Various tests are carried out, before a single strip module is ready for assembly in the BST support structure.

The wafer may contain fabrication errors leading to high currents under depletion and therefore bad detection efficiencies. The electronics for the hybrid might also be faulty, especially the APC readout chips. Final checks have to be made to ensure proper operation of the whole setup, because once the detector is inside H1, access is not possible for a long time.

Wafers are typically tested in the depleted regime with the backplane put on the required potential. As visible light creates free charge carriers by photoelectric effect, all tests have to be done in light tight boxes.

6.2.1   Static Wafer Tests

Static tests are the first ones to be carried out to check for production faults that typically show up when a high bias voltage is applied. Modules not passing the static tests can be discarded instantly.

To determine the correct depletion voltage for every individual wafer, a mea-
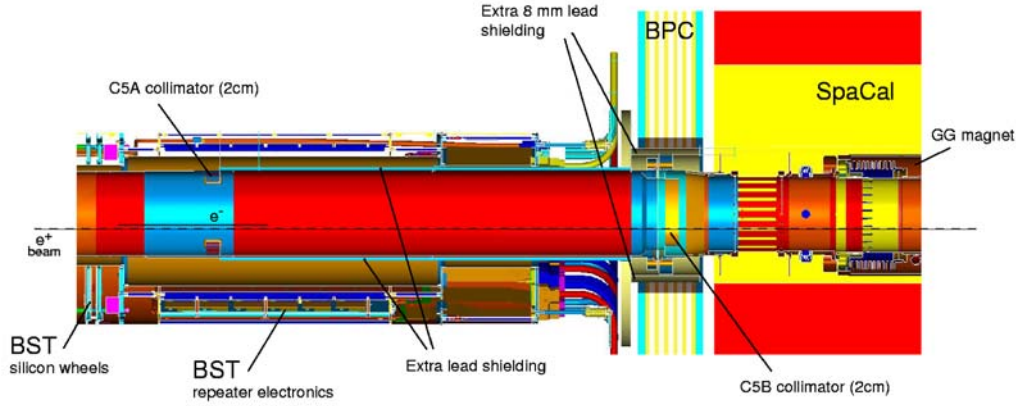
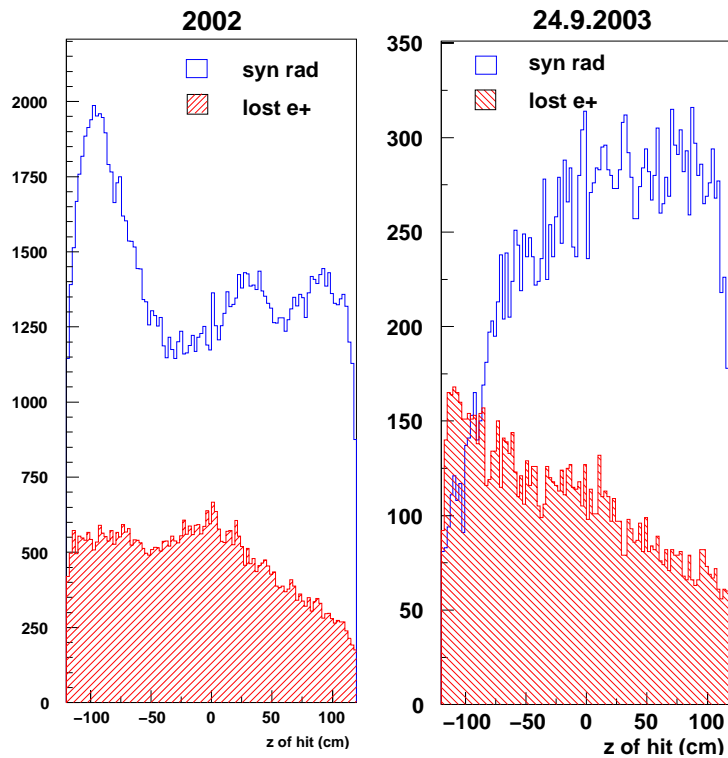Figure 6.6: The backward region of H1 with the new lead shield between $z = -80$ cm and $z = -150$ cm.

Figure 6.7: Hits in the CJC during e^+ only running. The data was triggered on an isolated bunch. Synchrotron radiation hits are distinguished from lost e^+ by hit multiplicity cuts. There is a pronounced difference for synchrotron radiation hits for $z < -50$ cm due to the new lead shielding. Figure is taken from [31].

surement of capacitance versus depletion voltage, short "C/V" measurement, is performed. A test structure on the wafer is used in order not to damage the module. A manual prober contacts the wafer. Instrument control and data acquisition are done with a LabView program running on a Macintosh computer. According to equation (3.2), voltage and capacitance are related as $C \propto V_B^{-1/2}$ as long as the detector is not fully depleted. Raising V_B more than needed for depletion will not change C any more. One method to determine the depletion voltage is to use a double logarithmic plot as demonstrated in figure 6.8. The observed relation in the non depleted regime is $C \propto V^{-0.45}$, close to the theoretical expectations. Typical depletion voltages for the φ-strip type are between 40 V and 75 V. Accuracy of a few Volts is sufficient in this test.

C/V Measurement of a Strip Module

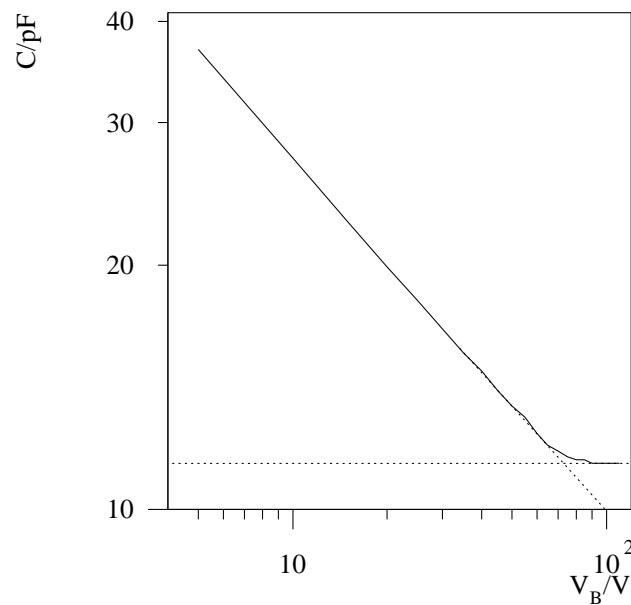Figure 6.8: Determination of the correct depletion voltage in a C/V measurement. The two regimes $C \propto V^{-1/2}$ and $C = $ const. are distinguishable. $V_B = 70$ V is sufficient for full depletion.

An important test of the overall quality of the module are measurements of guard and bias (active area) currents, I_G and I_B versus bias voltage V_B, short "I/V" measurements. The respective currents are measured through manual probers contacting the bias and guard structures. Typically there is a "break through" voltage after which currents rise rapidly. It is very important that this voltage is far above the depletion voltage. Good wafers

have stable currents of $I_G < 0.1\,\mu$A and $I_B < 2\,\mu$A even for $V_B = 300$ V. In the region of strongly rising currents one cannot expect an efficient detector with good S/N ratio. The results of two sample modules are shown in figure 6.9.
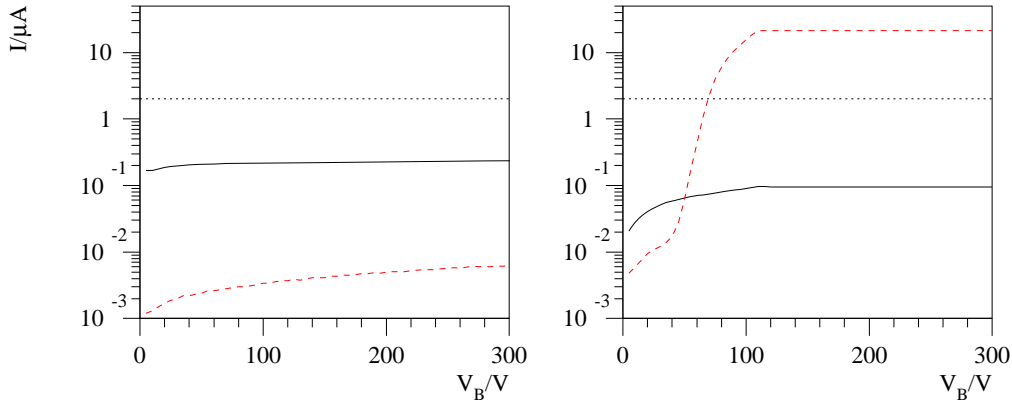
I/V Measurement of Strip Modules

Figure 6.9: Bias (solid lines) and Guard (dashed lines) currents as function of depletion voltage. The left measurement shows a very good detector with both currents well below the limit of 2 μA (dotted line), while the right one has very bad characteristics and has to be discarded. The current was limited to 20 μA.

Because the detector has to stay depleted for long periods during data taking and the lifetime of the whole detector should be several years, long term stability is important. Some production faults show up only after applying a high voltage for several days. So guard and bias currents of all modules are measured at 120% of the nominal depletion voltage for at least 1 week. Typical behaviors are shown in figure 6.10. After the long term test the I/V measurement is repeated.

Out of 113 delivered modules, 73 wafers showed very good results in the static tests, i. e. stable I/V behavior up to high bias voltages and no significant current increase during the long term test. To meet the increased demand for the replacement of damaged modules, another 16 modules were selected to be processed further. They had to pass relaxed selection criteria, for example break-through voltages of 150 V was still acceptable. While this is still well above the depletion level, it is a sign of production faults. As expected a large percentage of these worse performing modules showed dissatisfactory results in the following tests.
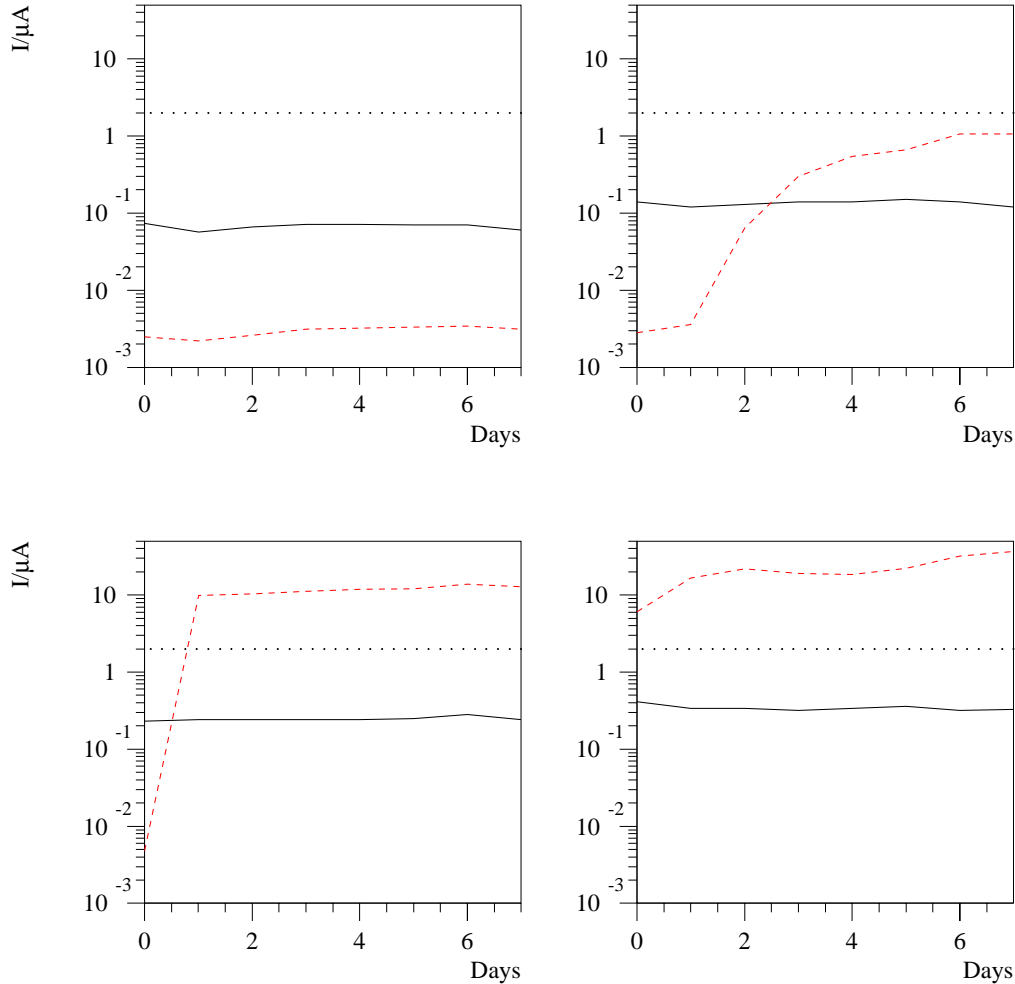
Long Term Measurement of Strip Modules

Figure 6.10: Bias (solid lines) and guard (dashed lines) currents in long term development. Both should stay within the limit of 2 μA (dotted lines). In the upper panels 2 modules passing the test with different characteristics are shown. The currents of the modules in the lower panels crossed the limit very quickly and are not usable.

6.2.2 Hybrid Tests

For testing newly assembled hybrids a procedure with test pulses very similar to the one used for diagnosing radiation damage is used. Noise, pedestal and the levels of test signals are recorded. This way problematic hybrids can be discarded before the final assembly. The test setup includes many

components used in H1. Control and evaluation of the test is done by a LabView program used for that purposes already in the BST upgrade in 2000 [17].

6.2.3 Final Assembly and Tests

A tested wafer can now be glued onto a tested hybrid. The module is sent to ZE at DESY Hamburg, where the 640 wire bonds from the strips to the APCs are done. After the bonding of the wafers to the readout chips the hybrid test is repeated.

As a final quality test, the efficiency of every strip is determined in a laser test. A pulsed laser (685 nm) shoots 10 times on each strip and the average signal is recorded. The laser mimics the effect of a particle crossing the detector. The only difference is that the charge carriers are created just below the surface of the detector by the light. The data analysis is similar to the one done online during H1 data acquisition. Pedestal, noise and hit efficiency are calculated. An automatic setup with a movable x-y-table tests a whole module in about 1 hour. Control and evaluation are done by a LabView program used for that purpose already in the BST upgrade in 2000 [17]. Figure 6.11 shows the output of the laser test for a typical module. The noise is rather low, efficiency 100% except for a few dead strips, and the signal amplitude is uniform for the whole module.

Altogether 80 new modules passed all tests with good results. Together with some old spares and the remaining undamaged modules it was possible, to equip 5 of the 6 planes with damage free detectors from both sides. As mentioned, the intermediate plane 2 is now equipped with slightly radiation damaged sensors from one side only.

6.3 The new BSTT Slow Control

One of the most interesting features of the BSTT is the possibility to change trigger settings online. For these functions a Slow Control system based on CAN bus communication was designed. On each motherboard the ALTERA ACEX is responsible for the Slow Control functions. It receives commands from the chip that serves as an interface to the CAN bus. In the old design a SLIO was used for both strip and Pad repeater. This chip however proved to be very sensitive to radiation damage.

The Strip repeater uses the CAN bus only for temperature measurements. This functionality can however be provided by the new Pad repeater, too. So the the destroyed line drivers were replaced by the new radiation hard type,
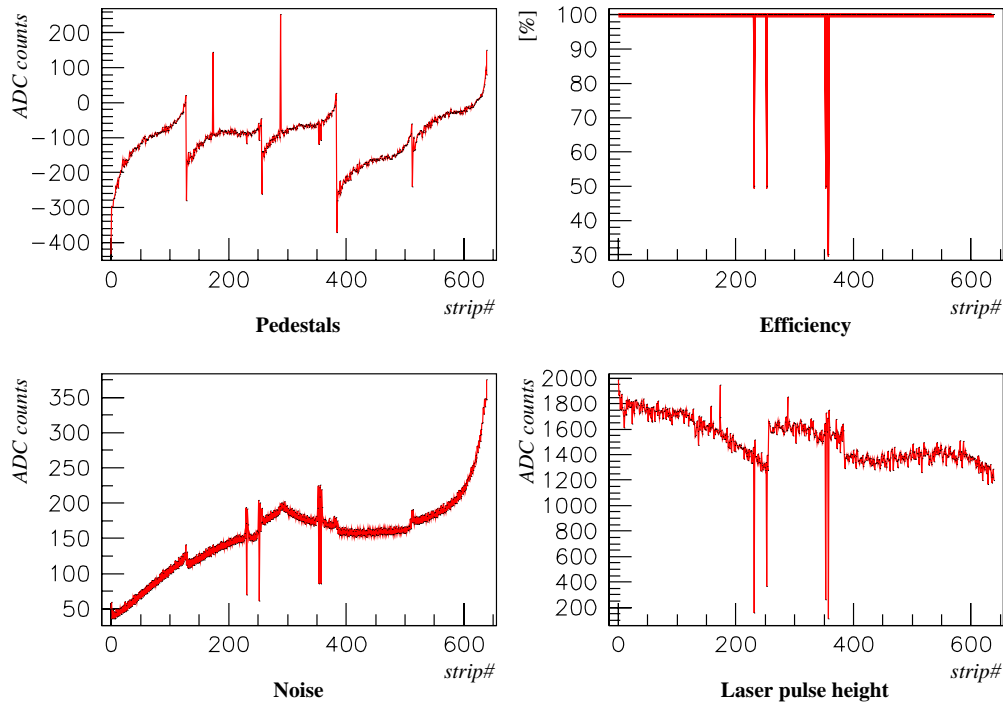
Figure 6.11: Laser test results for a good module. Rising noise to the end of the module is caused by the test setup and not seen in H1.

but the SLIO chips were merely exchanged as backup solution.

The PAD repeater was redesigned in many aspects. The exchange of the interface to the CAN bus by an ATMEL T89C51CC01 [21] has the largest impact. This controller includes the CAN interface and non volatile Flash memory for a user written firmware. The chip is less sensitive to radiation damage, since it is produced in modern technology. The replacement of the Slow Control interface brought about the need to rewrite the control software. Formerly an extensive program was available to control the BST Strip System only. The software for the BSTT was "expert only", i. e. not suitable for operation by the H1 shift crew.

As part of the work for this thesis a new Slow Control Program was written in the LabView [32] framework. A screen shot of the front panel is shown in figure 6.12. More screen shots and parts of the source code together with some more technical details are given in the appendix A.

Figure 6.13 shows the major components used in the Slow Control. The program runs on a "Macintosh Quadra 800" computer located in the H1 control room. It has a "MICRON MacVEE" interface card to the VME crates responsible for the BST Slow Control functions. In this crate several
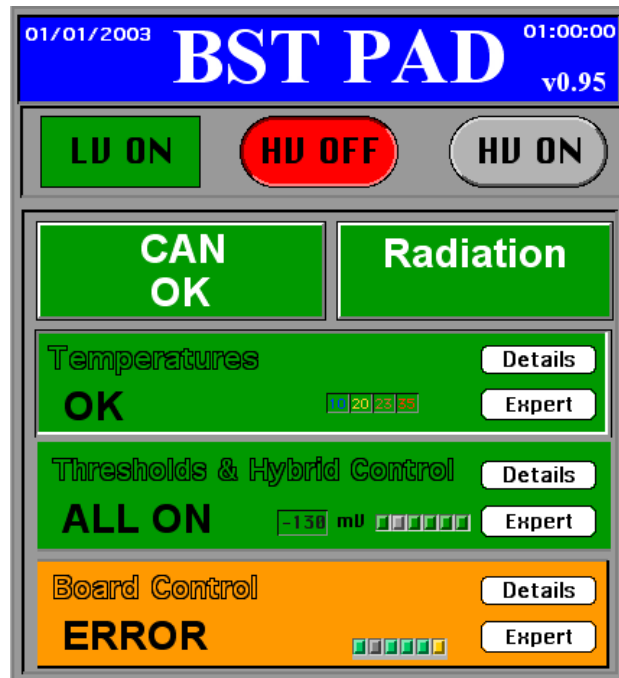
Figure 6.12: Front panel of the new unified BSTT Slow Control Program

VME modules are available for different tasks:

- An "IP-Carrier" provides two interfaces: an IP-CAN card for CAN bus communication with the front-end repeater boards and the Master Card in the trigger crate, and an IP-UNIDIG card for access to the central H1 Slow Control System BBL3 [33].

- The "Power and Download Station" (PDS) for controlling low and high voltages, checking trigger status signals from the front end, resetting the front end and multiplexing the JTAG bus to the 6 repeater boards.

- A watchdog card that signals problems with the control programs to the BBL3 system.

Reprogramming the ALTERA APEX/ACEX chips on the repeater boards has to be done from a "Industrial Windows PC" with proprietary software (MaxPlus). This can be done remotely using the JTAG multiplexing feature and the "Remote Control" software "Timbuktu Pro" [34]. All other aspects of the BSTT steering are available in the LabView program with a graphical user interface. The tasks of this program are (used communication channels in brackets):
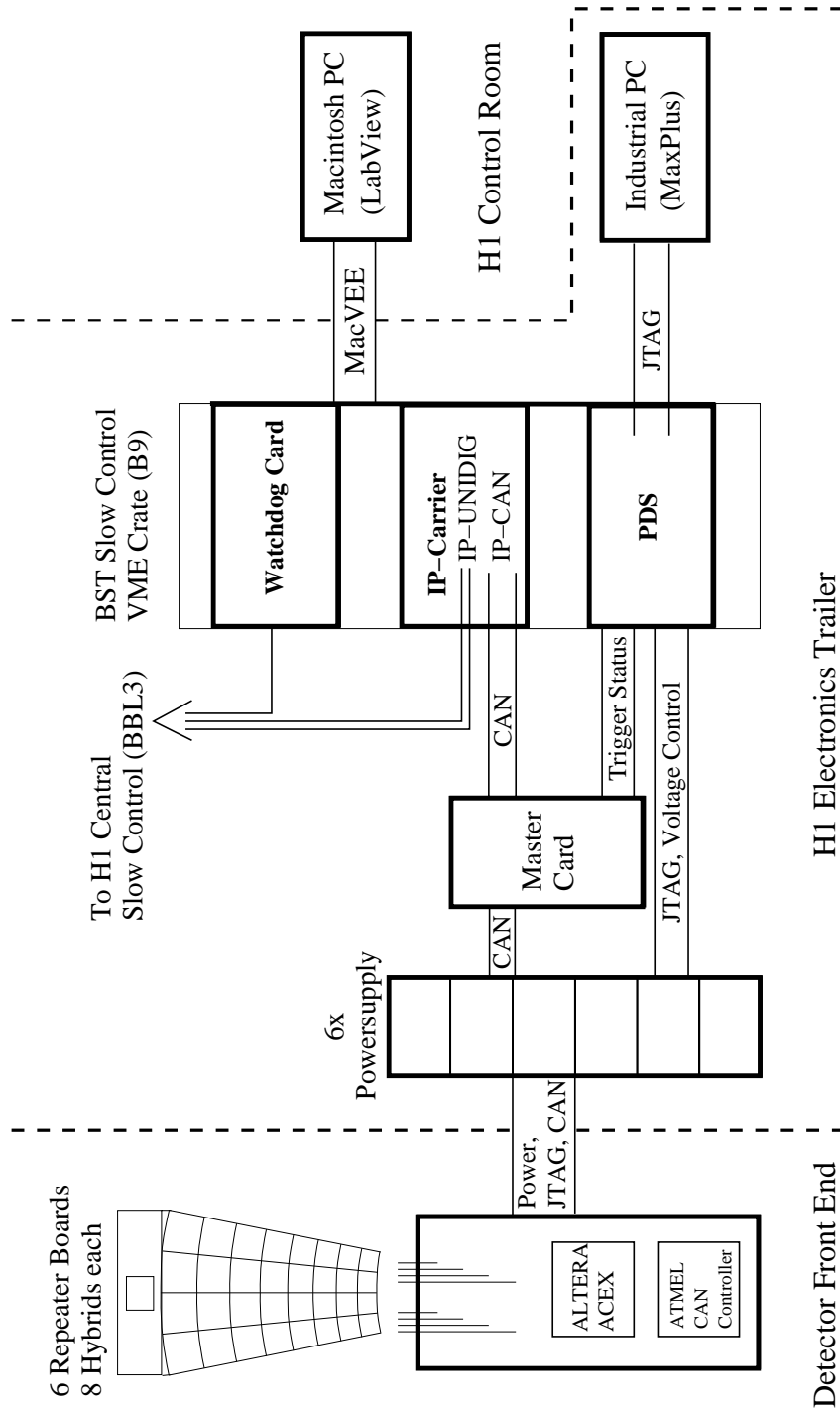
Figure 6.13: Schematic overview of the components used in BSTT Slow Control.

- Regular checks of the temperature (CAN, BBL3): The temperature is displayed graphically and written into a history file. Temperature "Warning" and "Alarm" are signaled when the adjustable thresholds are crossed. This is displayed optically and also transmitted to the BBL3 system to alarm the shift crew.

- Changing the threshold and special settings for the readout ASIC on every hybrid (CAN): The signal threshold controls the detector efficiency and noise. This is equivalent to imposing a S/N cut. The readout chip is reprogrammable and special settings might be required.

- Setting and reading the low and high voltage status of every repeater board (PDS, BBL3): The high voltage status is transferred to the BBL3 system, as well as errors in supply voltages.

- Regular checks of all available status information (CAN, PDS, BBL3): Status registers of the ALTERA chips and various trigger status bits provided through the PDS module can be checked to ensure reliable operation. Errors are displayed graphically and signaled to the BBL3 system.

- Front-end reset (PDS): Due to Single Event Upsets programs might be disturbed and a reinitialization of the ASICs, the ALTERA chips, and the ATMEL CAN controllers has to be done.

- Switching the JTAG input to another board (PDS): Used in conjunction with the Industrial PC to reprogram the ALTERA Chips.

- Signaling a properly running control program (Watchdog): This is done, if both Stirp and PAD Slow Control programs are running and have access to the VME crates.

Summary

H1 is one of the collider experiments at the HERA accelerator. The possibility to study deep inelastic lepton–proton scattering at a center of mass energy of 920 GeV is unique. The upgrade of the collider for the high luminosity phase HERA II also brought about many changes in the detector setup.

The BSTT is a new fast trigger device in the backward region of H1. It is designed for fast track recognition in the region of low Q^2 to support the measurement of the proton structure functions F_2 and F_L. In addition, it provides H1's most important background indicator, the H1 Radiation Monitor.

In this thesis efforts to understand the background situation after the HERA upgrade were presented. The problems have prevented planned high luminosity operation so far. A simple model was developed and applied to Radiation Monitor and CJC data. It can reasonably well explain the various contributions of beam-induced background. The beam pipe pressure increases dynamically due to synchrotron radiation. This results in frequent proton beam–gas scattering, which dominates the background. Slow improvements were seen during operation due to continuous vacuum conditioning ("bake out"). Nevertheless the background extrapolated to design currents still exceeded the tolerable limit by a factor of 2 to 3. Changes in the vacuum and collimator system in "North Right" in the 2003 shutdown are expected to help overcome the background problems.

First BSTT data was collected before and after the shutdown in an unbiased raw data mode. Both sets were analyzed and good correlation with SpaCal clusters was observed. Single detector efficiency was estimated to be in the range 90% to 95% with typical statistical uncertainty of 2% for good modules. Random coincidences due to noise were estimated to affect less than 2% of all events. Also preliminary tests showed capabilities of the BSTT for background suppression at the first trigger level.

In the last part of the thesis, development and maintenance of silicon detectors were discussed. During the first 2 years of HERA II running the

integrated dose received by the BST was exceptionally high despite effective online monitoring with the Radiation Monitor delivered by the BSTT. This caused radiation damage in 41 out of 72 BST φ-strip detector modules and the electronics of the Strip and Pad repeaters. A strong dependence of the damage on the z position of the detector showed synchrotron radiation to be responsible for the observed malfunctions.

New strip modules were tested. They were needed to replace the old r-strip sensors and irradiated modules. Tests included the determination of the depletion voltage, measurements of leakage currents, tests of long term stability, tests of the readout electronics, and a laser test to ensure efficient overall performance of each module. Out of 113 delivered sensors 80 showed good results and were used in the BST.

The radiation hard redesign of the Pad repeaters brought about a change in the Slow Control of the BSTT. A LabView program was written to handle all aspects of the Slow Control in a unified environment for experts and the H1 shift crew. This includes temperature control, supply voltage and trigger system settings, continuous control of reliable operation, and a front-end reset feature.

Appendix A

The BSTT Slow Control Program

LabView was chosen as the language for the Slow Control program. It provides good graphical user interface capabilities. The programming is done in a language called "G". In contrast to conventional languages like Fortran or C(++), variables, arithmetical operators, subroutines, loops and other control structures are represented as graphical objects. The data flow is determined by drawing wires between these objects.

The user interface of the program is divided into several parts:

- The front panel shown in figure 6.12. Here status information and errors are displayed in a compact form. Also the high voltage might be switched off by the shift crew. The subprograms for expert control and details are accessible.

- "Details" are available for each section. This gives only additional information and no changes can be made. An example are the temperature history plots, see figure A.1.

- "Expert Panels" are available for each section. Here experts that know the password can change settings. Examples are given in figure A.2. Most settings are self explaining. With the "Control ON/OFF" buttons (accidental) changes for the respective sector can be avoided.

In the figures A.3 to A.5 the source code of the main program is shown as example. To enforce a certain sequence, the code has to be structured in frames.

The Slow Control interfaces are accessed in different ways. On the one hand BBL3 and PDS are accessed directly through reading and writing VME registers. They are mapped by the MacVEE card into the system addressable
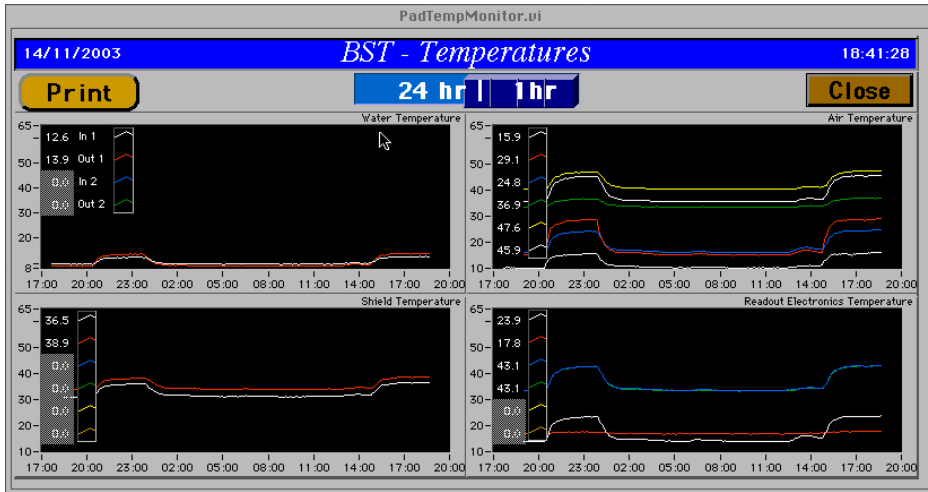
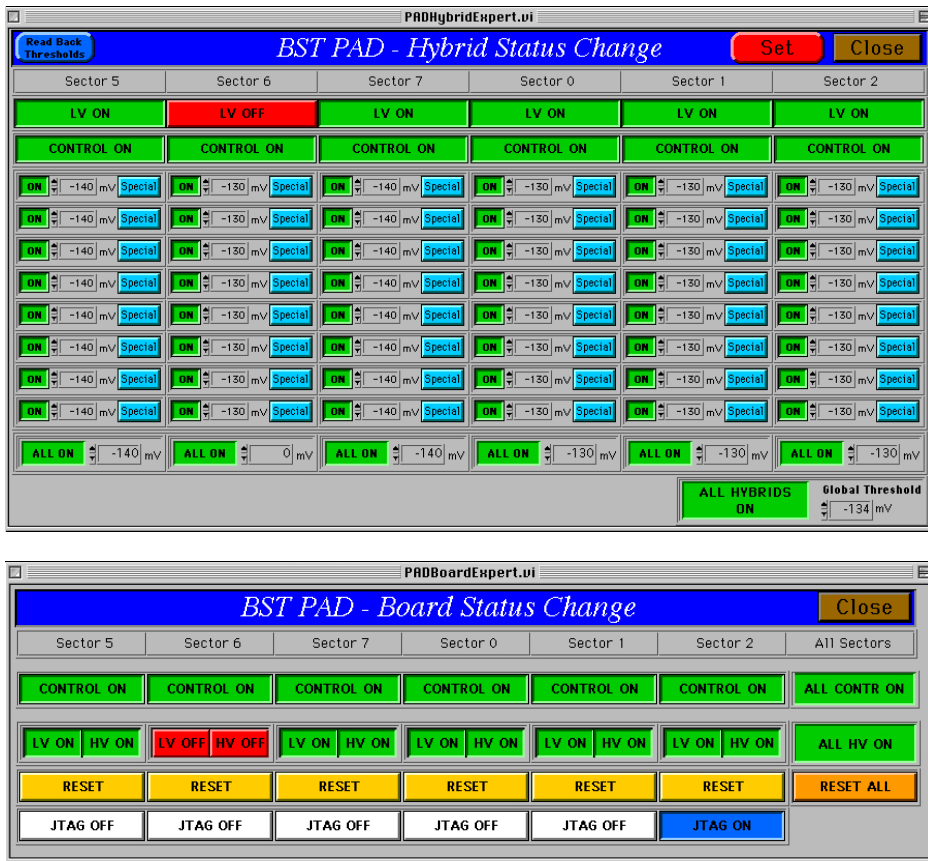Figure A.1: History Temperature Plots from the "Detail" Section

Figure A.2: Two of the 3 "Expert" control panels for changing BSTT settings.

memory. The CAN interface on the other hand is accessed via a user driver. While this in lower levels again uses the VME access through memory mapping, the user interface is "message" based.

The description of available CAN functions is given in [35]. Any command sent from the Slow Control program is acknowledged by an echo message from the receiving controller. This ensures reliable transmission. As the bus can be used by all attached controllers to send messages at any time, another level including a receiving queue was implemented. This is for example necessary to properly handle situations, when one board sends its temperatures according to the programmed time interval while new threshold settings are being set. Queue handling includes functions like initialization, echo-verified message sending, looking up specific messages or clearing the queue from processed messages.
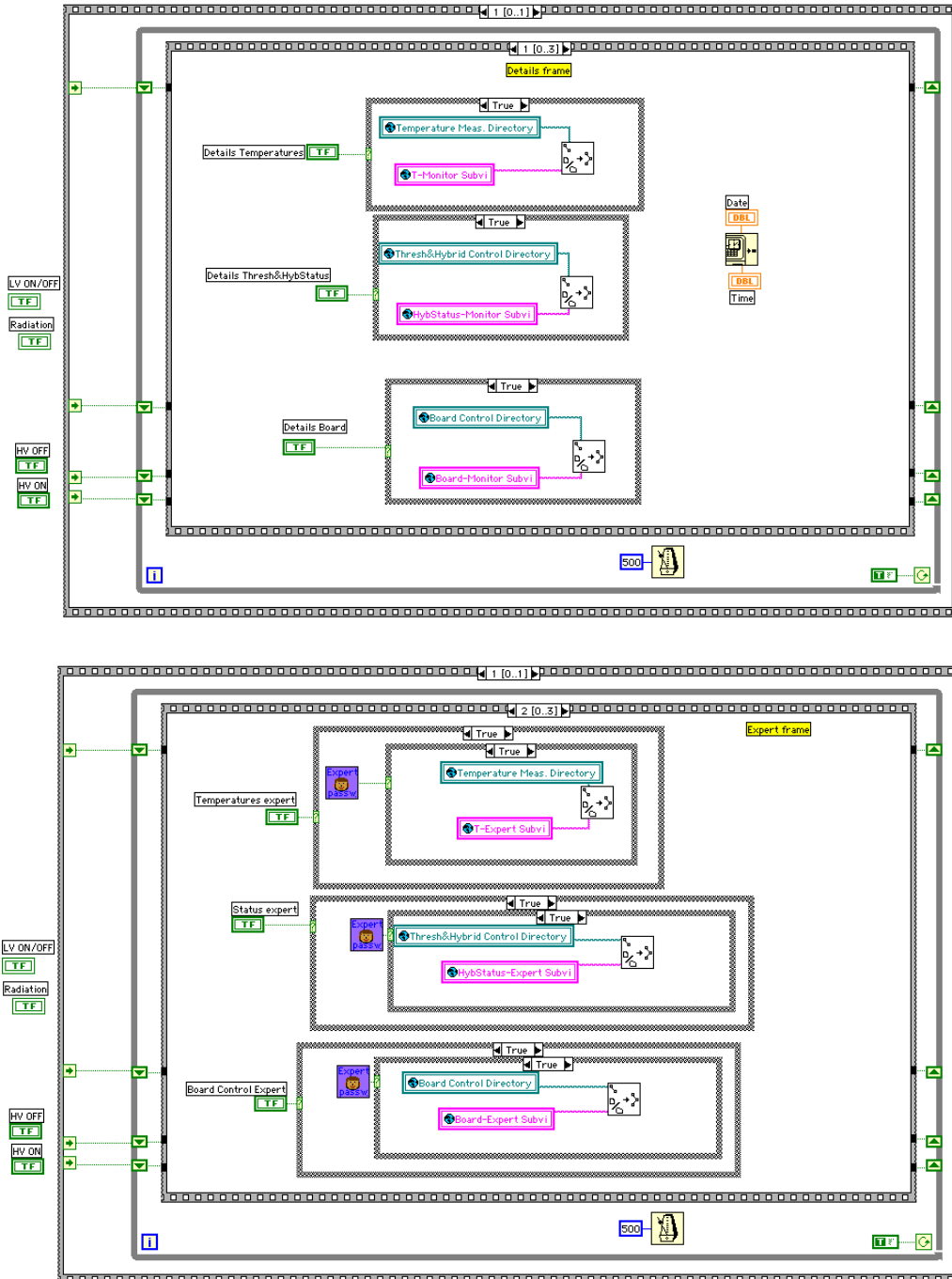
Figure A.3: Source Code of the BST PAD front panel program

Figure A.4: Source Code of the BST PAD front panel program, continued
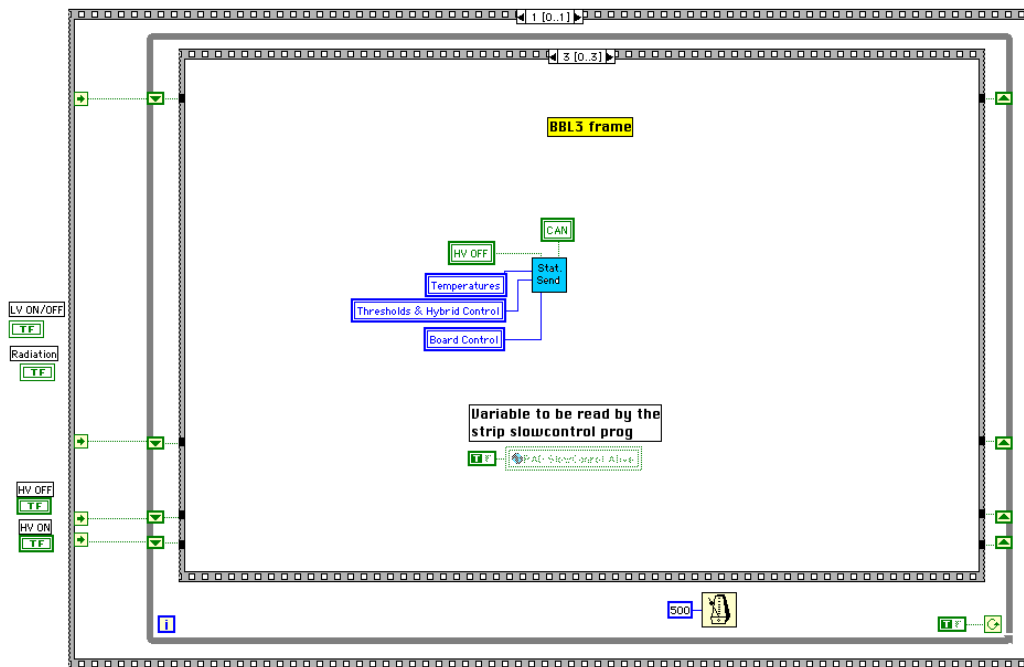
Figure A.5: Source Code of the BST PAD front panel program, continued

Appendix B

Deutsche Kurzfassung

Im H1 Experiment werden die hochenergetischen Elektron- und Proton-
strahlen des HERA Speicherringes zur Kollision gebracht. Die Möglich-
keit, Lepton-Proton-Wechselwirkungen bei einer Schwerpunktsenergie von
920 GeV zu untersuchen, ist weltweit einmalig. Um höhere Luminositäten
zu erreichen, wurde das Strahlfokussiersystem des Beschleunigers verändert.
Dieses HERA II System hat großes Potential für Präzissionsmessungen.

Der BSTT ("Backward Silicon Track Trigger") ist ein neuer Detektor im
rückwärtigen Bereich von H1. Er benutzt Siliziumdetektoren mit grossflächigen
Strukturen zur schellen Spurerkennung geladener Teilchen. Durch moderne
Elektronik ist der BSTT in der Lage, Entscheidungen ohne Verzögerung, also
für jeden möglichen Wechselwirkungszeitpunkt, zu treffen ("L1 Trigger"). Er
wurde zur Unterstützung der Messung der Proton-Strukturfunktionen F_2 und
F_L im Bereich kleiner Impulsüberträge Q^2 entwickelt. Zusätzlich liefert der
BSTT den wichtigsten Echtzeitindikator der Untergrundbedingungen, den
"H1 Radiation Monitor".

In dieser Arbeit werden Teile der Anstrengungen dokumentiert, die Unter-
grundsituation nach den Veränderungen am HERA Beschleuniger zu ver-
stehen. Probleme verhinderten bis jetzt das Betreiben des Beschleunigers
mit hohen Strahlströmen und hoher Luminosität. Ein einfaches Modell wird
entwickelt, um die Abhängigkeit der Untergrundindikatoren Radiation Moni-
tor und CJC (Zentrale Spurkammer, Central Jet Chamber) Ionisationsstrom
von den Strahlströmen zu erklären. Dieses empirische Modell kann einzelne
Bestandteile des im Strahlbetrieb auftretenden Untergrunds ausreichend gut
erklären. Das Vakuum verschlechtert sich dynamisch durch die Einwirkung
von Synchrotronstrahlung. Dies führt zur häufigen Streuung von Protonen
an Restgasatomen, welche den Hauptteil des beobachteten Untergrunds aus-
machen. Langsame Fortschritte im laufenden Betrieb durch verbessertes
Restvakuum sind erkennbar. Allerdings ist der Untergrund extrapoliert auf

die vorgesehenen maximalen Ströme immer noch zwei bis dreimal zu hoch. Im Jahre 2003 wurden Verbesserungen im Vakuum- und Kollimatorsystem nahe dem Wechselwirkungspunkt vorgenommen, die diese Probleme beseitigen sollen.

Für eine erste Datenanalyse lieferte der BSTT unverarbeitete Detektorsignale. Die Datennahme erfolgte kurz vor und nach der Betriebsunterbrechung im Jahre 2003. Die Signale werden auf Korrelation mit Signalen des Spaghetti Kalorimeters (SpaCal), welches Energie und Position von Teilchen hinter dem BSTT bestimmt, untersucht. Vollständig intakte Module weisen einen Teilchendurchgang mit einer Effizienz von etwa 90% bis 95% nach; der statistische Fehler dieser Effizienzbestimmung beträgt typisch 2%. Falsche Signale in Koinzidenz mit dem SpaCal durch Rauschen treten in weniger als 2% aller Ereignisse auf. Vorläufige Tests zeigen die Fähigkeit des BSTT zur Unterdrückung von Untergrundereignissen in der ersten Triggerebene.

Im letzten Teil der Arbeit werden Entwicklung und Instandhaltung von Siliziumdetektoren besprochen. Während der ersten zwei Betriebsjahre von HERA II wurden Teile des BST ("Backward Silicon Tracker") trotz effizienter Überwachung durch den H1 Radiation Monitor mit hohen Dosen belastet. Das führte zu Strahlungsschäden an 41 von 72 BST Streifendetektormodulen und an der detektornahen Elektronik auf sogenannten "Repeater"-Platinen. Die beobachtete starke Abhängingkeit der Schäden von der z-Position der Module zusammen mit Dosimetermessungen zeigten deutlich, dass Synchrotronbestrahlung für aufgetretene Fehlfunktionen verantwortlich ist.

Neue Streifendetektormodule wurden getestet. Diese werden einen älteren Detektortyp und strahlengeschädigte Module ersetzen. Diese Test umfassen die Bestimmung der Verarmungsspannung, Messung der Leckströme, Tests auf Langzeitstabilität, Tests der Signalausleseelektronik und einen Lasertest zur Endkontrolle jedes Moduls. Von 113 gelieferten Sensoren wurden 80 aufgrund guter Ergebnisse für den Einbau in den BST ausgewählt.

Um die "Repeater"-Platine des BSTT weniger empfindlich für Strahlungsschäden zu machen, war ein Neuentwurf des "Slow Control"-Systems, welches zeitunkritische Steuerfunktionen und Statusinformationen bereitstellt, unvermeidlich. Ein im Rahmen dieser Arbeit mit der grafischen Programmierumgebung LabView entwickeltes Programm wird vorgestellt. Es vereinigt alle verfügbaren "Slow Control"-Funktionen in einer einheitlichen Oberfläche: Temperaturkontrolle, Einstellungen der Versorgungsspannungen und des Triggersystems, ständige Überwachung der ordnungsgemäßen Funktion und die Möglichkeit zum Neustart der Triggerelektronik.

Bibliography

[1] H. Abramowicz and A. C. Caldwell, *HERA collider physics, Rev. Mod. Phys.* **71** (1999), no. 5 1275–1409.

[2] A. M. Cooper-Sakar, R. C. E. Devenish and A. de Roeck, *Structure Functions of the Nucleon and their Interpretation, Int. J. Mod. Phys. A* **13** (1998), no. 20 3385–3586 [`hep-ph/9712301`].

[3] H1 Collaboration, C. Adloff *et. al.*, *Deep-inelastic inclusive ep scattering at low x and a determination of* α_s, *Eur. Phys. J.* **C21** (2001) 33–61 [`hep-ex/0012053`].

[4] H1 Collaboration, *Determination of The Longitudinal Proton Structure Function* F_L *at low* Q^2, presented at DIS 2003, St. Petersburg, H1prelim-03-043, available at http://www-h1.desy.de/h1/www/publications, 2003.

[5] H1 Collaboration, C. Adloff *et. al.*, *Measurement of D* meson cross sections at HERA and determination of the gluon density in the proton using NLO QCD, Nucl. Phys.* **B545** (1999) 21–44 [`hep-ex/9812023`].

[6] H1 Collaboration, I. Abt *et. al.*, *The H1 detector at HERA, Nucl. Instrum. Meth.* **A386** (1997) 310–396.

[7] H1 Collaboration, SPACAL Group, *Performance of an electromagnetic lead/scintillating-fibre calorimeter for the H1 detector, Nucl. Instrum. Meth.* **A374** (1996) 149–156.

[8] H1 Collaboration, *ep Physics beyond 1999*, H1 note H1-10/97-531, 1997.

[9] K. Hagiwara *et. al.*, *Review of Particle Physics, Physical Review D* **66** (2002) 010001+. http://pdg.lbl.gov.

[10] H1 Collaboration, *Technical Proposal to build Silicon Tracking Detectors for H1*, H1 note H1-06/92-226, 1992.

[11] W. Braunschweig *et. al.*, *A Forward Silicon Tracker for H1*, H1 note
H1-02/99-563, 1999.

[12] C. Kiesling *et. al.*, *Proposal to Complement the H1 Backward Silicon
Tracker(BST) with ϕ-Strip Detectors*, H1 note H1-01/98-534, 1998.

[13] I. Tsurin, *Development of a fast H1 trigger using silicon pad detectors*,
Nucl. Instrum. Meth. **A501** (2003) 219–221.

[14] W. Eick *et. al.*, *Development of the H1 backward silicon strip detector*,
Nucl. Instrum. Meth. **A386** (1997) 397.

[15] H. Henschel and R. Lahmann, *The backward silicon tracker of the H1
experiment at HERA*, *Nucl. Instrum. Meth.* **A453** (2000) 93–97.

[16] W. J. Haynes *et. al.*, *The H1 silicon tracker data acquisition system*,
Nucl. Instrum. Meth. **A403** (1998) 313–325.

[17] M. Nožička, *Silicon detector for detection of inelastic scattering of
electrons on protons in H1 experiment*, Master's thesis, Charles
University in Prague, 2000.

[18] H. Henschel *et. al.*, *A Silicon Pad Detector L1 Trigger for Deep
Inelastic Scattering at Low x and Q^2*, H1 note H1-04/92-221, 1992.

[19] I. Tsurin, *The Backward Silicon Track Trigger of the HERA
Experiment H1*. PhD thesis, DESY Zeuthen, 2003.

[20] Altera Corporation, *Web site*, http://www.altera.com.

[21] Atmel Corporation, *Web site*, http://www.atmel.com.

[22] Intersil Corporation, *Web site*, http://www.intersil.com.

[23] H1 background working group, *Technical Report on the Beam Induced
Backgrounds in the H1 Detector*, H1 note H1-10/02-606, available at
http://www-h1.desy.de/h1/www/publications, 2002.

[24] H1 background working group, *Further Report on the Beam-Induced
Backgrounds in the H1 Detector*, H1 note H1-01/03-607, available at
http://www-h1.desy.de/h1/www/publications, 2003.

[25] ROOT, *An Object-Oriented Data Analysis Framework*,
http://root.cern.ch.

[26] nELAN, *H1 Physics Working Group for Inclusive Measurements*, http://www-h1.desy.de/h1/www/h1work/inc/index.html.

[27] PAW, *Physics Analysis Workstation*, http://paw.web.cern.ch/paw.

[28] G. A. Schuler and H. Spiesberger in *Proc. Workshop on HERA Physics* (W. Buchmüller and G. Ingelman, eds.), vol. 3, p. 1419, Hamburg, DESY, 1992.

[29] R. Engel and J. Ranft, *Hadronic photon-photon interactions at high energies*, Phys. Rev. **D54** (1996) 4244–4262 [`hep-ph/9509373`].

[30] LHCb Electronics Group, *Radiation hardness assurance*, http://lhcb-elec.web.cern.ch/lhcb-elec/html/radiation_hardness.htm.

[31] C. Niebuhr and D. Pitzl, *CJC currents*, http://www-h1.desy.de/h1/www/general/run03/cjc/cjc-curr.html.

[32] National Instruments, *LabVIEW*, http://www.ni.com/labview.

[33] H1 Collaboration, *H1 Central Slow Control*, http://www-h1.desy.de/isc.

[34] Netopia, *Timbuktu Pro Remote Control Software*, http://www.timbuktupro.com.

[35] M. Winde, *CAN Message Format in the upgraded BST3*, http://www-zeuthen.desy.de/∼winde/h1/h1bst.

Acknowledgments

First of all I wish to thank my parents, who supported me during my studies in all aspects.

Next I wish to thank all the people of H1 and DESY Zeuthen for their help and support, especially Peter Kostka, whose door was always open for me, and Max Klein, who introduced me to H1. I'm also indebted to Prof. Hermann Kolanoski, who made my work in Zeuthen possible by officially supervising it.

During my work I learned a lot from Mirek Nožička and Ilya Tsurin, who shared their knowledge about the BST with me. Together with many other great colleagues, Achim Meißner, Hans Henschel, Wolfgang Lange, and Micha Winde, we had a busy and exciting time during the BST repair.

Tomáš Laštovička, Thomas Naumann, and Serguey Gorbounov also helped me in many small aspects of my work. Special thanks go to Katerina Lipka for the time she dedicated to helping me.

Last but not least I'd like to thank my office mates Ewelina Lobozinska, Maja Čolovič, Ivan Glushkov, Alexey Petrukhin and everyone mentioned above for a nice time.

Erklärung

Hiermit bestätige ich, ich die vorliegende Arbeit ohne unerlaubte fremde Hilfe angefertigt und nur die abgegebene Literatur und Hilfsmittel verwendet zu haben.
Mit der Auslage meiner Diplomarbeit in der Bibliothek der Humboldt-Universität zu Berlin bin ich einverstanden.

Jan Kretzschmar
Berlin, den 15.12.2003